CONVERGENCE OF THE NOTCH, TGF-BETA AND SONIC HEDGEHOG PATHWAYS IN NEURAL PROGENITOR CELL SPECIFICATION AND DIFFERENTIATION

by

Raymond L. Swetenburg, III

(Under the Direction of Steven L. Stice)

ABSTRACT

One of the best studied fate switches in mammalian development is the specification and differentiation of cell types within the ventral neural tube, the precursor to the spinal cord. Unspecified cells experience a gradient of Sonic hedgehog (Shh) from the notochord and, later, the floor plate, which ultimately will become the complete motor control circuit responsible for all movement, both voluntary and involuntary. Initially, the transcription factor Olig2 is expressed under this Shh gradient in the ventral-most pool of cells. Within this group, more dorsal cells retain their Olig2 identity becoming the motor neuron progenitor domain (pMN), while more ventral cells, under the influence of increased Shh signaling, will express the Olig2-repressive transcription factor Nkx2.2 and become the p3 domain. Both progenitor pools initially generate neurons by self-preserving asymmetric divisions: motor neurons from the pMN and V3 interneurons from the p3. Later in development, these cells undergo a fate switch, where the sharp division between the domains becomes blurred and Olig2 and Nkx2.2 eventually become co-expressed as oligodendrocyte progenitor cells (OPC). The

juxtacrine Notch-Delta pathway is critical throughout neural development, though the results of gain- and loss-of-function experiments have shown it to be extremely context-dependent. For instance, Notch inhibition has been demonstrated to increase pMN at the expense of p3, increase MN at the expense of pMN or increase OPC at the expense of pMN, depending on the specific timing and method of inhibition. We therefore asked how Notch inhibition might regulate the Olig2 protein within the context of pluripotent stem cell towards these cell types. In this work, we show that Notch inhibition destabilizes Olig2 during neurogenesis by a post-transcriptional mechanism which can be rescued by Tgf-β signaling. Further, we explore the intricate push and pull of Shh, Notch-Delta and Tgf-β in the derivation and specification of pMN, p3, MN and OPC in which these signals can have multiple targets and modulate cell differentiation in complex, and sometimes opposing, manners. We have identified novel and diverse paradigms for Olig2 regulation throughout the course of differentiation with implications for stem cell biology and future models of disease and development.

INDEX WORDS: Pluripotent Stem Cells, Neural Differentiation, Neural Progenitor, Olig2, Nkx2.2, Notch-Delta, Tgf-β, Sonic Hedgehog (Shh), pMN, p3, Motor Neuron, Oligodendrocyte

CONVERGENCE OF THE NOTCH, TGF-BETA AND SONIC HEDGEHOG PATHWAYS IN NEURAL PROGENITOR CELL SPECIFICATION AND DIFFERENTIATION

by

RAYMOND L. SWETENBURG, III

B.S., University of the South, 2002

A Dissertation Submitted to the Graduate Faculty of The University of Georgia in Partial Fulfillment of the Requirements for the Degree

DOCTOR OF PHILOSOPHY

ATHENS, GEORGIA

2017

CONVERGENCE OF THE NOTCH, TGF-BETA AND SONIC HEDGEHOG PATHWAYS IN NEURAL PROGENITOR CELL SPECIFICATION AND DIFFERENTIATION

by

RAYMOND L. SWETENBURG, III

Major Professor:	Steven L. Stice
Committee:	Nicolay M. Filipov
	James D. Lauderdale
	Franklin D. West

Electronic Version Approved:

Suzanne Barbour
Dean of the Graduate School
The University of Georgia
August 2017

DEDICATION

I would like to dedicate this dissertation work to my parents, my siblings, my children and my wife. I could not have done any of this without them.

ACKNOWLEDGEMENTS

I would like to thank Dr. Filipov, Dr. Lauderdale and Dr. West for their guidance and critical advice. I would also like to thank Dr. Doug White, Dr. Todd McDevitt and Dr. Melissa Kemp for their help in Chapter 3 and for pushing me out of my comfort zone. Thanks to the Stice lab members, past and present. Thanks to the other RBC labs and members. Finally, and most importantly, thanks to Steve. He gave me a chance when he probably shouldn't have, pushed me to always be better, showed impossible patience and helped me up when I fell. For that, I am forever indebted to him.

TABLE OF CONTENTS

Page

CHAPTER 1

INTRODUCTION

Cellular fate decisions are the basis for all development. Cellular diversity, organ size and tissue homeostasis all rely on a complex and overlapping system of signaling mechanisms which precisely time and pattern development from the embryo to the adult and beyond. There are two key components in determining cell fate decisions: the surrounding extracellular microenvironment and the intracellular genetic state. The extracellular environment is comprised largely of the bioavailability of signaling molecules and the composition of the extracellular matrix, but also includes mechanical, chemical and electrical cues. On the micro scale, these interactions include juxtacrine and paracrine signals between cells in close proximity to each other. On a more macro scale, cells are patterned by precisely timed morphogen gradients which have differing effects on cells depending on their proximity to the source. This information is then interpreted through various receptors and channels triggering signaling cascades that are based almost directly on the internal state of the cell. This internal state is defined by both the epigenetic and genetic landscape within each cell, including the various receptors, scaffolds, transcriptional machinery, etc. which are available at a given time.

One of the best studied of patterning mechanisms occurs during the specification and differentiation of the ventral neural tube, which will ultimately become the spinal cord. A gradient of Sonic hedgehog (Shh) emanates from the notochord and, later, the floor plate, to generate five distinct progenitor domains: p3, pMN, p2, p1 and p0 [1-3].

These domains will divide and differentiate to become the neurons and glia of the motor control circuit, responsible for all voluntary and involuntary movement. The Shh pathway is activated when Shh binds patched (Ptch), thus derepressing Smoothened (Smo). Smo then triggers the GLI Family Zinc Finger (Gli) members which act as transcription factors driving Shh target genes. Multiple small molecules can suppress or activate the Shh pathway at the Smo level including cyclopamine and purmorphamine [4], which inhibit and activate the Shh pathway, respectively. How cells interpret Shh signaling is the topic of a number of excellent studies. Essentially, there is a feedback mechanism in which Gli activators drive Ptch, meaning there is more inhibition of Smo [5, 6]. Thus, cells that have experienced a wave of Shh are more resistant to future Shh waves. Shh first induces oligodendrocyte transcription factor 2 (Olig2) in a subset of ventral cells by suppressing the transcription factor paired box 6 (Pax6) [7]. The more ventral cells are desensitized to Shh, as noted, while a subset of the more dorsal Olig2 cells express the NK2 homeobox 2 (Nkx2.2) protein under increased Shh, which in turn represses Olig2 to establish the p3/pMN boundary [1, 8]. Both the pMN and p3 domains undergo two waves of differentiation. The initial wave is comprised of self-preserving asymmetric divisions generating newborn neurons, including motor neurons from the pMN domain and V3 interneurons from the p3 domain. Later, the boundary between pMN and p3 blurs as Olig2 and Nkx2.2 are co-expressed, becoming oligodendrocyte precursor cells (OPC). A key regulator of gliogenesis is the transforming growth factor-β (Tgf-β) family of signaling molecules, which have been shown to increase the OPC marker SRY-Box 10 (Sox10) [9]. Sox10 is required, along with Olig2 an Nkx2.2, for fully functional OPC [10]. Notably, Sox10 expression alone is not sufficient to drive

Nkx2.2 [10]. Further, Tgf-β family members are upregulated both in the pMN region and the motor columns of the neural tube around the time of gliogenesis [11].

Olig2 is a basic helix-loop-helix (bHLH) transcription factor driven by Shh signaling. bHLH largely function as hetero- or homodimers, and their choice of co-factor is subsequently regulated by post-translational modifications and binding partner availability [12-15]. Olig2 and the anti-mitotic, pro-neurogenic bHLH Neurogenin 2 (Ngn2) transcription factor function in opposition in the early pMN domain, during neurogenesis. Ultimately, as Ngn2 levels increase, Olig2 transitions from a homodimeric state to forming heterodimers with Ngn2, thus repressing Olig2 function and inducing neurogenesis [16, 17]. Olig2 phosphorylation state has been strongly linked to pro-neurogenic or anti-neurogenic outcomes including cofactor choice, the MN-to-OPC fate switch and proliferation [13, 15, 18-20]. Tgf-β2 transcription in gliomas can be upregulated by dephosphorylated Olig2, and repressed by phosphorylated Olig2 [21], providing a further link between Olig2 phosphorylation, Tgf-β and the glial switch.

Critical to many cell fate decisions, including neural differentiation, is the Notch-Delta pathway. Notch-Delta is a juxtacrine signaling mechanism activated by cell-cell contact and mediated through the Notch receptors, Notch1-4, and its ligands, including the Jagged and Delta-like family members [22, 23]. Notch inhibition, notably, can have different effects on pMN at different times during development. When Notch-Delta is genetically inhibited in all cells expressing Olig2, the pMN domain expands at the expense of the p3 through a Shh-mediated mechanism. Essentially, the effects of Shh are blunted, resulting in a lack of Nkx2.2 and more Olig2 cells [24]. In total knockout mutants, Notch1 depletion causes extreme neurogenesis at the expense of progenitors and

glia, indicative of the role Notch plays in the maintaining the cell cycle and preventing neurogenesis [22]. Likewise, when Notch is overexpressed, precocious OPC are generated at the expense of MN [25]. Towards the end of neurogenesis, when Notch signaling is expressed in a salt-an-pepper pattern, Notch inhibition generates precocious OPC as seen in Notch overexpression studies [26]. Therefore, Notch-Delta, and specifically Notch-Delta inhibition, is a context dependent process particularly in regards to pMN regulation.

One noteworthy aspect of Notch regulation of pMN differentiation is the downstream regulation of Olig2 after Notch modulation. Olig2 plays multiple roles over the course of differentiation, initially producing motor neurons while preserving a subset of mitotic progenitors to for gliogenesis. Accordingly, computational modeling of gene regulatory networks has identified Olig2 as a key regulator of mitosis and the divide-versus-differentiate fate decision [27]. In high grade gliomas, Olig2 largely functions as a cancer stem cell marker where it can oppose p53 [20], further emphasizing its role as a cell cycle regulator. Notch inhibition, however, can downregulate Olig2 both in glioma and after stroke, leading to decreased mitosis and increased differentiation [28, 29]. Most confounding, however, is the ability to Notch inhibition to cause increases in pMN early, push cells towards the post-mitotic, $Olig2^-$ MN state in mid-differentiation, and then induce $Olig2^+$ gliogenesis. As noted, Notch inhibition occurs in a permissive, context-dependent manner. Our overall aim was to better understand how extracellular signaling factors might set this context and facilitate the varying outcomes of Notch inhibition.

To study the effects of Notch inhibition on pMN, and Notch regulation of Olig2 as a whole, we employed a murine pluripotent stem cell (PSC) model of differentiation.

We modified a heavily cited protocol to differentiate PSC towards MN using retinoic acid (RA) and the Shh mimic purmorphamine (Pur) [30]. Throughout differentiation, we applied different treatments to cultures to see how pMN, and other cell types of interest, might respond. From these results, we were able to conceptualize a differentiation trajectory inclusive of these signals to better understand how they might be affecting differentiation.

Chapter 2 is a literature review from a published book chapter, which focuses on the specification of MN both *in vivo* and *in vitro.* In Chapter 3, we present a paper currently under review. Here, we employed computational modeling techniques to uncover novel mechanistic insights into MN and OPC specification. A combination of wet lab experiments was combined with stochastic and deterministic models to better understand differentiation. Stochastic models employ a degree of randomness and probability, and were based upon current literature in order to determine an overarching differentiation mechanism for our *in vitro* system. However, when various literature- and hypothesis-based models were compared to our experimental data, we found insurmountable discrepancies, notably in the amount of MN observed compared to potential pool of identifiable Olig2-expressing cells. We proposed, therefore, that a destabilized progenitor cell exists capable of bypassing mitosis to generate MN in the possible absence of identifiable Olig2. We then experimentally demonstrate a soluble signal from a late-arising population of cells capable of suppressing neurogenesis and increasing gliogenesis in a negative feedback loop. Further, by inhibiting Notch both early and late, we were able to experimentally recreate pro-neurogenic and pro-gliogenic effects seen *in vivo* and offer computational explanations for their underlying

mechanisms. Because our switch signal was demonstrated as soluble and Notch-Delta is inherently juxtacrine, we were able to spatially model each mechanism discretely to generate a three dimensional model of pMN regulation. Here, spatiotemporal aspects of Olig2-expressing cells and their progeny were successfully simulated complementary to experimental data. Lastly, we also explore Tgf-β signaling as a probable instigator of the glial switch, capable of suppressing or enhancing neurogenesis by activation and inhibition, respectively.

Chapter 4 presents work to be submitted further exploring the intersection of Shh, Tgf-β and Notch inhibition. However, this study is expanded to include the generation of the Nkx2.2-expressing p3 cell type to better capture the entire course of Olig2 differentiation. Taken together, we present a road map for *in vitro* PCS differentiation towards pMN, p3, MN and OPC, by investigating the interplay between three key extracellular signaling pathways, ultimately drawing novel conclusions about both the overlapping and, at times, opposing, forces at play.

References

1. Briscoe, J., et al., *A homeodomain protein code specifies progenitor cell identity and neuronal fate in the ventral neural tube.* Cell, 2000. **101**(4): p. 435-45.
2. Jessell, T.M., *Neuronal specification in the spinal cord: inductive signals and transcriptional codes.* Nat Rev Genet, 2000. **1**(1): p. 20-9.
3. Briscoe, J. and J. Ericson, *Specification of neuronal fates in the ventral neural tube.* Current Opinion in Neurobiology, 2001. **11**(1): p. 43-49.
4. Sinha, S. and J.K. Chen, *Purmorphamine activates the Hedgehog pathway by targeting Smoothened.* Nat Chem Biol, 2006. **2**(1): p. 29-30.
5. Dessaud, E., A.P. McMahon, and J. Briscoe, *Pattern formation in the vertebrate neural tube: a sonic hedgehog morphogen-regulated transcriptional network.* Development, 2008. **135**(15): p. 2489-2503.
6. Dessaud, E., et al., *Interpretation of the sonic hedgehog morphogen gradient by a temporal adaptation mechanism.* Nature, 2007. **450**(7170): p. 717-20.
7. Ericson, J., et al., *Pax6 controls progenitor cell identity and neuronal fate in response to graded Shh signaling.* Cell, 1997. **90**(1): p. 169-80.
8. Sun, T., et al., *Cross-repressive interaction of the Olig2 and Nkx2.2 transcription factors in developing neural tube associated with formation of a specific physical complex.* J Neurosci, 2003. **23**(29): p. 9547-56.
9. Dias, J.M., et al., *Tgfbeta signaling regulates temporal neurogenesis and potency of neural stem cells in the CNS.* Neuron, 2014. **84**(5): p. 927-39.

10. Liu, Z., et al., *Induction of oligodendrocyte differentiation by Olig2 and Sox10: Evidence for reciprocal interactions and dosage-dependent mechanisms.* Developmental Biology, 2007. **302**(2): p. 683-693.

11. Dutta, D.J., et al., *Combinatorial actions of Tgfbeta and Activin ligands promote oligodendrocyte development and CNS myelination.* Development, 2014. **141**(12): p. 2414-28.

12. Zhou, Q. and D.J. Anderson, *The bHLH transcription factors OLIG2 and OLIG1 couple neuronal and glial subtype specification.* Cell, 2002. **109**(1): p. 61-73.

13. Sun, Y., et al., *Phosphorylation state of Olig2 regulates proliferation of neural progenitors.* Neuron, 2011. **69**(5): p. 906-17.

14. Novitch, B.G., A.I. Chen, and T.M. Jessell, *Coordinate Regulation of Motor Neuron Subtype Identity and Pan-Neuronal Properties by the bHLH Repressor Olig2.* Neuron, 2001. **31**(5): p. 773-789.

15. Li, H., et al., *Phosphorylation regulates OLIG2 cofactor choice and the motor neuron-oligodendrocyte fate switch.* Neuron, 2011. **69**(5): p. 918-29.

16. Mizuguchi, R., et al., *Combinatorial roles of olig2 and neurogenin2 in the coordinated induction of pan-neuronal and subtype-specific properties of motoneurons.* Neuron, 2001. **31**(5): p. 757-71.

17. Lee, S.K., et al., *Olig2 and Ngn2 function in opposition to modulate gene expression in motor neuron progenitor cells.* Genes Dev, 2005. **19**(2): p. 282-94.

18. Gaber, Z.B. and B.G. Novitch, *All the embryo's a stage, and Olig2 in its time plays many parts.* Neuron, 2011. **69**(5): p. 833-5.

19. Meijer, D.H., et al., *An amino terminal phosphorylation motif regulates intranuclear compartmentalization of Olig2 in neural progenitor cells.* J Neurosci, 2014. **34**(25): p. 8507-18.

20. Mehta, S., et al., *The central nervous system-restricted transcription factor Olig2 opposes p53 responses to genotoxic damage in neural progenitors and malignant glioma.* Cancer Cell, 2011. **19**(3): p. 359-71.

21. Singh, Shiv K., et al., *Post-translational Modifications of OLIG2 Regulate Glioma Invasion through the TGF-β Pathway.* Cell Reports, 2016. **16**(4): p. 950-966.

22. Yoon, K. and N. Gaiano, *Notch signaling in the mammalian central nervous system: insights from mouse mutants.* Nat Neurosci, 2005. **8**(6): p. 709-15.

23. Louvi, A. and S. Artavanis-Tsakonas, *Notch signalling in vertebrate neural development.* Nat Rev Neurosci, 2006. **7**(2): p. 93-102.

24. Kong, Jennifer H., et al., *Notch Activity Modulates the Responsiveness of Neural Progenitors to Sonic Hedgehog Signaling.* Developmental Cell, 2015. **33**(4): p. 373-387.

25. Tan, G.C., Esteban O. Mazzoni, and H. Wichterle, *Iterative Role of Notch Signaling in Spinal Motor Neuron Diversification.* Cell Reports, 2016. **16**(4): p. 907-916.

26. Rabadan, M.A., et al., *Jagged2 controls the generation of motor neuron and oligodendrocyte progenitors in the ventral spinal cord.* Cell Death Differ, 2012. **19**(2): p. 209-19.

27. Mateo, J.L., et al., *Characterization of the neural stem cell gene regulatory network identifies OLIG2 as a multifunctional regulator of self-renewal.* Genome Res, 2015. **25**(1): p. 41-56.

28. Fan, X., et al., *NOTCH Pathway Blockade Depletes CD133-Positive Glioblastoma Cells and Inhibits Growth of Tumor Neurospheres and Xenografts.* Stem cells (Dayton, Ohio), 2010. **28**(1): p. 5-16.

29. Marumo, T., et al., *Notch signaling regulates nucleocytoplasmic Olig2 translocation in reactive astrocytes differentiation after ischemic stroke.* Neuroscience Research, 2013. **75**(3): p. 204-209.

30. Wichterle, H., et al., *Directed differentiation of embryonic stem cells into motor neurons.* Cell, 2002. **110**(3): p. 385-97.

CHAPTER 2

LITERATURE REVIEW: MOLECULAR AND EXTRACELLULAR CUES IN MOTOR NEURON SPECIFICATION AND DIFFERENTIATION[1]

[1]Swetenburg, R.L., Stice, S.L. and L. Karumbaiah. *Molecular and Cellular Therapies for Motor Neuron Diseases*. Boulis, N, O'Connor, D. and A. Donsante, Eds. 2017. p. 2-24 Reprinted here with permission of the publisher.

Introduction

Motor neurons (MN) are a diverse group of cells without which complex life would not be possible. MN are responsible for integrating signals from the brain and the sensory systems to control voluntary and involuntary movements. Though MN can be split into cranial and spinal subsets, this chapter will focus on spinal MN, as they are a key target of disease and injury. As such, MN are the focus of regenerative efforts to alleviate these public health burdens. During late gastrulation and neurulation, the developing spinal cord, termed the neural tube, is patterned into distinct progenitor domains. MN are specified from progenitors in the ventral neural tube. Once specified, newly born MN are further specified into columns, pools and subtypes, forming a unique topography. From these columns and pools, axons reach out to their targets under varying guidance cues. All MN are cholinergic cells which integrate with the motor control circuit, the sensory system and their outlying targets to control movement. MN are unique in that their targets lie outside the central nervous system (CNS), meaning they require novel methods for seeking out and synapsing on them. Here, we present an overview of MN differentiation and development. We will focus mainly on signaling events, transcription factor markers, and the extracellular matrix as they pertain to MN development. These cells are targets of permanent and often deadly diseases including amyotrophic lateral sclerosis, spinal muscular atrophy, multiple sclerosis, and injuries like spinal cord injury. Only by understanding how these cells progress through development can we understand how to treat these maladies which currently have little hope for a cure. Further, by decoding the major events and players in development, we can better recapitulate them *in vitro* for cell replacement therapy, or harness the

underlying principles for regeneration in the adult. Given the growing importance of the MN-glia interaction in a number of neurodegenerative diseases, we will also discuss the initial specification of oligodendrocyte precursor cells in detail, as they share a common progenitor with MN.

Specification of Neuroectoderm

Vertebrate embryos specify the ectoderm in late gastrulation. This germ layer will become the epidermis and the nervous system. The anterior neural ectoderm is distinguished from the epidermis by its inability to bind bone morphogenic proteins (BMP) due to the inhibitors secreted from the Spemann-Mangold organizer region of the gastrula[31]. These inhibitors- noggin, chordin and follistatin- bind and neutralize the effects of bone morphogenetic proteins (BMP), creating a permissive transcriptional environment for neural progression[32-35]. Posteriorly, the neural plate is specified by fibroblast growth factors (FGF) and Wingless-related integration site (Wnt) proteins that also suppress BMP activity[36]. Additionally, retinoid signaling from the paraxial mesoderm specifies the cells of the future spinal cord[37]. This newly specified neural plate then thickens as cells proliferate and invaginates through convergent extension, forming the neural groove. The neural groove forms hinge points which will ultimately close to form the neural tube- the precursor for the entire central nervous system[38]. For an in-depth review, see Massarwa, et al.[39].

Spinal Cord Patterning

The spinal cord is a two-way information conduit that connects the brain with the sensory and motor systems. To do this, it must generate a highly diverse set of neurons during development. The neural tube provides a three dimensional template which is

patterned by gradients of morphogens to generate this diversity. The early neural tube is composed of multipotent neural stem cells expressing Sex determining region Y box 1 (Sox1)[40]. The dorsal neural tube will generate cells linking the central nervous system to the sensory peripheral nervous system. The ventral neural tube will ultimately give rise to the motor control circuit responsible for controlling motor neurons. Bone morphogenetic proteins specify the dorsal portion of the neural tube, including neuronal subtypes involved in integration of the peripheral sensory nervous system. Ventrally, an initial wave of Sonic hedgehog (Shh) from the notochord patterns the cells into distinct progenitor domains[2]. These domains arise due to cross-repressive actions of two types of transcription factors downstream of Shh signaling: Type I transcription factors are repressed at threshold Shh concentrations, while Type II are expressed under it[2] (Fig. 2.1A). The type I transcription factor paired box protein 6 (Pax6) represses the activity of type II homeobox protein Nkx2.1. Similarly, type II homeobox Nkx6.1 cross-represses developing brain homeobox 2 (Dbx2)[2]. Most ventral progenitor domain is the floor plate, which is induced to secrete Shh in a second wave of patterning, followed by the progenitor domains p3, pMN, p2, p1 and p0 (Fig 2.1B). The combinatory actions of these two classes of proteins yield the five spatially distinct ventral progenitor domains.

The pMN domain and Initial Neurogenesis

The motor neuron progenitor (pMN) domain is responsible for generating motor neurons (MN). In mice and chick models, this domain is identified by the expression of the homeobox transcription factors Nkx6.1 and Pax6 and the basic helix-loop-helix (bHLH) oligodendrocyte transcription factor 2 (Olig2)[41]. Olig2 expression is obligate

for MN specification, as Olig2^{null} mice fail to generate MN[42]. Initially, Olig2 plays a key role in progenitor proliferation, however it also drives the expression of neurogenin 2 (Ngn2)[43], a key neural determinant. The first murine MN are born around E9.5[42]. The homeobox transcription factor Nkx2.2, important for the glial switch and a marker for p0 cells, shows variable expression in humans compared to mouse and chick models: the human pMN domain appears to include both are Olig2+/Nkx2.2- as well as Olig2+/Nkx2.2+ cells[44]. This could potentially add to the diversity of human MN.

Molecular Programs in Newborn MN

As mentioned above, Olig2 drives Ngn2 expression. However, Ngn2 is ultimately responsible for cell cycle exit and neurogenesis[16, 17] in direct contrast to the role of Olig2. Once Ngn2 protein levels surpass those of Olig2, cell cycle exit occurs and cells commit to the neuronal lineage. Olig2 binds and sequesters the MN transcription factor homeobox gene 9 (Hb9, also called MNX1), which is necessary for MN development[17]. LIM homeobox gene Isl1 and LIM homeobox 3 (Lhx3) form a complex with the nuclear LIM interactor (NLI) which suppresses interneuron fate and specifies MN[45]. Along with Ngn2, this complex stimulates Hb9, which self-stimulates its own expression[46], while forming a positive feedback loop with Isl1. Isl1 and 2 work in concert to further specify MN cell fate[47]. Lhx3 and Isl1 expression is necessary for MN generation and the expression of cholinergic genes common to all MN[48]. However, little is known about potential negative feedback mechanisms in this differentiation process that would limit MN number and organ size. We will discuss this further in the glial switch section.

In summary, Shh secreted from notochord drives the expression of Pax6 and Nxk6.1, which in turn drive Olig2 expression. Olig2 expression delineates a mitotic pMN progenitor. Olig2 induces the expression of Ngn2, which is responsible for cell cycle exit, of Lhx3/Isl1 transcription factors, as well as motor neuron-specific Hb9 in newborn, post-mitotic MN (Fig 2.2).

Migration

The topography of MN largely correlates to their function. MN cluster in columns with similar transcription factor expression and like targets. Within muscle-innervating columns, there are MN pools which innervate specific muscle groups. In order to specify this topography, MN must migrate away from the ventricular progenitor cells to their final destination in the ventral horn of the spinal cord. Newly-born neurons detach from the epithelium and migrate radially to the medial and lateral areas of the neural tube. Critical to this migration is cadherin expression driven by beta and gamma catenin signaling in a Wnt-independent manner. In knockout models of either cadherin, MN fail to properly align to their proper column, although their ultimate muscular targets are not disrupted[49]. This implies that the stereotypic and highly organized topology of MN is not a modulator of identity or function. The role of this highly specific organization has yet to be elucidated. Transcriptionally, the forkhead box P (Foxp) genes regulate cadherin expression for migration to occur. Specifically, the Foxp2/4 genes allow for the detachment of MN from the neuroepithelium by downregulating cadherin 2 and allow them to migrate towards their final location by further modulation[50]. Although cell bodies migrate within the spinal cord, all MN soma are exclusively contained within the spinal cord. Recently, Isl1/2 has been shown to play an integral part

of preventing the cell body from exiting the spinal cord[51]. In knockout animals, MN soma successfully exited the spinal cord into the periphery[51]. One potential mechanism is through the sempahorin-neuropilin repulsive signaling pathway common to axon guidance, as neuropilin was found to be regulated by Isl1/2[51]. For an in-depth review of migration and topography, please see Kania (2005)[52].

MN Subtypes and Targets

MN that innervate similar regions of the body group together in columns with identical molecular properties. The rostrocaudal axis is specified externally by retinoic acid at the cervical and brachial regions and by growth differentiation factor (GDF11) and FGF8 at the thoracic and lumbar regions[53]. Like much of the developing embryo, this rostrocaudal positional identity is specified internally by Hox gene activation in response to these external cues to delineate the types of MN in a given region[54]. Hox expression is summarized in Figure 2.3. Hoxc9 plays a critical role in the organization of the spinal cord by repressing limb-specific Hox genes, thus specifying the thoracic column[55]. Within each column, MN organize into pools which innervate distinct muscles. Hox genes work in concert with the Hox accessory factor Foxp1 to specify many of the columns and establish motor pools within columns[56]. Notably, in the absence of Foxp1 in knockout animals, there is a lack of defined rostrocaudal motor columns[56], further strengthening the case for its role in the positional identity of motor columns.

Somatic Motor Neurons

MN can be separated into somatic and visceral motor columns based on their targets. Somatic motor neurons synapse directly onto muscles, including the body wall,

limbs and diaphragm. These include the phrenic motor column, medial motor column, hypaxial motor column, spinal accessory column and lateral motor column. The variation in transcription factors expressed in these different columns most likely correlate to function. However, much work is needed to fully understand what the initial cues are triggering these regulators and how they can account for such a diverse set of cells.

The phrenic motor column, located cervically, controls the diaphragm and respiratory actions. This column is specified by Isl1/2, Hb9 and homeobox gene Pou3F1 under the control of Hox5[57].

The spinal accessory motor column is located cervically and controls the muscles of the jaw and neck. These neurons are specified under the homeobox transcription factors Nkx9.2 and Nkx2.2[58] and require expression of paired like homeobox 2b (Phox2b)[59].

Medial motor column (MMC) neurons innervate the muscles of the back and are unique in that they are present throughout the spinal cord, not being restricted to one region or under the influence of Hox genes. These cells in this column all express Hb9, Isl1/2 and are the only neurons to retain Lhx3 expression after specification[60]. Lhx3 is thought to play an important role in overcoming Hox regionalization[56]. These neurons also do not express Foxp1[56], which likely aids in escaping Hox control.

Body wall and abdominal muscles are innervated by the hypaxial motor column, located only in the thoracic region. These cells express Hb9, Isl1, Ets variant 1 (Etv1), and low levels of Isl2, while being negative for Foxp1[56]. Like the MMC, the lack of

Foxp1 expression likely aids in their ability to escape Hox regionalization in order to span a large part of the spinal cord.

Limb-innervating neurons are found in either the brachial or lumbar region in the lateral motor column (LMC). This can be further subdivided into the medial (LMCm) and lateral (LMCl) regions that innervate ventral and dorsal muscles, respectively, during development. Further specification includes the type of muscle innervated. These cells express Isl2, Foxp1 and the aldehyde dehydrogenase family gene Aldh1A2, a protein involved in retinoic acid synthesis, while downregulating Lhx3 [56]. Recently, the Onecut transcription factor family has been implicated in LMCm and LMCl fate decisons[61]. Conditional dicer knockouts result in a severe reduction of LMC MN through apoptosis, implicating miRNA as a key determinant in their survival[62].

There are three types of MN located within a pool synapsing on a specific muscle group: alpha, beta and gamma. Alpha MN innervate extrafusal muscles and cause muscle contraction, including reflex responses[63], synapsing on fast-twitch fatigable, slow-twitch fatigue-resistant and fast-twitch fatigue resistant fibers[64]. Beta MNs innervate both extra- and intrafusal muscle fibers, though their identity and role are poorly understood[65]. Gamma MNs synapse on intrafusal fibers to modulate muscle sensitivity[63]. Gamma MN are a distinct subset and can be identified by the secretion of Wnt7a[66].

Visceral Motor Neurons

As opposed to somatic MN, visceral MN regulate the autonomic nervous system and are found in the thoracic level of the spinal cord in the pre-ganglionic column. These are unique in that they do not synapse on muscles, but rather the ganglia of the peripheral

nervous system. Through this, they are able to regulate smooth muscle, cardiac muscle and glandular activity. These cells express mothers against decapentaplegic homolog 1 (Smad1)[56], nitric oxide synthase 1 (NOS1)[67], Smad interacting protein 1 (Sip1)[61] and low levels of Foxp1[56]. The presence of Sip1 and Smad1 imply an important role for BMPs, possibly by distinguishing them from the somatic MN during specification. Isl2 is downregulated to specify this cell type[47]. Recently, the Onecut family of factors which drive Isl1 were revealed to play an important role in visceral/somatic fate decisions[61]. In the more caudal regions, preganglionic motor column neurons regulate the parasympathetic system by projecting to ganglia near their target organs, while in the thoracic regions, they synapse on the ganglia in proximity to the spine to regulate the sympathetic systems of the body.

Axon Targeting

MN axons must exit the CNS in order to project onto their targets. A small subset of MN, specifically the spinal accessory column, exit dorsally through the lateral exit point[68]. These neurons express the netrin receptor, and are repelled from the midline of the spinal cord which expresses netrin-1[68]. However, most MN axons exit ventrally, driven by the chemokine C-X-C motif receptor 4 (Cxcr4) expressed on the neurons and its ligand chemokine C-X-C ligand 12 (Cxcl12) located in the ventral paraxial mesoderm[69]. Once the axons have exited, they are directed toward the body wall, the limbs, the muscles of the back, or the autonomic ganglia, which will ultimately determine which motor column they will become. MMC MN express ephrinA 3 and 4 receptors (EphA3/4) which repel them from the ephrin-A1 (Efna1)-secreting dorsal root ganglia to continue to the back muscles[70]. These neurons express fibroblast growth factor

receptor 1 (Fgfr1), which is thought to direct them, as well[71]. LMC, the limb-innervating MN, use a semaphorin-neuropilin complex in timing the invasion of the limb[72]. Once they have reached the limb bud, LMCl neurons express EphA4 receptor[73]. Ephrins in the ventral limb repel these neurons and they extend to the dorsal limb. LMCm express EphB1 and are similarly repelled from the dorsal limb which expresses ephrinB[74]. Though many of the mechanisms are poorly understood, understanding how axons migrate to their targets will be important for cell replacement therapies.

Once axons reach their target muscle, extrinsic factors play a critical role in finalizing the connections. Muscle-derived glial cell-line derived neurotrophic factor (Gdnf), specifically, drives Ets variant 4 (Etv4) which induces MN to arborize and innervate muscle fibers[75]. The Onecut gene family involved in MN specification has additionally been identified as a transcriptional regulator of neuromuscular junction formation[76]. For a review on axon guidance, see Stifani (2014)[64].

Extracellular Matrix and the Nervous System

The extracellular matrix (ECM) of the nervous system plays an important role in facilitating neuronal migration and axonal pathfinding during central and peripheral nervous system (CNS, PNS) development. The nervous system ECM is compositionally distinct, consisting of markedly lesser quantities of fibrous proteins such as collagens, and fibronectins, and displaying a higher concentration of glycoproteins and proteoglycans when compared to the ECM of other systemic tissues. The contribution of CNS and PNS ECM components to neuronal function and homeostasis, emphasizing MNs, are presented in this section.

Collagen

In contrast with other tissue specific ECMs, collagen type IV is the only collagen found in the CNS ECM. A majority of the collagen IV in the CNS ECM self-polymerizes along with fibronectin and laminin to form the basement membrane, which serves as a protective barrier between the vascular endothelial cells and the parenchyma of the brain [77, 78]. Collagen IV is also associated with the neural interstitial matrix, where it is found in small amounts along with small amounts of other such adhesive glycoproteins such as fibronectin and laminin, and sulfated glycoproteins such as entactin[78]. These minor components are interlinked within a major network of chondroitin sulfate proteoglycans (CSPGs), hyaluronic acid (HA), and tenascin, which make up the bulk of the neural interstitial matrix.

Collagens in the PNS are broadly classified into the fibrillary type I, III, and V collagens and the basement membrane associated type IV collagen[79]. The fibrillary collagens play an important role in supporting myelinating Schwann cell function. Long-term (14-28 day) *in vitro* cultures of MN in 3D type I &III collagen scaffolds produced elongated neurites of ~850 μm in length with thick myelin sheaths, indicating that trophic support provided by fibrillary collagens is essential for MN growth[80]. On the contrary, dysregulated fibrillary collagen associated with scar tissue formed after PNS injury is considered to be a major barrier to nerve regeneration[79].

Laminin

Laminins are large (~800 kDa) ECM associated glycoproteins thought to be essential for neuronal migration and axonal pathfinding during development. They are heterotrimeric molecules consisting of α, β, and γ chains. These chains present

themselves in a variety of different combinations to result in as many as 18 distinct laminin isoforms, a majority of which are present in the nervous system ECM[81]. S-laminin is a homolog of the B1 subunit of laminin. It is known to facilitate motor neuron adhesion, and plays an important role in the formation of neuromuscular junctions. In the developing CNS, S-laminin and laminin are both found to be present in the subplate in the cerebral cortex[82]. This situation changes dramatically in the adult CNS, which is marked by the disappearance of S-laminin, and the restricted expression of laminin to the basement membrane, where it is found in close association with collagen and heparan sulfate proteoglycans (HSPGs)[78].

Laminins are important constituents of the PNS basement membrane found surrounding Schwann cells. As integral adhesive and growth promoting constituents of the basement membrane, they are believed to organize together the meshwork of structural proteins to form the substratum upon which neuronal migration and axonal pathfinding can take place[83]. The diversity of laminin isoforms can be advantageous in regulating the selective attachment of motor neurons, which is reportedly mediated by the S-laminin specific LRE (leucine-arginine-glutamic acid) amino acid sequence[84].

Fibronectin

Fibronectins are ECM proteins known to play specific roles in neuronal migration during development and after injury[81]. Like laminin, they are large glycoproteins consisting of functional domains that facilitate cellular and ECM interactions[85]. In the CNS they are associated with the basement membrane where they are known to interact with collagen, HSPGs, and tenascin[86]. Fibronectin in the PNS is specifically upregulated after injuries. This is also accompanied by the upregulation of $\alpha_5\beta_1$ integrin

on the cell membranes of regenerating MN and Schwann cells[81], which is necessary for blood vessel development, pointing to the role of fibronectin in facilitating PNS repair.

Proteoglycans and Glycosaminoglycans

Proteoglycans such as CSPGs and HSPGs, and their associated sulfated glycosaminoglycans (GAGs), as well as unsulfated GAGs such as HA constitute the majority of the CNS ECM. High molecular weight HA forms the diffuse meshwork to which CSPGs, HSPGs, tenascins and other fibribrous ECMs proteins are linked together. This network is more condensed around presynaptic terminals, nodes of Ranvier, and around the perineuronal nets (PNNs) that surround inhibitory interneurons[87].

Chondroitin sulfate proteoglycans (CSPGs)

Sulfated CSPGs belonging to the lecitican family (aggrecan, versican, neurocan, and brevican) are the most abundant CSPGs associated with the CNS ECM and play a major role in regulating neuronal plasticity. They are large proteins consisting of multiple domains capable of specifically binding HA, tenascin, and other ECM components. The associated CS-GAG sidechains can be sulfated at various positions, resulting in a complex configuration of sulfated GAGs that are capable of mediating a variety of different functions, some of which include receptor and growth factor binding[88, 89]. The oversulfated CS-GAG CS-4,6 sulfate (CS-E) is a potent neurite repellant that is specifically upregulated after CNS injury[90, 91]. Nerve repulsive CSPGs are also believed to regulate axonal regeneration following PN crush injury, where they are found to bind and inhibit the growth promoting activity of laminin[92].

Heparan sulfate proteoglycans (HSPGs)

In contrast to the predominantly nerve repulsive role played by CSPGs, large basement membrane associated HSPGs such as perlecan are known to complex with laminin to induce neurite outgrowth[93]. However, in the context of neurodegenerative diseases such as Alzheimer's disease, HSPGs are thought to exacerbate the formation of amyloid-β and prevent its proteolytic degradation[94]. In the PNS, HSPGs such as glypican-1 are upregulated in the dorsal root ganglia after sciatic nerve transection, where it is believed to promote target MN reinnervation[95].

Hyaluronic acid (HA)

HA is an unsulfated GAG that interacts with CD44 and other cell surface receptors in the brain ECM[96]. HA is abundantly found in the neural interstitial matrix where it is complexed with CSPGs. The upregulation of HA in response to CNS injuries is believed to inhibit remyelination of neurons. However, the role of HA in directly influencing these outcomes remains to be elucidated owing to the fact that it is often bound to CSPGs[78]. Recent studies have indeed demonstrated that the enzymatic degradation of HA by the hyaluronidase PH20, but not other hyaluronidases, results in digestion products that can further impede remyelination[97]. In the PNS, HA is found to be densely deposited at the nodes of Ranvier in PN axons[98]. Previous studies evaluating the regenerative potential and function of transected sciatic nerves treated with HA report significant improvements in nerve conduction velocity and muscle mass, and a significant reduction in scarring when compared to saline treated animals[99]. These seemingly contradictory functions point to the diverse roles played by HA in the CNS and PNS, and also highlight the importance of the role of enzymatic degradation of these GAGs in regulating these end outcomes.

MN Cell Death

The developing spinal cord makes MN in excess, with about 40% undergoing cell death[100]. Almost all MN are specified before this death begins. This phenomena was observed when the removal of a limb bud led to an increased death in MN[101], leading to the neurotrophic theory: that pro-survival molecules exist in limited quantities during development allowing for selected survival or programmed cell death of neurons[102]. During development, different MN subtypes require different cocktails of factors to survive. The best studied of these is Gdnf. Gdnf is expressed by skeletal muscles and can be transported retro- and anterogradely[103, 104]. Gdnf binds its receptor, the tyrosine kinase Ret, as well as the GFRalpha1 receptor[105]. Exogenous brain-derived neurotrophic factor (Bdnf) also enhances MN survival but is not required[106]. Other factors include ciliary neurotrophic factor (Cntf), neurotrophic factor (Ntf), leukemia inhibitory factor (Lif), hepatocyte growth factor (Hgf), insulin-like growth factor (Igf) and vascular endothelial growth factor (Vegf)[107].

The Glial Switch

The pMN domain which generates MN also generates oligodendrocyte precursor cells (OPC). During progenitor and MN specification, Olig2 and Nkx2.2 cross-repress each other to establish the pMN-p3 border[8]. However, Olig2 and Nkx2.2 are co-expressed during the oligodendrogliogenic phase of development with Olig2 being necessary for oligodendrocyte production[12] and Nkx2.2 knockouts yielding extremely depleted oligodendrocyte pools[108]. Olig2 overexpression alone is insufficient for OPC generation; however, dual overexpression with Nkx2.2 leads to an increase in OPCs from this domain[109]. This switch from cross-repression to co-expression suggests that there

is a common convergence of extracellular signaling focusing on the simultaneous activation of these two transcription factors. Interestingly, dicer inactivation leads to a high loss of OPCs, implicating miRNA as a key determinant in OPC specification[62]. One hallmark of the neurogenic to gliogenic switch is a downregulation of pro-neural genes, specifically Ngn2[110]. Olig2 is a basic helix-loop-helix (bHLH) repressor and its phosphorylation state affects protein-protein binding kinetics. Olig2 is typically phosphorylated at Ser147 during MN differentiation, while the site is dephosphorylated during OPC specification. Abolishing the phosphorylation site blocks MN differentiation, while having no effect on OPCs. The proposed mechanism of action involves homodimerization of Olig2 during neurogenesis and heterodimerization during oligodendrogliogenesis[15].

Floor plate cells play a critical role in OPC specification. In zebrafish, the floor plate secretes Indian hedgehog b (Ihhb), which is necessary for OPC specification in a Shh independent manner[111]. Another role for the floor plate in mouse and chick models is secretion of sulfatase 1, which positively regulates Shh signaling through heparin sulfate proteoglycan (HSPG) modifications, potentially by triggering a dorsal shift in perceived Shh levels, thereby increasing Nkx2.2 (expressed under high concentrations of Shh) in cells already expressing Olig2 (e.g. in the pMN domain)[112]. Notch-Delta is a form of cell-cell juxtacrine signaling and is additionally implicated in progenitor fate determination. However, findings here have been contradictory. In zebrafish, Notch signaling has been shown to increase OPCs[113], while in the chick, attenuation of Notch signaling through its ligand Jagged2 enhanced OPC generation[26].

Notch has been shown to induce cell cycle exit[23], which implies a permissive, rather than instructive role for Notch-Delta in OPC specification.

Elegant modeling work in the olfactory bulb has shown a negative feedback system in which committed neuronal cells influence both progenitor cell renewal and neuronal/glial fate decisions[114]. Gokoffski and coworkers show that committed neuronal cells secrete transforming growth factor-β (Tgf-β) family proteins (Activin β-B and GDF11) which inhibit progenitor populations from expanding, while this is countered by production of Tgf-β inhibitors (follistatin) from the progenitor cells themselves. Therefore, when neuronal signals outnumber progenitor signals (e.g. after neuronal populations and signaling reach a threshold), the progenitor cells exit the cell cycle and differentiate towards glia. The study also showed that Tgf-β signaling could upregulate Achaete-Scute family bHLH transcription factor 1 (Ascl1), which is necessary for OPC specification in the ventral neural tube[115]. While this study examined olfactory bulb, similar feedback mechanisms may be at play in the neural tube[116]. Recently, Tgf-β has been implicated in the glial switch in the spinal cord making it a strong candidate for further study[9].

Generating MN from Pluripotent Stem Cells

Regenerative medicine requires either deriving cell types *in vitro* for transplantation or understanding the cues governing development to generate lost or injured cell types from endogenous stores of progenitors. The study and optimization of pluripotent stem cell (PSC) differentiation into MN progenitors, MN and oligodendrocytes is of the utmost importance in realizing these cures, while serving the dual purpose of acting as developmentally relevant models which are easier to interrogate

than embryos *in utero*. Much of the groundbreaking work that led to the initial decoding of *in vivo* MN specification also led to the first derivation of MN from PSCs. Murine MN were induced from PSCs using retinoic acid (RA) and Shh. When they were transplanted into mice, they were able to synapse onto muscles[30]. *In vitro,* these cells are electrophysiologically active and form neuromuscular junctions with myocytes[117]. Human MN have also been derived from embryonic stem cells[118, 119]. Shh mimics, including purmorphamine[120, 121]and HH-ag1.3[117] have been used to increase the efficiency and decrease cost of MN generation from PSCs *in vitro*. More recently, Smad inhibition greatly increased the yield of neural stem cells from embryonic stem cells and has been used in concert with RA and Shh cues to generate MN[122].

With the advent of induced pluripotent stem cells (iPSC) offering patient specific treatment hopes[123], human iPSCs were also shown to generate MN *in vitro* under developmental cues including RA and Shh[121]. Murine iPSCs were shown to mature and integrate into chick spinal cord by histological analysis[124]. Optogenetic neuronal control[125] has provided further proof that transplanted PSC derived MN can directly restore function to limb muscles[126].

Exogenous gene expression has also been used to increase the efficiency of MN differentiation in addition to, or instead of, external patterning factors. Exogenous expression of Isl1 and Lhx3 has been shown to more efficiently transform ESCs to MN than Shh alone[45]. ESCs can be directly converted to MN with as little as three factors: Ngn2, Isl1 and Lhx3[127]. MN can be transdifferentiated from fibroblasts, as well, with the input of three groups of factors: fibroblast to neuronal factors, pMN progenitor factors, and MN transcription factors[128].

However, once MN are initially specified, further differentiation into specific columns or pools has proved challenging, though some gains have been made in this area. Alterations to protocols can drastically alter MN subtype. RA addition to murine PSC cultures results in cervical MN[30]. Though RA addition is extremely efficient in producing cervical MN from PSCs[30], it is interesting to note that MN can be specified *in vitro* in the absence of retinoid signaling, leading to greater malleability in later specification and maturation toward a wider variety of subtypes[129]. For instance, FGF and GDF11 addition push MN to a more caudal identity[53]. In human MN derivation, the use of purmorphamine and smoothened agonist (SAG), when compared to recombined Shh protein, results in the shift in columnar identity from MMC to LMC[130]. Importantly, transplanted MN can develop into appropriate thoracic and lumbar fates when transplanted into the corresponding location in the embryonic spinal cord[131]. Recently, efficient generation of LMC and MMC MN was achieved through exogenous Foxp1 expression[132], likely by escaping Hox gene regionalization.

When there is no precedent for generating a specific MN subtype from PSCs, there are combined *in vivo* and *in vitro* methods for delineating transcriptional regulation. For instance, in the difficult to study phrenic motor column, Machado and coworkers[133] isolated these MN *in vivo* and compared their gene expression with control MN using microarray analysis. Putative determinants based on this analysis were then exogenously expressed in PSCs followed by another round of comparative analysis. Through this systematic approach, Pou3f1 and Hoxa5, as well as Notch signaling, were all found to be key determinants of phrenic motor column identity. Future studies will

further elucidate methods for generating the vast diversity of MN for cell transplantation studies and disease and developmental modeling.

PSC-derived MN are a valuable tool for MN studies outside the context of an animal. Using microfluidics and stripe assays, Nedelec and coworkers were able to show growth cone collapse occurs through two separate mechanisms, one dependent and one independent of local protein synthesis, in response to semaphorins in both human and murine cell lines[134]. PSC-derived MNs make excellent candidates for drug screening, as well, particularly in human derived cells where *in vivo* tests are inappropriate and iPSCs can be generated from patients. For instance, in a large scale screen of small molecules, kenpaullone, an inhibitor of glycogen synthase kinase 3 and the mitogen-activated kinase pathway (MAP4K4), was recently shown to greatly increase the survival of iPSC-derived MN from an ALS patient[135].

Other developmental phenomena have been recapitulated using PSCs, including the fate decisions in pMN progenitors. A negative feedback mechanism appears to control this switch from neurogenesis to gliogenesis, while progenitor mitosis is triggered externally, rather than being an inherent quality[116]. Understanding these rules opens the door for regenerative medicine to regrow lost populations of progenitors, MN or OPCs within the adult body with simple cues.

Differences between human and mouse ESC differentiation has provided insights into species differences in developmental properties, as well. For instance, during neurogenesis human ESCs coexpress Olig2+ and Nkx2.2+ in a subset of MN progenitors. In contrast, murine ESC segregate these transcription factors until the gliogenic phase[44]. Differentiating stem cells into MN has even given new insights into how Shh

signaling occurs. For instance, exosomes containing integrins are necessary for Olig2 expression[136]. For a review of generating MN from PSCs, please see Davis-Dusenbery et al (2014)[137].

Generating Oligodendrocyte Precursor Cells from PSCs

Understanding oligodendrocyte differentiation from pluripotent stem cells is important in light of diseases that affect myelin, including multiple sclerosis and demyelination following spinal cord injury. Additionally, oligodendrocytes were the first human embryonic stem cell-derived cell type to be approved for clinical trial[138]. In fact, oligodendrocytes were generated from murine ES cells before motor neurons[139]. These ESC-derived oligodendrocytes myelinate axons both *in vitro* and *in vivo*. Human ESC-derived oligodendrocytes similarly remyelinated axons when transplanted[140]. Recently, there has been an emphasis on transplanting neural stem and progenitor cells to an injured or diseased site. It is interesting to note that most of the daughter cells from these transplants develop into glia[141-143], which means understanding the glial switch will better inform the ways in which these cells are transplanted. Compared to murine PSCs, oligodendrocytes derived from human ESC show divergence in their response to FGF signaling[144], implying that these processes are not wholly conserved between species. Most oligodendroglial specification protocols are similar to MN derivation protocols using RA and Shh to specify pMN cells, however they often require long amounts time[145, 146]. This approach likely works by eliminating neural progenitors through division and neurons through unfavorable culture conditions. It is interesting to note that oligodendrocyte precursor cells can be coerced to generate type I and II astrocyte *in vitro* through Notch signaling[147]. In addition to remyelination, OPC

transplantation has been shown to decrease neuropathic pain after spinal cord contusions, a beneficial side effect for further transplantation studies[148]. OPCs have been generated from fibroblasts through the expression of transcription factors Sox10, Olig2 and Zfp536[149]. For an in-depth review of OPC development into mature oligodendrocytes, please see Alsanie, et al (2013)[150].

Conclusion

Our current understanding of the journey from neuroectodermal specification to fully mature motor neuron has provided an excellent road map to the diversification of neuronal identity as well as presented many clues for potential cell replacement and regenerative therapies. However, much work remains, both *in vitro* and *in vivo,* to fully understand the mechanisms governing these essential cells and make these treatments a reality.

References

1. Hamburger V. Ontogeny of neuroembryology. *The Journal of neuroscience : the official journal of the Society for Neuroscience.* 1988;8(10):3535-3540.
2. Smith WC, Knecht AK, Wu M, Harland RM. Secreted noggin protein mimics the Spemann organizer in dorsalizing Xenopus mesoderm. *Nature.* 1993;361(6412):547-549.
3. Hemmati-Brivanlou A, Kelly OG, Melton DA. Follistatin, an antagonist of activin, is expressed in the Spemann organizer and displays direct neuralizing activity. *Cell.* 1994;77(2):283-295.
4. Hemmati-Brivanlou A, Melton DA. Inhibition of activin receptor signaling promotes neuralization in Xenopus. *Cell.* 1994;77(2):273-281.
5. Sasai Y, Lu B, Steinbeisser H, Geissert D, Gont LK, De Robertis EM. Xenopus chordin: a novel dorsalizing factor activated by organizer-specific homeobox genes. *Cell.* 1994;79(5):779-790.
6. Stern CD. Neural induction: old problem, new findings, yet more questions. *Development.* 2005;132(9):2007-2021.
7. Novitch BG, Wichterle H, Jessell TM, Sockanathan S. A requirement for retinoic acid-mediated transcriptional activation in ventral neural patterning and motor neuron specification. *Neuron.* 2003;40(1):81-95.
8. Colas JF, Schoenwolf GC. Towards a cellular and molecular understanding of neurulation. *Developmental dynamics : an official publication of the American Association of Anatomists.* 2001;221(2):117-145.

9. Massarwa R, Ray HJ, Niswander L. Morphogenetic movements in the neural plate and neural tube: mouse. *Wiley interdisciplinary reviews. Developmental biology.* 2014;3(1):59-68.

10. Zhang X, Huang CT, Chen J, et al. Pax6 is a human neuroectoderm cell fate determinant. *Cell stem cell.* 2010;7(1):90-100.

11. Jessell TM. Neuronal specification in the spinal cord: inductive signals and transcriptional codes. *Nature reviews. Genetics.* 2000;1(1):20-29.

12. Novitch BG, Chen AI, Jessell TM. Coordinate regulation of motor neuron subtype identity and pan-neuronal properties by the bHLH repressor Olig2. *Neuron.* 2001;31(5):773-789.

13. Lu QR, Sun T, Zhu Z, et al. Common developmental requirement for Olig function indicates a motor neuron/oligodendrocyte connection. *Cell.* 2002;109(1):75-86.

14. Ma YC, Song MR, Park JP, et al. Regulation of motor neuron specification by phosphorylation of neurogenin 2. *Neuron.* 2008;58(1):65-77.

15. Marklund U, Alekseenko Z, Andersson E, et al. Detailed expression analysis of regulatory genes in the early developing human neural tube. *Stem Cells Dev.* 2014;23(1):5-15.

16. Mizuguchi R, Sugimori M, Takebayashi H, et al. Combinatorial roles of olig2 and neurogenin2 in the coordinated induction of pan-neuronal and subtype-specific properties of motoneurons. *Neuron.* 2001;31(5):757-771.

17. Lee SK, Lee B, Ruiz EC, Pfaff SL. Olig2 and Ngn2 function in opposition to modulate gene expression in motor neuron progenitor cells. *Genes & development.* 2005;19(2):282-294.

18. Lee S, Cuvillier JM, Lee B, Shen R, Lee JW, Lee SK. Fusion protein Isl1-Lhx3 specifies motor neuron fate by inducing motor neuron genes and concomitantly suppressing the interneuron programs. *Proceedings of the National Academy of Sciences of the United States of America.* 2012;109(9):3383-3388.

19. Tanabe Y, William C, Jessell TM. Specification of motor neuron identity by the MNR2 homeodomain protein. *Cell.* 1998;95(1):67-80.

20. Thaler JP, Koo SJ, Kania A, et al. A postmitotic role for Isl-class LIM homeodomain proteins in the assignment of visceral spinal motor neuron identity. *Neuron.* 2004;41(3):337-350.

21. Cho HH, Cargnin F, Kim Y, et al. Isl1 directly controls a cholinergic neuronal identity in the developing forebrain and spinal cord by forming cell type-specific complexes. *PLoS Genet.* 2014;10(4):e1004280.

22. Demireva EY, Shapiro LS, Jessell TM, Zampieri N. Motor neuron position and topographic order imposed by beta- and gamma-catenin activities. *Cell.* 2011;147(3):641-652.

23. Rousso DL, Pearson CA, Gaber ZB, et al. Foxp-mediated suppression of N-cadherin regulates neuroepithelial character and progenitor maintenance in the CNS. *Neuron.* 2012;74(2):314-330.

24. Lee H, Kim M, Kim N, et al. Slit and Semaphorin signaling governed by Islet transcription factors positions motor neuron somata within the neural tube. *Exp Neurol.* 2015;269:17-27.

25. Kania A. Spinal motor neuron migration and the significance of topographic organization in the nervous system. *Advances in experimental medicine and biology.* 2014;800:133-148.

26. Liu JP, Laufer E, Jessell TM. Assigning the positional identity of spinal motor neurons: rostrocaudal patterning of Hox-c expression by FGFs, Gdf11, and retinoids. *Neuron.* 2001;32(6):997-1012.

27. Dasen JS, Jessell TM. Hox networks and the origins of motor neuron diversity. *Current topics in developmental biology.* 2009;88:169-200.

28. Jung H, Lacombe J, Mazzoni EO, et al. Global control of motor neuron topography mediated by the repressive actions of a single hox gene. *Neuron.* 2010;67(5):781-796.

29. Dasen JS, De Camilli A, Wang B, Tucker PW, Jessell TM. Hox repertoires for motor neuron diversity and connectivity gated by a single accessory factor, FoxP1. *Cell.* 2008;134(2):304-316.

30. Philippidou P, Walsh CM, Aubin J, Jeannotte L, Dasen JS. Sustained Hox5 gene activity is required for respiratory motor neuron development. *Nature neuroscience.* 2012;15(12):1636-1644.

31. Pabst O, Rummelies J, Winter B, Arnold HH. Targeted disruption of the homeobox gene Nkx2.9 reveals a role in development of the spinal accessory nerve. *Development.* 2003;130(6):1193-1202.

32. Hirsch MR, Glover JC, Dufour HD, Brunet JF, Goridis C. Forced expression of Phox2 homeodomain transcription factors induces a branchio-visceromotor axonal phenotype. *Developmental biology.* 2007;303(2):687-702.

33. Tsuchida T, Ensini M, Morton SB, et al. Topographic organization of embryonic motor neurons defined by expression of LIM homeobox genes. *Cell.* 1994;79(6):957-970.

34. Roy A, Francius C, Rousso DL, et al. Onecut transcription factors act upstream of Isl1 to regulate spinal motoneuron diversification. *Development.* 2012;139(17):3109-3119.

35. Chen JA, Wichterle H. Apoptosis of limb innervating motor neurons and erosion of motor pool identity upon lineage specific dicer inactivation. *Front Neurosci.* 2012;6:69.

36. Eccles JC, Eccles RM, Iggo A, Lundberg A. Electrophysiological studies on gamma motoneurones. *Acta physiologica Scandinavica.* 1960;50:32-40.

37. Stifani N. Motor neurons and the generation of spinal motor neuron diversity. *Frontiers in cellular neuroscience.* 2014;8:293.

38. Bessou P, Emonet-Denand F, Laporte Y. Motor fibres innervating extrafusal and intrafusal muscle fibres in the cat. *The Journal of physiology.* 1965;180(3):649-672.

39. Ashrafi S, Lalancette-Hebert M, Friese A, et al. Wnt7A identifies embryonic gamma-motor neurons and reveals early postnatal dependence of gamma-motor neurons on a muscle spindle-derived signal. *The Journal of neuroscience : the official journal of the Society for Neuroscience.* 2012;32(25):8725-8731.

40. Dasen JS, Liu JP, Jessell TM. Motor neuron columnar fate imposed by sequential phases of Hox-c activity. *Nature.* 2003;425(6961):926-933.

41. Dillon AK, Fujita SC, Matise MP, et al. Molecular control of spinal accessory motor neuron/axon development in the mouse spinal cord. *The Journal of neuroscience : the official journal of the Society for Neuroscience.* 2005;25(44):10119-10130.

42. Lieberam I, Agalliu D, Nagasawa T, Ericson J, Jessell TM. A Cxcl12-CXCR4 chemokine signaling pathway defines the initial trajectory of mammalian motor axons. *Neuron.* 2005;47(5):667-679.

43. Gallarda BW, Bonanomi D, Muller D, et al. Segregation of axial motor and sensory pathways via heterotypic trans-axonal signaling. *Science (New York, N.Y.).* 2008;320(5873):233-236.

44. Shirasaki R, Lewcock JW, Lettieri K, Pfaff SL. FGF as a target-derived chemoattractant for developing motor axons genetically programmed by the LIM code. *Neuron.* 2006;50(6):841-853.

45. Huber AB, Kania A, Tran TS, et al. Distinct roles for secreted semaphorin signaling in spinal motor axon guidance. *Neuron.* 2005;48(6):949-964.

46. Helmbacher F, Schneider-Maunoury S, Topilko P, Tiret L, Charnay P. Targeting of the EphA4 tyrosine kinase receptor affects dorsal/ventral pathfinding of limb motor axons. *Development.* 2000;127(15):3313-3324.

47. Luria V, Krawchuk D, Jessell TM, Laufer E, Kania A. Specification of motor axon trajectory by ephrin-B:EphB signaling: symmetrical control of axonal patterning in the developing limb. *Neuron.* 2008;60(6):1039-1053.

48. Helmbacher F, Dessaud E, Arber S, et al. Met signaling is required for recruitment of motor neurons to PEA3-positive motor pools. *Neuron.* 2003;39(5):767-777.

49. Audouard E, Schakman O, Rene F, et al. The Onecut transcription factor HNF-6 regulates in motor neurons the formation of the neuromuscular junctions. *PloS one.* 2012;7(12):e50509.

50. Burnside ER, Bradbury EJ. Manipulating the extracellular matrix and its role in brain and spinal cord plasticity and repair. *Neuropathol Appl Neurobiol.* 2014;40(1):26-59.

51. Lau LW, Cua R, Keough MB, Haylock-Jacobs S, Yong VW. Pathophysiology of the brain extracellular matrix: a new target for remyelination. *Nat Rev Neurosci.* 2013;14(10):722-729.

52. Koopmans G, Hasse B, Sinis N. Chapter 19: The role of collagen in peripheral nerve repair. *Int Rev Neurobiol.* 2009;87:363-379.

53. Gingras M, Beaulieu MM, Gagnon V, Durham HD, Berthod F. In vitro study of axonal migration and myelination of motor neurons in a three-dimensional tissue-engineered model. *Glia.* 2008;56(3):354-364.

54. Venstrom KA, Reichardt LF. Extracellular-Matrix .2. Role of Extracellular-Matrix Molecules and Their Receptors in the Nervous-System. *Faseb J.* 1993;7(11):996-1003.

55. Hunter DD, Llinas R, Ard M, Merlie JP, Sanes JR. Expression of s-laminin and laminin in the developing rat central nervous system. *The Journal of comparative neurology.* 1992;323(2):238-251.

56. Hohenester E, Yurchenco PD. Laminins in basement membrane assembly. *Cell Adhes Migr.* 2013;7(1):56-63.

57. Hunter DD, Cashman N, Morris-Valero R, Bulock JW, Adams SP, Sanes JR. An LRE (leucine-arginine-glutamate)-dependent mechanism for adhesion of neurons to S-laminin. *J Neurosci.* 1991;11(12):3960-3971.

58. Rutka JT, Apodaca G, Stern R, Rosenblum M. The extracellular matrix of the central and peripheral nervous systems: structure and function. *J Neurosurg.* 1988;69(2):155-170.

59. Ingham KC, Brew SA, Erickson HP. Localization of a cryptic binding site for tenascin on fibronectin. *J Biol Chem.* 2004;279(27):28132-28135.

60. Bruckner G, Brauer K, Hartig W, et al. Perineuronal nets provide a polyanionic, glia-associated form of microenvironment around certain neurons in many parts of the rat brain. *Glia.* 1993;8(3):183-200.

61. Sugahara K, Mikami T. Chondroitin/dermatan sulfate in the central nervous system. *Curr Opin Struct Biol.* 2007;17(5):536-545.

62. Deepa SS, Umehara Y, Higashiyama S, Itoh N, Sugahara K. Specific molecular interactions of oversulfated chondroitin sulfate E with various heparin-binding growth factors. Implications as a physiological binding partner in the brain and other tissues. *J Biol Chem.* 2002;277(46):43707-43716.

63. Brown JM, Xia J, Zhuang B, et al. A sulfated carbohydrate epitope inhibits axon regeneration after injury. *Proc Natl Acad Sci U S A.* 2012;109(13):4768-4773.

64. Karumbaiah L, Anand S, Thazhath R, Zhong Y, McKeon RJ, Bellamkonda RV. Targeted downregulation of N-acetylgalactosamine 4-sulfate 6-O-sulfotransferase

significantly mitigates chondroitin sulfate proteoglycan-mediated inhibition. *Glia.* 2011;59(6):981-996.

65. Zuo J, Hernandez YJ, Muir D. Chondroitin sulfate proteoglycan with neurite-inhibiting activity is up-regulated following peripheral nerve injury. *J Neurobiol.* 1998;34(1):41-54.

66. Hantaz-Ambroise D, Vigny M, Koenig J. Heparan sulfate proteoglycan and laminin mediate two different types of neurite outgrowth. *J Neurosci.* 1987;7(8):2293-2304.

67. Rosenmann H, Meiner Z, Kahana E, et al. An association study of a polymorphism in the heparan sulfate proteoglycan gene (perlecan, HSPG2) and Alzheimer's disease. *Am J Med Genet B Neuropsychiatr Genet.* 2004;128B(1):123-125.

68. Bloechlinger S, Karchewski LA, Woolf CJ. Dynamic changes in glypican-1 expression in dorsal root ganglion neurons after peripheral and central axonal injury. *Eur J Neurosci.* 2004;19(5):1119-1132.

69. Bignami A, Hosley M, Dahl D. Hyaluronic-Acid and Hyaluronic Acid-Binding Proteins in Brain Extracellular-Matrix. *Anat Embryol.* 1993;188(5):419-433.

70. Preston M, Gong X, Su WP, et al. Digestion products of the PH20 hyaluronidase inhibit remyelination. *Ann Neurol.* 2013;73(2):266-280.

71. Abood LG, Abul-Haj SK. Histochemistry and characterization of hyaluronic acid in axons of peripheral nerve. *J Neurochem.* 1956;1(2):119-125.

72. Ozgenel GY. Effects of hyaluronic acid on peripheral nerve scarring and regeneration in rats. *Microsurgery.* 2003;23(6):575-581.

73. Hamburger V. Cell death in the development of the lateral motor column of the chick embryo. *The Journal of comparative neurology.* 1975;160(4):535-546.

74. Hamburger V, Yip JW. Reduction of experimentally induced neuronal death in spinal ganglia of the chick embryo by nerve growth factor. *The Journal of neuroscience : the official journal of the Society for Neuroscience.* 1984;4(3):767-774.

75. Oppenheim RW. The neurotrophic theory and naturally occurring motoneuron death. *Trends Neurosci.* 1989;12(7):252-255.

76. Rind HB, Butowt R, von Bartheld CS. Synaptic targeting of retrogradely transported trophic factors in motoneurons: comparison of glial cell line-derived neurotrophic factor, brain-derived neurotrophic factor, and cardiotrophin-1 with tetanus toxin. *The Journal of neuroscience : the official journal of the Society for Neuroscience.* 2005;25(3):539-549.

77. Rind HB, von Bartheld CS. Anterograde axonal transport of internalized GDNF in sensory and motor neurons. *Neuroreport.* 2002;13(5):659-664.

78. Airaksinen MS, Titievsky A, Saarma M. GDNF family neurotrophic factor signaling: four masters, one servant? *Molecular and cellular neurosciences.* 1999;13(5):313-325.

79. Henderson CE, Yamamoto Y, Livet J, Arce V, Garces A, deLapeyriere O. Role of neurotrophic factors in motoneuron development. *Journal of physiology, Paris.* 1998;92(3-4):279-281.

80. Gould TW, Enomoto H. Neurotrophic modulation of motor neuron development. *The Neuroscientist : a review journal bringing neurobiology, neurology and psychiatry.* 2009;15(1):105-116.

81. Sun T, Dong H, Wu L, Kane M, Rowitch DH, Stiles CD. Cross-repressive interaction of the Olig2 and Nkx2.2 transcription factors in developing neural tube associated with formation of a specific physical complex. *The Journal of neuroscience : the official journal of the Society for Neuroscience.* 2003;23(29):9547-9556.

82. Zhou Q, Anderson DJ. The bHLH transcription factors OLIG2 and OLIG1 couple neuronal and glial subtype specification. *Cell.* 2002;109(1):61-73.

83. Qi Y, Cai J, Wu Y, et al. Control of oligodendrocyte differentiation by the Nkx2.2 homeodomain transcription factor. *Development.* 2001;128(14):2723-2733.

84. Zhou Q, Choi G, Anderson DJ. The bHLH transcription factor Olig2 promotes oligodendrocyte differentiation in collaboration with Nkx2.2. *Neuron.* 2001;31(5):791-807.

85. Sugimori M, Nagao M, Bertrand N, Parras CM, Guillemot F, Nakafuku M. Combinatorial actions of patterning and HLH transcription factors in the spatiotemporal control of neurogenesis and gliogenesis in the developing spinal cord. *Development.* 2007;134(8):1617-1629.

86. Li H, de Faria JP, Andrew P, Nitarska J, Richardson WD. Phosphorylation regulates OLIG2 cofactor choice and the motor neuron-oligodendrocyte fate switch. *Neuron.* 2011;69(5):918-929.

87. Chung AY, Kim S, Kim E, et al. Indian hedgehog B function is required for the specification of oligodendrocyte progenitor cells in the zebrafish CNS. *The Journal of neuroscience : the official journal of the Society for Neuroscience.* 2013;33(4):1728-1733.

88. Touahri Y, Escalas N, Benazeraf B, Cochard P, Danesin C, Soula C. Sulfatase 1 promotes the motor neuron-to-oligodendrocyte fate switch by activating Shh signaling in Olig2 progenitors of the embryonic ventral spinal cord. *The Journal of neuroscience : the official journal of the Society for Neuroscience.* 2012;32(50):18018-18034.

89. Snyder JL, Kearns CA, Appel B. Fbxw7 regulates Notch to control specification of neural precursors for oligodendrocyte fate. *Neural development.* 2012;7:15.

90. Rabadan MA, Cayuso J, Le Dreau G, et al. Jagged2 controls the generation of motor neuron and oligodendrocyte progenitors in the ventral spinal cord. *Cell death and differentiation.* 2012;19(2):209-219.

91. Louvi A, Artavanis-Tsakonas S. Notch signalling in vertebrate neural development. *Nature reviews. Neuroscience.* 2006;7(2):93-102.

92. Gokoffski KK, Wu HH, Beites CL, et al. Activin and GDF11 collaborate in feedback control of neuroepithelial stem cell proliferation and fate. *Development.* 2011;138(19):4131-4142.

93. Sugimori M, Nagao M, Parras CM, et al. Ascl1 is required for oligodendrocyte development in the spinal cord. *Development.* 2008;135(7):1271-1281.

94. Swetenburg R, White, DE, Kemp, ML, McDevitt, TC, Stice, SS. In preparation. 2015.

95. Dias JM, Alekseenko Z, Applequist JM, Ericson J. Tgfbeta signaling regulates temporal neurogenesis and potency of neural stem cells in the CNS. *Neuron.* 2014;84(5):927-939.

96. Wichterle H, Lieberam I, Porter JA, Jessell TM. Directed differentiation of embryonic stem cells into motor neurons. *Cell.* 2002;110(3):385-397.

97. Miles GB, Yohn DC, Wichterle H, Jessell TM, Rafuse VF, Brownstone RM. Functional properties of motoneurons derived from mouse embryonic stem cells. *The Journal of neuroscience : the official journal of the Society for Neuroscience.* 2004;24(36):7848-7858.

98. Li XJ, Du ZW, Zarnowska ED, et al. Specification of motoneurons from human embryonic stem cells. *Nature biotechnology.* 2005;23(2):215-221.

99. Shin S, Dalton S, Stice SL. Human motor neuron differentiation from human embryonic stem cells. *Stem Cells Dev.* 2005;14(3):266-269.

100. Li XJ, Hu BY, Jones SA, et al. Directed differentiation of ventral spinal progenitors and motor neurons from human embryonic stem cells by small molecules. *Stem cells (Dayton, Ohio).* 2008;26(4):886-893.

101. Hu BY, Zhang SC. Differentiation of spinal motor neurons from pluripotent human stem cells. *Nature protocols.* 2009;4(9):1295-1304.

102. Chambers SM, Fasano CA, Papapetrou EP, Tomishima M, Sadelain M, Studer L. Highly efficient neural conversion of human ES and iPS cells by dual inhibition of SMAD signaling. *Nature biotechnology.* 2009;27(3):275-280.

103. Takahashi K, Yamanaka S. Induction of pluripotent stem cells from mouse embryonic and adult fibroblast cultures by defined factors. *Cell.* 2006;126(4):663-676.

104. Toma JS, Shettar BC, Chipman PH, et al. Motoneurons derived from induced pluripotent stem cells develop mature phenotypes typical of endogenous spinal motoneurons. *The Journal of neuroscience : the official journal of the Society for Neuroscience.* 2015;35(3):1291-1306.

105. Boyden ES, Zhang F, Bamberg E, Nagel G, Deisseroth K. Millisecond-timescale, genetically targeted optical control of neural activity. *Nature neuroscience.* 2005;8(9):1263-1268.

106. Bryson JB, Machado CB, Crossley M, et al. Optical control of muscle function by transplantation of stem cell-derived motor neurons in mice. *Science (New York, N.Y.).* 2014;344(6179):94-97.

107. Mazzoni EO, Mahony S, Closser M, et al. Synergistic binding of transcription factors to cell-specific enhancers programs motor neuron identity. *Nature neuroscience.* 2013;16(9):1219-1227.

108. Son EY, Ichida JK, Wainger BJ, et al. Conversion of mouse and human fibroblasts into functional spinal motor neurons. *Cell stem cell.* 2011;9(3):205-218.

109. Patani R, Hollins AJ, Wishart TM, et al. Retinoid-independent motor neurogenesis from human embryonic stem cells reveals a medial columnar ground state. *Nature communications.* 2011;2:214.

110. Amoroso MW, Croft GF, Williams DJ, et al. Accelerated high-yield generation of limb-innervating motor neurons from human stem cells. *The Journal of neuroscience : the official journal of the Society for Neuroscience.* 2013;33(2):574-586.

111. Peljto M, Dasen JS, Mazzoni EO, Jessell TM, Wichterle H. Functional diversity of ESC-derived motor neuron subtypes revealed through intraspinal transplantation. *Cell stem cell.* 2010;7(3):355-366.

112. Adams KL, Rousso DL, Umbach JA, Novitch BG. Foxp1-mediated programming of limb-innervating motor neurons from mouse and human embryonic stem cells. *Nature communications.* 2015;6:6778.

113. Machado CB, Kanning KC, Kreis P, et al. Reconstruction of phrenic neuron identity in embryonic stem cell-derived motor neurons. *Development.* 2014;141(4):784-794.

114. Nedelec S, Peljto M, Shi P, Amoroso MW, Kam LC, Wichterle H. Concentration-dependent requirement for local protein synthesis in motor neuron subtype-specific response to axon guidance cues. *The Journal of neuroscience : the official journal of the Society for Neuroscience.* 2012;32(4):1496-1506.

115. Yang YM, Gupta SK, Kim KJ, et al. A small molecule screen in stem-cell-derived motor neurons identifies a kinase inhibitor as a candidate therapeutic for ALS. *Cell stem cell.* 2013;12(6):713-726.

116. Vyas N, Walvekar A, Tate D, et al. Vertebrate Hedgehog is secreted on two types of extracellular vesicles with different signaling properties. *Sci Rep.* 2014;4:7357.

117. Davis-Dusenbery BN, Williams LA, Klim JR, Eggan K. How to make spinal motor neurons. *Development.* 2014;141(3):491-501.

118. https://clinicaltrials.gov/ct2/show/NCT01217008.

119. Liu S, Qu Y, Stewart TJ, et al. Embryonic stem cells differentiate into oligodendrocytes and myelinate in culture and after spinal cord transplantation. *Proceedings of the National Academy of Sciences of the United States of America.* 2000;97(11):6126-6131.

120. Keirstead HS, Nistor G, Bernal G, et al. Human embryonic stem cell-derived oligodendrocyte progenitor cell transplants remyelinate and restore locomotion after spinal cord injury. *The Journal of neuroscience : the official journal of the Society for Neuroscience.* 2005;25(19):4694-4705.

121. Kumagai G, Okada Y, Yamane J, et al. Roles of ES cell-derived gliogenic neural stem/progenitor cells in functional recovery after spinal cord injury. *PloS one.* 2009;4(11):e7706.

122. Hooshmand MJ, Sontag CJ, Uchida N, Tamaki S, Anderson AJ, Cummings BJ. Analysis of host-mediated repair mechanisms after human CNS-stem cell transplantation for spinal cord injury: correlation of engraftment with recovery. *PloS one.* 2009;4(6):e5871.

123. Erceg S, Ronaghi M, Oria M, et al. Transplanted oligodendrocytes and motoneuron progenitors generated from human embryonic stem cells promote locomotor recovery after spinal cord transection. *Stem cells (Dayton, Ohio).* 2010;28(9):1541-1549.

124. Hu BY, Du ZW, Li XJ, Ayala M, Zhang SC. Human oligodendrocytes from embryonic stem cells: conserved SHH signaling networks and divergent FGF effects. *Development.* 2009;136(9):1443-1452.

125. Hu Z, Li T, Zhang X, Chen Y. Hepatocyte growth factor enhances the generation of high-purity oligodendrocytes from human embryonic stem cells. *Differentiation; research in biological diversity.* 2009;78(2-3):177-184.

126. Jiang P, Selvaraj V, Deng W. Differentiation of embryonic stem cells into oligodendrocyte precursors. *Journal of visualized experiments : JoVE.* 2010(39).

127. Chen C, Daugherty D, Jiang P, Deng W. Oligodendrocyte progenitor cells derived from mouse embryonic stem cells give rise to type-1 and type-2 astrocytes in vitro. *Neuroscience letters.* 2012;523(2):180-185.

128. Tao F, Li Q, Liu S, et al. Role of neuregulin-1/ErbB signaling in stem cell therapy for spinal cord injury-induced chronic neuropathic pain. *Stem cells (Dayton, Ohio).* 2013;31(1):83-91.

129. Yang N, Zuchero JB, Ahlenius H, et al. Generation of oligodendroglial cells by direct lineage conversion. *Nature biotechnology.* 2013;31(5):434-439.

130. Alsanie WF, Niclis JC, Petratos S. Human embryonic stem cell-derived oligodendrocytes: protocols and perspectives. *Stem Cells Dev.* 2013;22(18):2459-2476.

Figure 2.1. A gradient of Sonic Hedgehog drives progenitor domain formation in the ventral neural tube. A. Shh signaling from the notochord drives Class I transcription factors and represses Class II transcription factors at threshold levels. These transcription factors cross-repress to form sharply delineated boundaries. The class I Nkx2.2 represses the class II Pax6, while the Class I Nx6.1 represses Dbx2. B. This cross-repression leads to 5 distinct domains: FP, p3, pMN, p2, p1, and p0. Sonic Hedgehog (Shh); notochord (NC); floor plate (FP); progenitor (p); motor neuron progenitor (pMN)

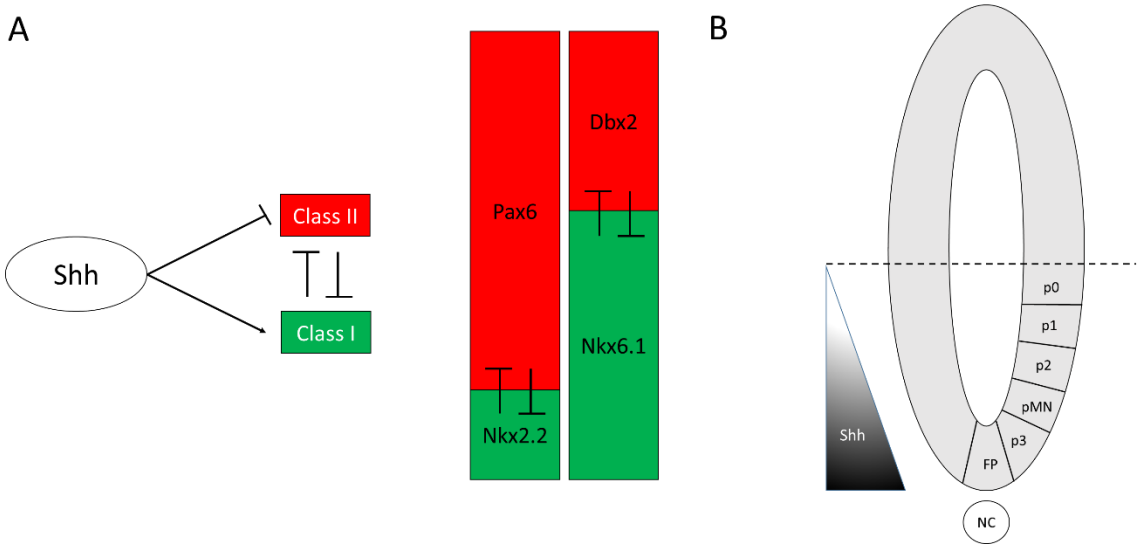
A
Shh
Class II
Class I
Pax6
Nkx2.2
Dbx2
Nkx6.1
B
Shh
p0
p1
p2
pMN
p3
FP
NC

Figure 2.2. Shh-driven transcriptional progression of initial motor neuron specification. Shh drives transcription of Pax6 and Nkx6.1, which drive Olig2, identifying mitotic progenitor cells. Ngn2 is expressed and causes cells to exit the cell cycle. Lhx3 and Isl1 activate Hb9 transcription which identifies a committed motor neuron. Sonic hedgehog (Shh)

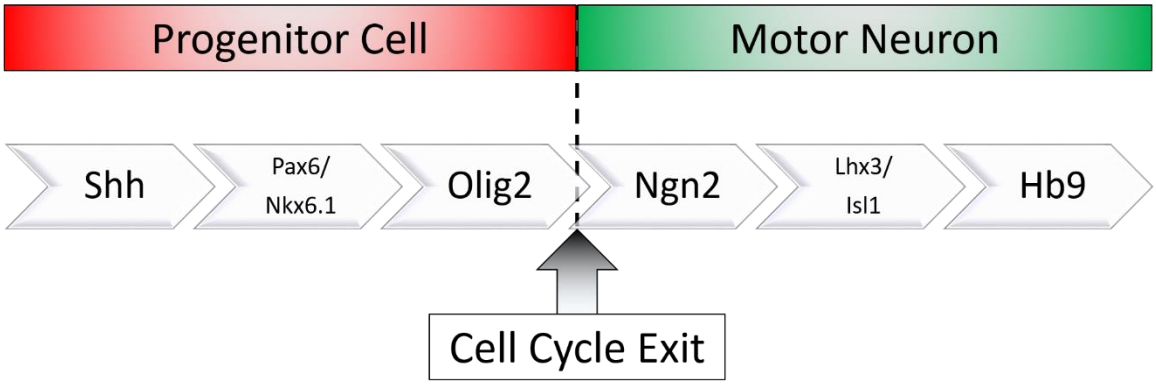
Progenitor Cell
Motor Neuron
Shh
Pax6/
Nkx6.1
Olig2
Ngn2
Lhx3/
Isl1
Hb9
Cell Cycle Exit

Figure 2.3. Hox gene expression throughout the developing spinal cord. Rostrocaudal identity is conferred through Hox genes expression throughout the neural tube. The repressive and combinatory actions of the factors play a crucial role in generating the wide diversity of motor neurons.

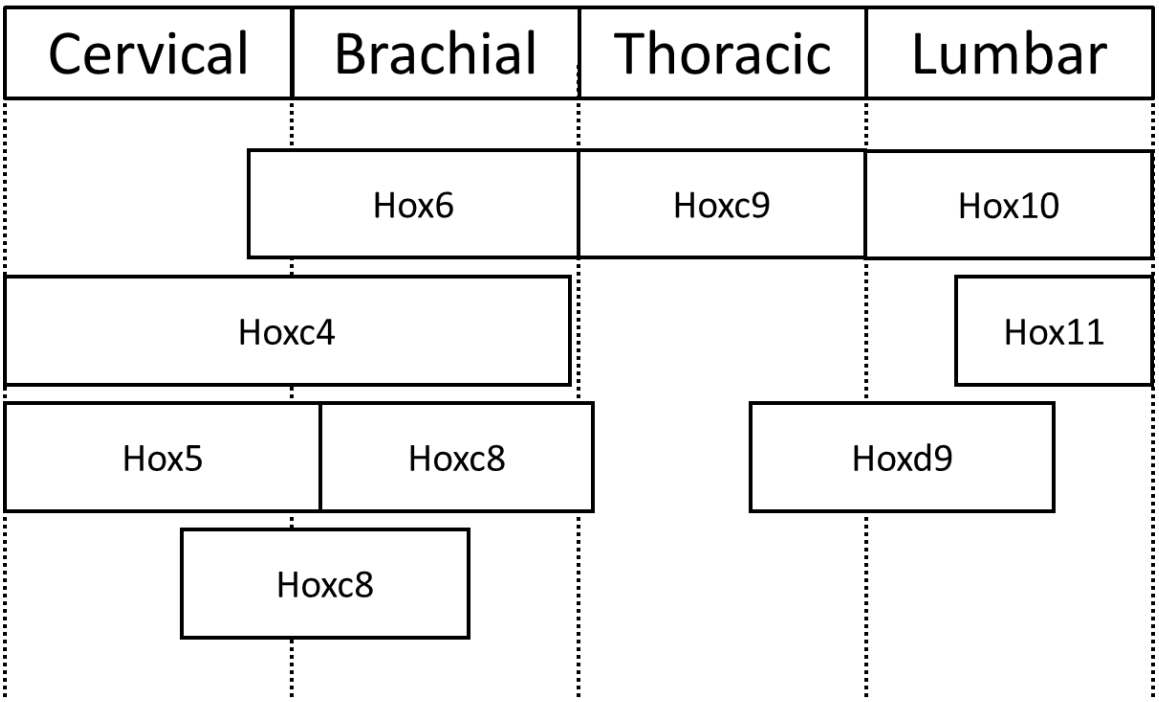
Cervical
Brachial
Thoracic
Lumbar
Hox6
Hoxc9
Hox10
Hoxc4
Hox11
Hox5
Hoxc8
Hoxd9
Hoxc8

CHAPTER 3

ELUCIDATING MOTOR NEURON AND OLIGODENDROCYTE DIFFERENTIATION PATHWAYS VIA COMPUTATIONAL ANALYSIS OF SUBPOPULATION DYNAMICS IN THREE DIMENSIONAL MURINE EMBRYONIC STEM CELL CULTURE [1]

[1]Swetenburg, R.L., White, D.E., Kemp, M.L., McDevitt, T.C. and S.L. Stice. Submitted to *Nature Communications*, 1/18/17.

Abstract

Three dimensional *in vitro* stem cell differentiation is an inherently heterogeneous and complex process which currently lacks an adequate framework to test mechanistic hypotheses. Spatial pattern analysis provides a portable computational method to quantify, model and explain the interactions between diverse cell types at both the phenotypic and molecular level. Here, we describe motor neuron progenitor cells as they self-renew and differentiate towards motor neurons or oligodendrocyte precursor cells. Using network-derived metrics as high-level features for comparing complex multicellular properties, such as spatial relationships between different phenotypes, allows for the unique ability to compare computational simulations directly to three dimensional microscopy imaging data. Through this iterative computational/experimental approach and validation process, we describe potential mechanisms governing both the cellular source of the glial switch and the multifaceted role of Notch-Delta. A three dimensional, agent-based computational model of progenitor cell fate decisions supports a novel intermediate cell state between progenitors and motor neurons, and underlying mechanisms governing both the glial switch signal and Notch-Delta signaling.

Introduction

Stem and progenitor cell fate decisions, including self-renewal and differentiation, are critical to achieving appropriate cellular heterogeneity and stoichiometry, regulating organ size and maintaining homeostasis throughout development and in the adult [1]. Typical *in vitro* and *in vivo* studies investigate a single or limited set of mechanistic hypotheses in order to explain fate decisions and phenotype acquisition. However, cellular phenotype is a complex and fluid emergent property resulting from the

integration of multiple extracellular cues and the complete intracellular state. Standard approaches, therefore, are often constrained and may lack the proper context in which a given process may occur. Computational modeling allows us to reverse engineer the process of differentiation: we can begin with an observed phenotypic progression and efficiently test mechanistic hypotheses *in silico*, leading to a better understanding of both *in vitro* and *in vivo* events. In this manner, we can facilitate the concurrent integration and interrogation of diverse but interdependent hypotheses. Moreover, *in vitro* cell culture conditions are inherently disrupted from *in vivo* settings: cells will encounter unique environmental cues and cell-cell interactions potentially revealing novel mechanistic phenomena. To facilitate this process, we previously developed an agent-based model for investigating dynamic features of *in vitro* pluripotency, capable of both recapitulating and predicting early loss-of-pluripotency differentiation events [2]. Furthermore, we have demonstrated the utility of a multicellular pattern analysis pipeline to reveal novel interactions between distinct but related cellular phenotypes in diverse systems including pluripotent stem cell (PSC) aggregates and gastrulating fish embryos [3].

In the developing embryo, one of the best described fate decision processes occurs in the ventral neural tube, where a soluble Sonic Hedgehog (Shh) gradient emanating from the notochord and, later, the floor plate, generates distinct progenitor domains that produce most of the neuronal and glial cell types of the adult motor control system [4]. Each progenitor domain undergoes mitosis to maintain its own population while also generating two or more cell types in a precise temporal manner [5]. Specifically, the motor neuron progenitor domain (pMN) initially generates motor

neurons (MN). Later, the pMN domain generates oligodendrocyte precursor cells (OPC). Although initial Shh-dependent patterning events are well described, the diversification of the pMN domain including the glial switch from MN to OPC remains poorly understood.

Division and differentiation of pMN fall largely under the genetic control of the basic helix-loop-helix protein oligodendrocyte transcription factor 2 (Olig2) [6-9], which is necessary for the generation of both MN and OPC [9]. Initially, Olig2 drives the transcription of pro-neurogenic genes while preventing cell cycle exit (anti-neurogenic), partially by repressing the essential MN identity gene homeobox 9 transcription factor (Hb9) [10, 11]. After a pool of Olig2-expressing progenitors arises, MN are generated through asymmetric divisions [12] yielding one progenitor and one MN. Later in development, pMN co-express Olig2 and NK2 homeobox transcription factor 2 (Nkx2.2), demarcating early OPCs [8]. Interestingly, Olig2 and Nkx2.2 act as cross-repressors during progenitor domain specification delineating distinct cell types, yet are co-expressed and cooperate to promote the OPC genetic program, including myelination [13]. Though some intracellular events have been identified, external cues governing the switch from cross-repression to co-expression, and also from neuronal to glial cell fates of downstream progeny, remains largely unknown.

In addition to Olig2, Notch-Delta signaling is essential for appropriate pMN fate decisions, but *in vivo* studies have linked its effect to temporally-dependent phenotypes. In the murine neural tube, activated Notch-Delta is required for progenitor self-renewal and maintenance of the pMN pool through mitosis [14, 15]. In contrast, Notch inhibition potentiates cells to Shh signaling in early development, increasing pMN pools in a cell

cycle-independent manner [16]. Upon the formation of a pMN pool, Notch1 knockout causes precocious neuronal differentiation in the mouse neural tube at the expense of progenitors [17] consistent with *in vitro* reports [14]. Notably, knockdown of the Notch ligand Jagged2 in the chick neural tube generates precocious OPC production [18]. These findings imply that there is a temporal, permissive aspect to Notch-Delta signaling dependent on the pMN genetic state and/or external signaling factors, while also raising the possibility that Notch-Delta may be acting in conjunction with more than one pathway over the course of development. Resolving these conflicting phenotypes - increased versus decreased progenitor pools; enhanced neurogenesis versus enhanced gliogenesis - is therefore essential to properly elucidate the roles of Notch-Delta and the underlying mechanisms defining pMN fate decisions.

In this study, we examined *in vitro* pMN fate decisions employing a combined computational and experimental approach. Through iterative, stochastic modeling, we elucidated novel cell states and signaling mechanisms governing differentiation in order to build a multicellular computational modeling platform for further interrogation of pMN self-renewal and differentiation. For the first time, we link the genetic state of progenitors, the glial switch, and morphogen signaling (Notch-Delta and Sonic Hedgehog) together to elucidate the complex interconnections between these cues and how their combined effects regulate fate decisions.

Results

To generate aggregates and desired cell types, HBG3 mouse embryonic stem cells (mESC) [19] were aggregated in rotary suspension culture for 48 hours in the absence of leukemia inhibitory factor (LIF)[20]. Cultures were supplemented with the Shh-mimic

purmorphamine [21] and retinoic acid from day 2 and with each subsequent media change (Fig. 3.1a). The neuronal survival factors brain-derived neurotrophic factor and glial cell line-derived neuronal factor were added on day 6 (Fig. 3.1a). Intact aggregates were fixed every 24 hours from day 3; immunolabeled for Olig2 (Fig. 3.1b), GFP (Fig. 3.1c) and Nkx2.2 (Fig. 3.1d); and imaged in three dimensions using confocal microscopy (Fig. 3.1e). Cell types were identified as pMN ($Olig2^{+}/Nkx2.2^{-}$), MN (GFP^{+}) and OPC ($Olig2^{+}/Nkx2.2^{+}$) (Fig. 3.1f) and converted to graph networks for analysis (see Methods).

From the converted network images, we generated a dataset of spatial attributes for each aggregate (Fig. 3.2). Unsupervised principal component analysis (PCA) of our data indicated clear differentiation trajectories for aggregates (Fig. 3.2a) through the latent space, similar to morphogenic trajectories observed with prior systems using network-derived metrics [2, 3]. Differentiation from day 3 through 7 progressed with increasing loading weights on principal component (PC) 1 and negatively on PC2. Interestingly, days 5-7 appear to generally cluster together, representing covariance of network-extracted features, even though aggregates appear to undergo rapid changes in subpopulations during this time period (Fig. 3.3). Observations from Day 8 are shifted up in PC1, while the variance of this time point in latent space is greater than earlier observations. Observations from Day 9, in contrast, yield larger weights contributing to PC2. PC1, accounting for 23.82% of the variance, was positively correlated to progenitor metrics, as well as MN and pMN cluster-cluster distances (Fig. 3.2b) and can be loosely interpreted as a "progenitor axis". PC1 was weakly influenced by measurements of local cell-cell connectivity (termed the 1^{st} and 2^{nd} degree associative metrics) (Fig. 3.2b). PC2, accounting for 15.18% of variance, negatively correlated to progenitor metrics, but was

strongly influenced by OPC metrics and OPC-related 1st and 2nd degree associative metrics (Fig. 3.2b). Interestingly, MN metrics had little influence on PC1 or 2, weakly influenced PC3, and became more prevalent in negatively influencing PC4 and 5 (Fig. 3.2b).

To interpret the data from our network analysis, we next explored possible differentiation schemes via stochastic modeling. Our experimental results reflected three trends with regards to cell type quantity: (1) MN and pMN arise concurrently, followed by the appearance of OPC; (2) MN increase rapidly and plateau at later time points as OPC are generated; (3) pMN expand slowly but exhibit a rapid rate of expansion in late differentiation (Fig. 3.3). Based on these results we generated four stochastic models to computationally describe our experimental data. The first model explored was a "random" scheme (Fig. 3.3a), in which each cell type arises with unique, but temporally consistent, probabilities. Compared to experimental data, this mechanism prematurely generated both pMN (Fig. 3.3b) and OPC (Fig. 3.3d), but failed to account for the late differentiation plateau seen in MN (Fig. 3.3c). To address both the MN plateau and late onset of OPC production, we implemented a hypothetical negative feedback mechanism (Fig. 3.3e), wherein OPC generation depended on the number of MN present (see Methods). When MN reached a critical mass, they self-limit their production causing a permissive, neuronal-to-glial switch in progenitors. With this model, we qualitatively demonstrated that the model could capture both experimental trajectories for MN (Fig. 3.3g) and OPC (Fig. 3.3h). However, simulated progenitors were still generated prematurely to observed experimental results and failed to capture the rapid expansion of the late experimental data (Fig. 3.3f). In order to capture the dynamics of the pMN curve,

we introduced a transient progenitor state to the model. This state was defined as a non-mitotic MN progenitor cell type that lacked identifiable Olig2 expression and thus exists within the unlabeled cell population (Supplementary Fig. 3.1). This model appropriately recapitulated pMN cell generation without disrupting the previously validated MN (Fig. 3.3k) and OPC (Fig. 3.3l) curves. Collectively, the model structure implied two novel mechanisms in the fate decisions of progenitor cells: a negative feedback mechanism self-limiting MN generation and a transient, non-mitotic progenitor state.

The HBG3 cell line expresses enhanced green fluorescent protein (GFP) behind the promoter sequence for the motor neuron-specific transcription factor Hb9 [19]. To address negative feedback as a source for the glial switch (Fig. 3.3i), we performed fluorescence-activated cell sorting (FACS) and collected conditioned media from MN-enriched (GFP^+) and MN-depleted (GFP^-) cell fractions, as well as from immature cultures (prior to RA or Pur addition). Dissociated day 5 aggregates were cultured in conditioned media for each condition. All cultures generated both MN and OPC in test cultures (Fig. 3.4a-c). However, conditioned media from MN-enriched (Fig. 3.4a) and MN-depleted (Fig. 3.4b) mature cultures increased the ratio of OPC to MN 6.0 and 7.4 fold, respectively, over media from immature cultures (Fig. 3.4c, d). Taken together, our data suggest a temporally-dependent, soluble factor from MN-enriched or –depleted mature, but not immature, cultures significantly increased OPC production. These results are consistent with a mechanism suggested by the feedback/transient model, in which a late arising population, including MN, regulates the OPC population through feedback (Fig. 3.3i).

Although Notch-Delta commonly impacts progenitor cell fate decisions, it often functions in a context-dependent manner [16, 18, 22], thus we next explored how temporal Notch inhibition might affect the system. Previous reports suggest that Notch-Delta inhibition can induce either neurogenesis (early) or gliogenesis (late) [14, 17, 18], as well as expand pMN pools [16]. To explore the role of Notch-Delta signaling in pMN fate decisions, cultures were treated starting at either day 3 or day 7 of differentiation with the γ-secretase inhibitor DAPT, which inhibits the Notch pathway [23]. Experimentally, we observed rapid MN differentiation followed by a steady decline (Fig. 3.5c), few pMN (Fig. 3.5b) and no OPC (Fig. 3.5d) after day 3 DAPT-treatment. In contrast, addition of DAPT starting at day 7 did not hinder the expansion of pMN (Fig. 3.5e) or the onset of OPC (Fig. 3.5g), and had little effect on MN (Fig. 3.5f). When compared to vehicle at 48 hours post-treatment, MN and OPC were significantly increased, after days 3 and 7 DAPT, respectively (Supplementary Fig. 3.2a, b), consistent with previous reports.

To rule out the direct involvement of Notch-Delta in the pMN-to-MN or pMN-to-OPC transition, we employed stochastic modeling to separately probe whether DAPT directly increased flux towards either MN (Supplementary Fig. 3.2c) or OPC (Supplementary Fig. 3.2j). When DAPT drove only MN differentiation, our model recapitulated early MN increases, but could not account for the decline in MN (Supplementary Fig. 3.2e), the low number of pMN (Supplementary Fig. 3.2d) or the lack of OPC (Supplementary Fig. 3.2f). Day 7 DAPT simulations recreated MN levels (Supplementary Fig. 3.2h), but could not account for expansion of progenitors (Supplementary Fig. 3.2g) or increased OPC (Supplementary Fig. 3.2i). When DAPT

directly increased OPCs (Supplementary Fig. 3.2j), day 3 treatment failed to increase MN (Supplementary Fig. 3.2l) or deplete progenitors (Supplementary Fig. 3.2k), while prematurely increasing OPC (Supplementary Fig. 3.2m). Day 7 DAPT simulations captured OPC increases (Supplementary Fig. 3.2p), but not pMN expansion (Supplementary Fig. 3.2n), while depressing MN quantity (Supplementary Fig. 3.2o). Based on an inability to accurately simulate the experimental outcomes, it is likely that DAPT or its targets, including Notch-Delta, contributed to MN and OPC differentiation by an indirect mechanism, possibly through Olig2.

To explore potential indirect mechanisms of MN expansion over vehicle (Supplementary Fig. 3.2b), we hypothesized that activated Notch stabilizes Olig2, therefore the inhibition of Notch signaling would destabilize Olig2 generating an increase in transient progenitors and thus MN. Further, this destabilization would increase MN at the expense of pMN and OPC (Fig. 3.5 a-g). To explain additional increases in downstream cell types, we took into account that Notch-Delta inhibition expands pMN progenitors in early neural tube development by augmenting Shh signaling in a cell cycle-independent manner [16]. Thus, we further hypothesized that this mechanism persists throughout the differentiation process, yielding increased pMN and OPC, both of which are at least partially contingent on Shh signaling pathways (Fig. 3.5 a, h, l). By applying these two independent hypotheses, our computational data recreated our Day 3 DAPT-treated experimental data: stable pMN remained low (Fig. 3.5b), MN increased then declined (Fig. 3.5c), and no OPC were generated (Fig. 3.5d). However, simulations of Day 7 DAPT-treated conditions failed to match pMN (Fig. 3.5e) or OPC (Fig. 3.5g), but could fit MN (Fig. 3.5f). Hence, the computational simulations based on the

schematic in Figure 5a matched day 3 DAPT treatment but failed to account for day 7 DAPT treatments.

To investigate mechanisms responsible for the cell quantities in day 7 DAPT-treated conditions, we hypothesized that, while DAPT was sufficient for Olig2 destabilization at day 3 (Fig. 3.5h), Olig2 was stabilized by a non-DAPT target at day 7 (Fig. 3.5l). In other words, at day 3 of differentiation, DAPT increased flux from pMN to transient progenitor (Fig. 3.5h). But by day 7, though DAPT retains its ability to augment Shh signaling, Notch is no longer required for Olig2 stabilization. Thus, the DAPT-mediated pMN-to-transient progenitor transition is effectively eliminated (Fig. 3.5l). Here, we accurately recapitulated the stochasticity of Day 3 DAPT treatment effects on pMN (Fig. 3.5i), MN (Fig. 3.5j) and OPC (Fig. 3.5k). In late-stage differentiation, this new model appropriately fit the dynamics of pMN (Fig. 3.5m), MN (Fig. 3.5n) and the spike in OPC (Fig. 3.5o). From these simulations, we propose that, in the early stages of differentiation, the pMN state is pushed towards a transient $Olig2^-$ state in the absence of Notch-Delta signaling, resulting in an increase in MN at the expense of pMN and OPC. In later stages of differentiation, the pMN-to-transient progenitor transition is blocked, thereby generating increases in pMN and OPC.

In the murine neural tube at the time of OPC specification, Tgf-β family members are expressed by pMN and in the motor columns [24]. Moreover, Tgf-β signaling has been implicated in regulating the potency of MN-and OPC-generating progenitors [25]. Nkx2.2 has been shown to directly interact with and restrict Olig2 protein to the nucleus [13]. Therefore, we investigated both Tgf-β signaling and Nkx2.2 expression as potential Olig2 stabilization agents (Fig. 3.6, Supp. Table 3.1). Aggregates were dissociated and

exposed to either Tgf-β2 or the Tgf-β inhibitor SB431542 (SB) [26] at day 5, when pMN quantities plateau at a low level yet MN are increasing (Fig. 3.3). Media was changed to DAPT- or DMSO-containing media followed by immunocytochemistry and analysis by flow cytometry (Fig. 3.6a). SB treatment generated more MN than Tgf-β2 treated cultures, consistent with a stabilized Olig2 hypothesis (*P*=0.037 between SB and Tgf-β2). Total $Olig2^+$ cells including pMN ($Olig2^+/Nkx2.2^-$) and OPC ($Olig2^+/Nkx2.2^+$) were increased in Tgf-β2 cultures (*P*=0.02 between SB and Tgf-β2), and DAPT significantly increased this population in Tgf-β2, but not SB, cultures (*P*=0.012 For DMSO/DAPT within Tgf-β2). pMN cell quantities largely followed the same pattern as total Olig2-expressing cells with Tgf-β2/DAPT being significantly increased over all other conditions (*P*=0.08 between SB and Tgf-β; *P*=0.027 for DMSO/DAPT with Tgf-β; *P*=0.006 for SB/Tgf-β within DAPT). Total Nkx2.2-expressing cells increased with DAPT over DMSO, but there was no difference between Tgf-β2 and SB (*P*=0.025 between DMSO and DAPT, *P*=0.842 between SB and Tgf-β2), indicating that DAPT increases Nkx2.2 expression in a Tgf-β-independent manner. Further confirming this, within Olig2-expressing cells there was no significant difference in the fraction of pMN and OPCs regardless of culture conditions. However, the Nkx2.2-expressing population showed an overall increase in the $Nkx2.2^+/Olig2^-$ fraction in Tgf-β over SB, but a decrease in OPC (*P*=0.006 for $Olig2^-$ within $Nkx2.2^+$; *P*=0.045 for $Olig2^+$ within $Nkx2.2^+$), concurrent with the ratio of total $Nkx2.2^+$ cells to total $Olig2^+$ cells. Taken together, the cell fraction data indicate that Olig2 is equally susceptible to the downstream effects from Notch-Delta inhibition or Tgf-β signaling independent of the availability of Nkx2.2. Nkx2.2, therefore, is insufficient to block the destabilizing effects

of DAPT on Olig2. Overall, these data support the hypothesis that DAPT increases Shh signaling and destabilizes Olig2 in the absence of Tgf-β2 signaling. Tgf-β, but not Nkx2.2, was able to block the destabilizing effect of DAPT, strongly supporting a role for Tgf-β signaling in the maintenance of Olig2 expression and prior to the specification of $Olig2^{+}/Nkx2.2^{+}$ OPC.

Given the pronounced perturbation of MN and OPC lineages that resulted from time-sensitive DAPT treatment (Supplementary Fig. 3.2a, Fig. 3.5), our knowledge of changes in patterning that result within NSC aggregates (Figs 1 & 2) and the inherent spatial contrast between juxtacrine Notch-Delta and a soluble negative feedback signal, we hypothesized that the spatial relationships between pMN, MN, and OPC as reflected by our network-based analysis would reflect DAPT disruption of the transient progenitor state. Using the previously validated stochastic modeling scheme (Fig. 3.5h) a 3D computational model was constructed to examine the evolution of spatial patterns associated with DAPT treatment. As self-renewing progenitors are known to be regulated by juxtacrine Notch signaling induced via proximity to Notch ligand expressing-cells [14, 15, 27], it was hypothesized that differences in progenitor cluster sizes and cell associations would be readily detected between aggregates treated or not treated with DAPT. The proposed mechanism for MN self-limiting feedback is an unknown secreted factor, likely Tgf-β, while the Notch-Delta mediated feedback on progenitors is established through local cell-cell interactions [27]. Thus the MN feedback mechanism was modeled as directly proportional to the number of MN, while local cell-cell interactions associated with pMN regulation were explicitly modeled as a function of cellular neighbors (see methods). Importantly, our proposed $Olig2^{-}$ transient progenitor

state was included as a population within the unlabeled cells (Supplementary Fig. 3.1). Because these simulations are computationally intensive, a pseudo-time axis was used and then normalized to match the experimental time scales. Representative images for untreated (Fig. 3.7a-c) and DAPT-treated aggregates (Fig. 3.7d-f) illustrate that, by day 10 of our simulation, DAPT-treated aggregates had a greater number of pMN with more overall OPC and pMN than vehicle-treated aggregates. The changes in cell number corresponded to those observed in the DAPT and vehicle experiments (Fig. 3.5m and n). In order to quantitatively describe these differences, spatial pattern analysis was used as described for Fig. 3.2 [2].

Using network-derived metrics as high-level features for comparing complex multicellular properties, such as spatial relationships between different phenotypes, allows for the unique ability to compare computational simulations directly to microscopy imaging data. Based on the hypothesized changes upon DAPT treatment, it was expected that such spatially observable changes would primarily affect the $Olig2^{+}$ progenitor pool. Therefore, a reduced model to investigate only the spatial localization of progenitors was considered based on the previous hypothesis (Fig. 3.7j). PCA of the agent-based simulated aggregates showed a predicted trajectory of network metric loading weights across latent space for the DAPT and untreated conditions which gradually separate from day 8 (Fig. 3.7g), day 9 (Fig. 3.7h) and day 10 (Fig. 3.7i). Simulated populations at day 8 contained little to no OPC cells; however PC1 (56.25% of the variance) was positively correlated with intra-cluster distance metrics as well as the relationship between glial and progenitor cells, suggesting that the PC1 axis primarily denoted interactions between progenitor clusters and glial cells. In contrast, PC2 (24.89%

of the variance) was strongly negatively influenced by the cluster count and positively influenced by the number of unclustered nodes making it a measure of overall progenitor clustering. The same PCA model was then applied to the experimental data from both untreated and DAPT-treated day 9 aggregates (Fig. 3.7k). Experimental DAPT treatment produced aggregates that matched the simulated evolution of multicellular spatial organization in DAPT treatment especially around day 9. Interestingly, data from untreated experimental aggregates yielded a mix of the simulated control population at day 8 and day 9. However, the aggregates in the same region on the PCA plot as the DAPT population were largely devoid of glial cells, while those in the upper left quadrant had an established glial population similar to simulated day 9, which matched the predicted model scheme. The spatial analysis of neural aggregates in conjunction with the computational modeling analysis suggested that Notch inhibition at later time points increased the number of progenitor clusters but decreased the number of progenitor cells within clusters, as well as increasing the number of unclustered pMN compared to control. Therefore, consistent with our proposed mechanism, DAPT-treated aggregates responded to augmented Shh signaling via Notch inhibition which generated smaller clusters and more unclustered pMN. Conversely, the pMN cell population in vehicle aggregates largely derived from pMN mitosis resulting in fewer clusters and fewer unclustered pMN. Furthermore, the model predicts that allowing differentiation to proceed over longer culture times would result in greater separation and resolution of Notch-inhibited and -uninhibited populations in PCA space (Fig. 3.7i). Altogether, the collective results demonstrate that manipulating Notch signaling modulated the

proportion of progenitor populations and subsequent differentiation to either neuronal or glial fates via a time-dependent mechanism.

Discussion

Multicellular, three dimensional *in vitro* differentiation, as seen in organoids, is inherently defined by complex interactions among heterogeneous cell types. Thus, the collection, characterization and analysis of 3D structures and subsequent comparisons to computational models poses challenges for traditional molecular biology approaches. Computational modeling is a powerful tool for concurrent, qualitative interrogation of mechanistic hypotheses including diverse, codependent pathways that arise in heterogeneous systems throughout their temporal evolution. Here, we present a spatial pattern analysis platform capable of overcoming traditional limitations based on experimental results and defined, biologically-relevant rules, including asymmetric and symmetric divisions as well as binary cell state transitions.

During normal *in vivo* development, Olig2-expressing pMN cells arise, then divide symmetrically to expand in number prior to generating MN [9]. *In vitro* MN differentiation has been assumed to function in a similar manner, but previous studies have failed to integrate data from early time points [19]. Here, we show that it was impossible for *in silico* simulations to recreate our data with an identifiable, obligate pMN cell state. Both scenarios in which mitotic, identifiable, Olig2-expressing cells were simulated - even upon immediate symmetric division to MN - failed to fit the experimentally observed early pMN lag and the late expansion. Therefore, we introduced a novel transient progenitor cell state into the computational models, whereby neural stem cells could bypass an identifiable Olig2-expressing cell type to generate neurons.

Only with the inclusion of an intermediate cell state did the models faithfully recapitulate the experimental cell quantities.

It is important to note that in our simulations, Olig2 expression remains required to MN formation, yet is undetectable by our network conversion method. In other words, these transient progenitors are "hidden" from conventional Olig2^{+} staining. One justification for the inclusion of a transient progenitor cell state is that the Olig2 protein is translated, then actively exported from the nucleus, as has been reported [13, 28]. Our cell type identification algorithm initially masked images corresponding to the nuclear dye Hoechst (see Methods), meaning only proteins labeled within the nucleus were quantified and labeled proteins in the cytoplasm would have been excluded. Additionally, nuclear export of Olig2 would abrogate its function as a repressor of proneural genes including Ngn2 and Hb9 [6], allowing for rapid neuronal differentiation. Moreover, Notch inhibition with DAPT can induce Olig2 translocation to the cytoplasm in the adult murine brain [29]. Further strengthening our argument for a transient, non-functional Olig2^{+} state, Olig2 is neither necessary nor sufficient for the direct reprogramming of fibroblasts, or differentiation of mESCs, to a MN fate [30, 31].

Notch signaling is required for progenitor pool expansion and cell division [32]. Therefore, we posited that Notch or a Notch target serves as a nuclear anchor for Olig2, and thus its inhibition would destabilize Olig2, shifting mitotic progenitor cells towards a transient progenitor state. In addition, neural stem and progenitor cells can divide asymmetrically depending upon the level of Notch activity in each daughter cell. Notch^{high} daughter cells retain their progenitor identity, while Notch^{low} cells progress rapidly towards a neuronal fate [12, 33, 34]. In further refining our differentiation

schemes, we accounted for recent studies where Notch inhibition expanded *in vivo* pMN pools by potentiating cells to augmented Shh signaling in a mitosis-independent manner in early differentiation [16]. Our data suggest this mechanism persists throughout differentiation. Therefore, in our model, Notch inhibition contrastingly increases Shh signaling, leading to an increase in Olig2 transcription, while destabilizing Olig2 function. Notably, augmented Shh signaling is critical to OPC differentiation [35-41], as Nkx2.2 is a target of Shh [42]. Thus, we constructed our model accordingly: Notch inhibition via DAPT enhanced the transition of NSC to pMN and transient progenitors, but drastically increased the flux of mitotic to transient progenitors; Notch inhibition also increased the transition from pMN to OPC, though the effect was imperceptible in early (day 3) DAPT treatments due to a lack of stable progenitors. The resulting model successfully recreated the early DAPT results and is consistent with both with *in vivo* [14] and *in vitro* [17] reports of enhanced neurogenesis in response to Notch inhibition.

While this strategy could explain early DAPT treatment, this model could not account for the increase in pMN and OPC seen in late (day 7) DAPT treatment. Despite the indispensable role of Olig2 in our system, the presence of identifiable Olig2 is a fundamental difference between MN and OPC, as well as transient and mitotic progenitors. In early DAPT treatment, the system shifts to cell types lacking nuclear Olig2 expression due to the proposed Notch-dependent Olig2 stabilization. In late DAPT treatment, the system shifts to cell types positive for nuclear Olig2 expression. To reconcile these divergent effects, we introduced a Boolean Olig2 “anchor” term to our stochastic model. Essentially, the anchor term is a required Olig2 stabilization signal to preserve its function. Olig2 was thus “anchored” by a DAPT target in early

differentiation (day 3-7). Early DAPT treatment removed the anchor resulting in the destabilization of Olig2, and a corresponding increase in Olig2$^-$ transient progenitors and MN. In days 7-9, we hypothesized that Notch was replaced as the Olig2 anchor, but that DAPT retained its ability to increase Shh signaling, resulting in the observed OPC and pMN increases after day 7 DAPT treatment.

bHLH transcription factors like Olig2 proteins can perform multiple functions that change over time due, in large part, to their ability to dimerize with interchangeable binding partners, or cofactors [43]. The pairing with cofactor(s) is determined by cofactor availability and/or the post-translational state of the bHLH protein (e.g. phosphorylation). We hypothesize that cofactor selection is a likely mechanism for Olig2 stabilization, as defined in the model by the anchor term. Moreover, the negative feedback signal described here is a likely candidate as the effector of this new Olig2 anchor which replaces the Notch target. Although MN pools began to plateau by day 7, neither pMN nor OPC have begun to accumulate to prime the progenitor cells for the large transitions seen at days 8 and 9. Furthermore, the weights from our individual observations shift along the "progenitor" PC1 axis from days 3 through 6, then appear to regress on day 7, before the large changes in progenitor state and OPC features (PC2) appear on day 8 and 9 (Fig. 3.2). We hypothesize that network characteristics reflect the timing that this Notch anchor is likely replaced. A soluble external signaling protein, like that present in conditioned media (Fig. 3.4), could trigger various pathways including kinase/phosphatase cascades or new cofactor translation resulting in the preferential binding of Olig2 over a Notch-mediated mechanism.

To investigate potential Olig2 stabilization signals, we activated or inhibited Tgf-β signaling in differentiating cultures (Fig. 3.6). Tgf-β-stabilized Olig2 expectedly yielded decreased MN and increased the total number of Olig2-expressing cells. The Olig2 population was further increased by DAPT in Tgf-β cultures, which we attribute to Shh signaling in the presence of a Tgf-β-dependent Olig2 stabilization mechanism. The Nkx2.2-expressing cell population was independent of Tgf-β signaling, but significantly increased under DAPT conditions, although Nkx2.2 does not require stabilization as we propose for Olig2. Olig2 is transiently expressed and selectively downregulated in what will ultimately become the Nkx2.2+ progenitor domain of the neural tube [44], meaning we would expect a decrease in $Olig2^{+}$ cells concomitant with an increase in Nkx2.2 cells, particularly in SB-treated cultures. However, even when comparing DMSO and DAPT in the most (Tgf-β) and least (SB) favorable conditions for Olig2 expression, no reciprocal increase or decrease was observed in Nkx2.2-expressing cells. While we cannot rule out the Olig2-to-Nkx2.2 progenitor conversion in early differentiation, the MN generated would need to be derived from a reduced population of progenitors than hypothesized, further reinforcing our transient progenitor hypothesis if understating its importance.

The transition from Olig2-Nkx2.2 co-repression to co-expression is required for the pMN progeny fate switch from MN to OPC [8, 13, 45, 46]. Nkx2.2 directly interacts with Olig2, and has been implicated as a binding partner capable of restricting Olig2 localization to the nucleus [13]. However, our data demonstrate that Nkx2.2 expression does not directly influence Olig2 expression, nor does it act as a stabilizing agent. In figure 3.6, the $Nkx2.2^{+}$ and $Nkx2.2^{-}$ cell fractions within the Olig2-expressing population

shows no change across treatments. Were Nkx2.2 a true "anchor" for Olig2, as described in the final model, we would expect pMN and OPC to be differentially regulated within the $Olig2^{+}$ population in response to treatments. OPC as a share of Nkx2.2-expressing cells decreased in Tgf-β inhibited cultures, indicating that the presence of Nkx2.2 is insufficient to block the effects of DAPT in the same manner as Tgf-β. However, Olig2 co-expression with Nkx2.2 remains a required step in OPC specification [46]. Therefore, a novel, intermediate cell state likely exists subsequent to $Olig2^{+}/Notch^{high}$ pMN cells but preceding $Olig2^{+}/Nkx2.2^{+}$ OPC that is at least partially reliant on Tgf-β signaling for Olig2 stabilization. The attenuation of Notch-Delta signaling, as seen *in vivo* during the post-neurogenesis pMN stage [18], could then increase Nkx2.2 expression.

Lastly, we built an agent-based model that incorporated a diversity of mechanisms governing progenitor cell fate decisions, as described above (Fig. 3.7). Model reduction, via pseudo-time approximations (which reduces run time to ~10 minutes per run), makes a computational optimization of the local cellular environment to investigate the effects on differentiation feasible. For example, altering the Notch-Delta profile or other spatial patterning queues (e.g. the glial switch signal) could be used for *in silico* drug testing and predictive neurotoxicity systems. Similarly, existing knowledge of an injury milieu could inform potential differentiation trajectories for transplanted cells. Additionally, the model could be used to quantitatively compare pattern evolution between developmental systems and *in vitro* data in order to reveal both conserved and divergent mechanisms. Importantly, mPSC and hPSC differentiation to MN and OPC follow a largely conserved developmental course, including acquisition of an Olig2+ progenitor state, followed by generation of $Hb9^{+}$ motor neurons and $Olig2^{+}/Nkx2.2^{+}$ OPCs [47-49]. Human and murine

protocols for the differentiation of PSC to MN and OPC often involve a three dimensional (3D) process in the presence of both a Shh agonist and RA resulting in heterogeneous cultures, although hPSC require a longer time course. Though MN have been derived in 2D, these protocols also produce heterogeneous cultures similar to 3D differentiation and often include fluorescence sorting, DAPT addition and/or sedimentation of 3D cell clusters for MN enrichment of cultures [50-53]. This flexible modeling platform allows for direct comparison human and murine data, revealing both consistencies and divergences within the developmental time course.

Unidentified cell types likely affect differentiation in dynamic cultures, possibly by redundant or compensatory signaling. However, our interpretation(s) of Notch and Tgf-β and the mechanisms by which they govern differentiation, remain constant regardless of the cell source. Notch signaling occurs in much of the ventricular region of the neural tube [18, 54], likely among the cell types generated within aggregates. Additionally, conditioned media from both GFP^+ and GFP^- cultures generated an increase in the ratio of OPC to MN (Fig. 3.4), indicating a switch signal emanates from both MN and at least one other late-arising cell population, though this mechanisms is modeled specifically as a function of the total number of MN (Fig. 3.3). Tgf-β family members are expressed both in pMN and the motor columns *in vivo* [24]. Therefore, though Tgf-β likely derives from multiple cell sources, the mechanism and timing of the fate switch remains the same. Given that *in vitro* spatial organization is highly disrupted compared to *in vivo*, cells likely experience contact with cell types we would not expect from traditional animal studies. This is one strength of a combined *in vitro* and computational approach: cells encounter novel or disrupted microenvironments. Computational models

are built largely on both *in vivo* and *in vitro* literature, which experimental data can confirm or refute.

In contrast to typical molecular biological studies, which focus on temporally and mechanistically constrained hypotheses, new computational modeling tools enable us to view multicellular signaling and differentiation in a dynamic and experimentally intractable context. For example, contrasting studies find that Notch-Delta inhibition (1) increases progenitor pools [16], (2) decreases progenitor pools and increases neuronal differentiation [23], and (3) increases glial differentiation [18]. Each study on its own has merit, but more inclusive techniques are needed to interrogate such diverse phenomena and their emergent outcomes. Our findings confirm Notch-Delta inhibition in augmented Shh signaling throughout the pMN lineage, and further suggest a Notch- and Tgf-β-dependent Olig2 stabilization function. Iterative, top-down deconstruction of pMN fate decisions simultaneously accounts for, and distinguishes between, these concomitant but distinct mechanisms. Finally, a three dimensional agent-based model, built on these mechanistic insights, will facilitate future investigations to yield a more comprehensive picture of the molecular underpinnings of pMN cellular fate decisions.

Methods

ES cell culture

The HBG3 mESC cell line was a gift from the lab of Dr. Hynek Wichterle. ES cells were maintained as previously described [19]. Briefly, mitomyocin C-inactivated mouse embryonic fibroblasts (MEF) were plated at 50,000 cells/cm2 for 24-48 hours in media consisting of DMEM with 4500 mg/L Glucose (HyClone Laboratories), supplemented with Defined FBS (10%, HyClone Laboratories), Penicillin/Streptomycin

(50 U/ml, ThermoFisher) and L-Glutamine (4 mM, ThermoFisher). HBG3 mESCs were plated on inactivated MEFs in ESC medium consisting of EmbryoMax DMEM with 4500 mg/L glucose and 2250 mg/L $NaHCO_3$ (Milllipore), Non-Essential Amino Acids (1x, ThermoFisher), Nucleosides (1x, Millipore), L-Glutamine (2 mM, ThermoFisher), Penicillin/Streptomycin (50 U/ml, ThermoFisher), Defined FBS (15%, HyClone Laboratories), Beta-mercaptoethanol (100 nM, Sigma) and murine LIF (1000 U/ml, Millipore). Cells were between passage 15 and 19 for all experiments. Cells were expanded and frozen in ESC medium supplemented with 10% DMSO until use.

ES cell differentiation

HBG3 were differentiated as described [19], with minor adjustments. Briefly, HBG3 mESCs were thawed (day 0) directly into differentiation medium consisting of a 1:1 mixture of AB2 (Aruna Biomedical) and Advanced DMEM/F12 (ThermoFisher) supplemented with Knockout Serum Replacement (10%, ThermoFisher), L-Glutamine (2 mM, ThermoFisher), Penicillin/Streptomycin (50 U/ml, ThermoFisher), and Beta-mercaptoethanol (100 nM, Sigma). To remove MEFs, cells were thawed onto 10 cm, tissue culture treated plates pre-coated and dried with 0.1% gelatin (Sigma) for one hour at 37° C. After the initial MEF removal, cells were strained through a 70 μm mesh cell strainer (Corning) and reseeded into 10 cm petri dishes in where they self-aggregated, and were maintained in rotary culture on an Orbi-shaker Jr. (Benchmark Scientific) at 50 rpm for the duration of the differentiation protocol. Cells were maintained in basal differentiation medium for 72 hours post-thaw with daily media changes (days 1-3). At 48 and 72 hours post-thaw, media was supplemented with retinoic acid (RA, 1 μM) and Purmorphamine (Pur, 1 μM). A final media change occurred day 6 which included both

RA and Pur, as well as BDNF (R & D Systems) and GDNF (Neuromics), both at 10 ng/ml. N-[N-(3, 5-difluorophenacetyl)-l-alanyl]-S-phenylglycine t-butyl ester (DAPT, 1 μM, Sigma) was added daily to cultures beginning on day 3 or 7, as indicated.

Immunocytochemistry and Imaging

Immunocytochemistry was performed on intact embryoid bodies (EB) as described[2], with minor modifications. Briefly, EBs were fixed in Formalde-Fresh (ThermoFisher) for 45 minutes. EBs were then permeabilized for 30 minutes in 1.0% Triton X-100 in phosphate buffered saline with calcium and magnesium (PBS++, HyClone), and re-fixed in formalin for 15 minutes. EBs were blocked in blocking buffer (2% bovine serum albumin, 0.1% Tween-20 in PBS++) for 4 hours. Samples were immunolabelled with rabbit anti-Olig2 (1:500, EMD Millipore) and mouse anti-Nkx2.2 (1:5, Developmental Hybridoma Studies Bank) antibody overnight at 4°C in blocking buffer. After three five-minute washes in blocking buffer, EBs were subsequently stained with a secondary anti-rabbit AlexaFluor 546 and anti-mouse AlexaFluor 647 secondary antibodies (both 1:1000, ThermoFisher) for 4 hours. EBs were then immunolabelled with conjugated rabbit anti-GFP AlexaFluor 488 (ThermoFisher). Hoechst (1:2000) nuclear labeling was then performed for 15 minutes in fresh blocking buffer. Samples were washed 3 more times for five minutes each, resuspended in blocking buffer, and imaged using a 40X oil objective on a Zeiss LSM 710 Confocal Microscope at the Biomedical Microscopy Core at the University of Georgia. EBs were imaged at z-intervals of 2 μM for 80-100 μm.

Conditioned media experiment

To obtain MN-enriched and -depleted conditioned media, EBs were differentiated as described above. At day 7, EBs were dissociated using 0.05% Trypsin (ThermoFisher) for 6 minutes with trituration at 3 minutes. Trypsin was quenched with an equal volume of 20% FBS in DMEM/F12 (ThermoFisher), followed by another trituration post-quench. Dissociated cells were passed through a 70 μm cell strainer (Corning) in differentiation media for fluorescence-activated cell sorting (FACS). FACS was performed with a Bio-Rad S3 cell sorter at the CTEGD Cytometry Shared Resource Laboratory at the University of Georiga. Both GFP^+ and GFP^- cell fractions were replated at 100,000 cells /cm2 in 6-well dishes. Dishes were precoated with Growth Factor Reduced (GFR) Matrigel (Corning) at a 1:100 dilution in DMEM/F12 for 45 minutes and rinsed twice with PBS with magnesium and calcium prior to sorting. Conditioned media was collected at 48 hours and frozen at -80° C. For conditioned media from immature cultures, EBs were dissociated at day 2, and replated as above. For conditioned media experiments, aggregates were differentiated as described to day 5, where they were dissociated and replated onto GFR-Matrigel-coated 96-well plates at 100,000 cells/cm2 in fresh differentiation medium supplemented with 1 μM RA, 1 μM Pur, 1 μM DAPT (Sigma-Aldrich), and 10 μM ROCK Inhibitor (Tocris). 24 hours post plating, media was replaced with 3:1 mix of conditioned media to fresh differentiation media with the following supplements (final concentration): RA (1 μM), Pur (1 μM), DAPT (1 μM), BDNF (10 ng/ml), GDNF (10 ng/ml). Cells were allowed to differentiate for 48 hours, then fixed in 4% paraformaldehyde (Electron Microscopy Sciences) in PBS++. Immunocytochemistry was performed as above except incubation times were shortened

to 1 hour. Whole wells were imaged as tiles with a 20x objective on a Zeiss 710 Confocal Microscope using four channels and a 21 μm, 3-plane z-stack.

Tgf-β Experiments

For Tgf-β experiments, cells were differentiated in aggregates as above. At day five, cells were dissociated to 60 mm, Matrigel coated plates in HBG3 Diff supplemented with 1 μM Pur, 1 μM RA, 10 μM ROCKi plus either the Tgf-β inhibitor SB431542 [26] (10 μM, Sigma-Aldrich) or Tgf-β2 (10 ng/ml, EMD Millipore). After 48 hours, media was changed to that containing either DAPT (5 μM) or an equal volume of DMSO. After 48 hours, cells were dissociated with trypsin, washed once in PBS without magnesium or calcium (PBS -/-) and fix in 4% PFA in PBS -/-. 10^6 cells were transferred to a V-bottom 96 well plate where all subsequent steps occurred on ice. Cells were permeabilized with 0.1% Triton-X 100 in PBS -/- and washed twice in PBS -/-. Cells were blocked in 1% BSA in PBS -/- (blocking buffer) for one hour. Cells were then incubated with Olig2 (1:500, EMD Millipore) or Nkx2.2 (1:10, DHSB) for 60 minutes in blocking buffer. Cells were washed three time for 5 minutes in blocking buffer and incubated with Alexfluor 546 or 633 at 1:2000 for 30 minutes. After three washes in blocking buffer, cells were resuspended in PBS- -/- for analysis by flow cytometry, including unstained cells and FMO controls for each antibody. Flow cytometry was performed on a Beckman Coulter Cytoflex. Flow cytometry results were analyzed using the open-source, density- and cluster-based FLOCK package [55] freely available through the National Institute of Allergy and Infectious Diseases (NIAID). Briefly, the workflow was performed as suggested, and consisted of automated quality control on each sample, followed by automatic gating and conversion. All samples were merged

and FLOCK analysis was run on the merged dataset. Like populations were auto-collapsed and centroids were determined based on the software algorithm. CrossSample analysis was then run on each dataset individually and final cell fractions were taken from output file. The complete dataset will be published through the NIAID website (Immport.org).

Spatial Pattern Analysis

Spatial pattern analysis was performed as described previously [3] with the following modifications.

Cell Segmentation and Identification

Nuclei segmentation was performed with the commercial software package IMARIS. IMARIS enabled reproducible segmentation results across all images regardless of background staining or changes in intensity. Briefly, the nuclei segmentation tool was used to segment cells which consists of a Gaussian smoothing operation, a subsequent background subtraction, followed by aggressive adaptive thresholding, and finally a watershed morphology based seeding to segment individual nuclei. Nuclei were then sorted based on size and a quality metric. Next, the three other channels, red (Olig 2), green (Hb9) and cyan (Nkx2.2) were analyzed using the nuclei as a mask. The mean fluorescence and standard deviation for each channel were exported and processed using python to determine subsequent cellular staining identities. Cellular staining thresholds were originally assigned using an ensemble method which chose between a global otsu, yen and li threshold via the python skimage package. However, this ensemble method often led to a conservative threshold, which resulted in significant background in roughly

40% of the images, particularly for the HB9 channel. Thus the thresholds were adjusted by hand to maximize internal cell signal while eliminating background staining.

Network Reconstruction and Network Based Pattern Analysis

Once the position of the nuclei along with their identities were determined from the cell segmentation and identification step outlined above, this information as fed into the network reconstruction algorithm. In the sequence of direct cellular connectivity information, this algorithm performs a Delaunay triangulation (from the scipy.spatial package) on the nuclei locations to construct a most likely network representation. In this case, due to varying cell densities across cell aggregates, and even within cellular aggregates, the triangulations were pruned based on distance and maximum number of possible connections. The segmentation process outlined above detected cells at a maximum of 2-3 cell layers deep within the aggregate (which agrees with the limitations of confocal microcopy in cellular aggregates) and thus the maximum connectivity was set to 9 for network reconstruction purposes. Due to the lens-like shape of the reconstructions, radial distance metrics were omitted from the analysis. Furthermore, to remove bias associated with cell numbers, all metrics were normalized by the number of cells of that type present in the aggregate. Two new classes of metrics were added: one to further examine cellular clustering within cell types, and another to examine co-localization of different cell types. To provide more information on the cellular clusters (where a cluster is defined as 2 or more spatially adjacent cells of the same type) the average cluster-cluster distance and standard deviation as well as the number of cells in clusters, and those not in clusters were added. To elucidate interactions between different cell types, an association metric was added. The association metric was calculated over

all cells asking how many cells of a certain type could be found within all primary or secondary neighbors. Three different cell types were examined for association: pMN ($Olig2^+/Nkx2.2^-$), motor neurons (GFP^+, and oligodendrocytes ($Nkx2.2^+/Olig2^+$).

Principal Component Analysis:

Principal component analysis was performed as described previously using the python sklearn package [3].

Stochastic Modeling:

Stochastic modeling was performed using the python programming language. Code is available at the following link [...]. Generally an object oriented programming approach was used in which a cell object was allowed to transition to different fates according to the schematics shown in Figures 3.3 & 3.4. The initial cell population was assumed to be asynchronous and this was modeled via the addition of a randomized offset according to the following equation:

$$divsion\ delay = U(0,1) * division\_time$$

Where the division delay represents is generated from a random uniform distribution and then scaled by the division time of the cell. When a cell reached its expected division time, the probability that it differentiated into two states s1, and s2 were calculated according to probability equations. This setup allowed for symmetric and asymmetric division of progenitor cells. It is important to note that the transient progenitor state did not lead to amplification of the cell type, rather this state purely underwent conversion towards a motor neuron fate. In the model this was denoted by only defining the first state s1, while the second state s2 was set to “none”. The

probability equations for the random, feedback, and transient progenitor schemes are shown below:

Random

$$P(NSC \rightarrow prog) = \propto$$

$$P(NSC \rightarrow NSC) = 1 - \propto$$

$$P(prog \rightarrow prog) = \beta$$

$$P(prog \rightarrow mn) = (1 - \beta) * \gamma$$

$$P(prog \rightarrow olig) = (1 - \beta) * (\gamma - 1)$$

Where α=0.2, δ=0.06, β=0.65

Feedback

$$P(NSC \rightarrow prog) = \propto$$

$$P(NSC \rightarrow NSC) = 1 - \propto$$

$$P(prog \rightarrow prog) = \beta$$

$$\delta = \frac{\gamma}{\left(1.0 - \left(\frac{\#mn}{k1}\right)^{n1}\right)}$$

$$P(prog \rightarrow mn) = (1 - \beta) * \delta$$

$$P(prog \rightarrow olig) = (1 - \beta) * (\delta - 1)$$

Where α = 0.275, β = 0.7, γ=0.8, k1=120.0, n1=20.0

Transient

$$\varepsilon = 1.0 - \frac{1.0}{\left(1.0 - \left(\frac{\#prog + \#prog\_t}{k2}\right)^{n2}\right)}$$

$$P(NSC \rightarrow prog) = \propto * \varepsilon$$

$$P(NSC \rightarrow t\_prog) = (1 - \propto * \varepsilon)$$

$$P(NSC \rightarrow NSC) = 1 - (1 - \propto * \varepsilon)$$

$$P(prog \rightarrow prog) = \beta$$

$$\delta = \frac{\gamma}{\left(1.0 - \left(\frac{\#mn}{k1}\right)^{n1}\right)}$$

$$P(prog \rightarrow mn) = (1 - \beta) * \delta$$

$$P(prog \rightarrow olig) = (1 - \beta) * (\delta - 1)$$

$$P(t\_prog \rightarrow mn) = \delta$$

$$P(t\_prog \rightarrow t\_prog) = (\delta - 1)$$

Where α = 0.275, β = 0.7, γ=0.8, k1=120.0, n1=20.0, k2 = 100, n2 = 5.5

In all cases the initial conditions for the simulation where all cell populations set to 0, except for neural stem cells, which start with a population of 140 cells. Parameters were fit by hand comparison of the experimental data and computational models. In the case of Figure 3.3, the initial random, feedback, and transient models were fit to the control data set. In the case of Figure 3.4, the DAPT treatments at Day 3, and Day 7 were used to fit the computational models. The equations used for the influence of DAPT in Figure 3.4 are outlined below where for the sake of brevity, only changed or new equations from the previous transient model are shown:

DAPT promotes glia:

$$P(prog \rightarrow mn) = (1 - \beta) * \delta$$

$$P(prog \rightarrow olig) = (1 - \beta) * (\delta - 1)$$

Where δ = 1.

DAPT promotes motor neurons:

$$P(prog \rightarrow mn) = (1 - \beta) * \delta$$

$$P(prog \rightarrow olig) = (1-\beta) * (\delta - 1)$$

Where $\delta = 0$.

Always Transient Progenitor

$$P(prog \rightarrow t\_prog) = DAPT * \theta$$

$$\propto = \propto * (1 + DAPT * \tau)$$

$$\beta = \frac{\beta}{1 + DAPT * \omega}$$

Where $\omega = 1.25$, $\tau = 1.5$, $\theta = 0.75$

True Model

$$P(prog \rightarrow t\_prog) = DAPT * Anchor * \theta$$

$$\propto = \propto * (1 + DAPT * \tau)$$

$$\beta = \frac{\beta}{1 + DAPT * \omega}$$

Where $\omega = 1.25$, $\tau = 1.5$, $\theta = 0.75$

DAPT was modeled as a Boolean variable, set to 0 when DAPT is not present, and 1 when DAPT is present. Olig2 anchoring in the nucleus is represented with the Boolean variable *Anchor*, which is set to 0 for DAPT treatment at Day 3, and one for DAPT after the glial switch at Day 7. Since the time delay for DAPT to take effect was not explicitly modeled in these equations, a time delay was introduced by simulating addition of DAPT half a day after it was added. This resulted in DAPT addition at days 3.5 and day 7.5 to simulate day 3 and day 7 treatments respectively.

Across all simulations the same division times were used for each cell type 18 hours for neural stem cells, progenitors, and transient progenitors, while motor neurons and glial cells were assumed to be terminally differentiated and did not divide. Cell death

was calculated at each step, where a cell had a 2% probability of dying as fit from experimental data.

3D Aggregate Modeling:

Once a suitable scheme was determined via the stochastic modeling this scheme was adapted to a 3D aggregate model. The modeling was performed as previously described [3] with the following modifications. A 500 cell aggregate was investigated, with ~100 cells starting in the neural stem cell state, with the remainder making up an unstained cell population. To eliminate excess computational overhead for collisions and simulating multiple cell types, the unstained cells were assumed to divide relatively slowly (division time = 50 hours), and a pseudotime axis was used to simulate the cells dividing over a 100 time-step period. This time axis was then mapped back to the 168 hour experimental time frame. A rapid collision detection method using a KDTree was implemented. Cellular division times were assumed to be 21 hours for neural stem cells, an average of 15 hours for transient progenitors, 18 hours for Olig2 positive progenitors, and motor neurons/glial cells were assumed to not divide. Furthermore, while the relationships governing motor neuron feedback were assumed to be rapid soluble signals which were modeled only as a function of the number of motor neurons, the progenitor division was defined by local cell-cell interactions. The local cell-cell interactions were based on feedback from neighboring transient and Olig2+ progenitor cells, normalized by the total number of neighbors. The equations governing the state transition are outlined below:

$$\varepsilon = 1.0 - \frac{1.0}{\left(1.0 - \left(\frac{\dot{prog} + \dot{prog\_t}}{k2}\right)^{n2}\right)}$$

$$\propto = \propto * (1 + \ DAPT * \tau)$$

$$P(NSC \rightarrow prog) = \propto * \ \varepsilon$$

$$P(NSC \rightarrow t\_prog) = (1 - \propto * \varepsilon)$$

$$P(NSC \rightarrow NSC) = \ 1 - (1 - \propto * \varepsilon)$$

$$P(prog \rightarrow prog) = \ \beta$$

$$\delta = \frac{\gamma}{\left(1.0 - \left(\frac{\#mn}{k1}\right)^{n1}\right)}$$

$$\beta = \frac{\beta}{1 + DAPT * \omega}$$

$$P(prog \rightarrow mn) = (1 - \beta) * \delta$$

$$P(prog \rightarrow olig) = \ (1 - \beta) * (\delta - 1)$$

$$P(t\_prog \rightarrow mn) = \delta$$

$$P(t\_prog \rightarrow t\_prog) = (\delta - 1)$$

$$P(prog \rightarrow t\_prog) = DAPT * Anchor * \theta$$

Where α = 0.4, β = 0.9, γ=0.7, k1=200.0, n1=20.0, k2 = .25, n2 = 7.5, ω = 1.25, τ = 1.5, θ = 0.75, and $\dot{prog} + \dot{prog}\_t$ is the normalized count of transient and Olig2^{+} progenitors present within a given cell's neighbors.

It is important to note that for the control scheme, the parameters had to be adjusted to take into account the lack of cell death in the 3D modeling approach. The new parameters were determined using a by hand fit method to capture the qualitative nature of the transitions occurring during the control and DAPT treatment at Day 7.

Code Availability

Code available to academic researchers upon request from the authors.

References

1. Moore, K.A. and I.R. Lemischka, *Stem Cells and Their Niches.* Science, 2006. **311**(5769): p. 1880-1885.
2. White, D.E., et al., *Spatial pattern dynamics of 3D stem cell loss of pluripotency via rules-based computational modeling.* PLoS Comput Biol, 2013. **9**(3): p. e1002952.
3. White, D.E., et al., *Quantitative multivariate analysis of dynamic multicellular morphogenic trajectories.* Integr Biol (Camb), 2015. **7**(7): p. 825-33.
4. Briscoe, J., et al., *A homeodomain protein code specifies progenitor cell identity and neuronal fate in the ventral neural tube.* Cell, 2000. **101**(4): p. 435-45.
5. Rowitch, D.H., *Glial specification in the vertebrate neural tube.* Nat Rev Neurosci, 2004. **5**(5): p. 409-19.
6. Mizuguchi, R., et al., *Combinatorial roles of olig2 and neurogenin2 in the coordinated induction of pan-neuronal and subtype-specific properties of motoneurons.* Neuron, 2001. **31**(5): p. 757-71.
7. Novitch, B.G., A.I. Chen, and T.M. Jessell, *Coordinate regulation of motor neuron subtype identity and pan-neuronal properties by the bHLH repressor Olig2.* Neuron, 2001. **31**(5): p. 773-89.
8. Zhou, Q., G. Choi, and D.J. Anderson, *The bHLH transcription factor Olig2 promotes oligodendrocyte differentiation in collaboration with Nkx2.2.* Neuron, 2001. **31**(5): p. 791-807.
9. Lu, Q.R., et al., *Common developmental requirement for Olig function indicates a motor neuron/oligodendrocyte connection.* Cell, 2002. **109**(1): p. 75-86.

10. Lee, S.K., et al., *Olig2 and Ngn2 function in opposition to modulate gene expression in motor neuron progenitor cells.* Genes Dev, 2005. **19**(2): p. 282-94.

11. Arber, S., et al., *Requirement for the homeobox gene Hb9 in the consolidation of motor neuron identity.* Neuron, 1999. **23**(4): p. 659-74.

12. Shen, Q., et al., *Asymmetric Numb distribution is critical for asymmetric cell division of mouse cerebral cortical stem cells and neuroblasts.* Development, 2002. **129**(20): p. 4843-53.

13. Sun, T., et al., *Cross-repressive interaction of the Olig2 and Nkx2.2 transcription factors in developing neural tube associated with formation of a specific physical complex.* J Neurosci, 2003. **23**(29): p. 9547-56.

14. Yoon, K. and N. Gaiano, *Notch signaling in the mammalian central nervous system: insights from mouse mutants.* Nat Neurosci, 2005. **8**(6): p. 709-15.

15. Louvi, A. and S. Artavanis-Tsakonas, *Notch signalling in vertebrate neural development.* Nat Rev Neurosci, 2006. **7**(2): p. 93-102.

16. Kong, Jennifer H., et al., *Notch Activity Modulates the Responsiveness of Neural Progenitors to Sonic Hedgehog Signaling.* Developmental Cell, 2015. **33**(4): p. 373-387.

17. Crawford, T.Q. and H. Roelink, *The Notch response inhibitor DAPT enhances neuronal differentiation in embryonic stem cell-derived embryoid bodies independently of sonic hedgehog signaling.* Developmental Dynamics, 2007. **236**(3): p. 886-892.

18. Rabadan, M.A., et al., *Jagged2 controls the generation of motor neuron and oligodendrocyte progenitors in the ventral spinal cord.* Cell Death Differ, 2012. **19**(2): p. 209-19.

19. Wichterle, H., et al., *Directed differentiation of embryonic stem cells into motor neurons.* Cell, 2002. **110**(3): p. 385-97.

20. Carpenedo, R.L., C.Y. Sargent, and T.C. McDevitt, *Rotary suspension culture enhances the efficiency, yield, and homogeneity of embryoid body differentiation.* Stem Cells, 2007. **25**(9): p. 2224-34.

21. Sinha, S. and J.K. Chen, *Purmorphamine activates the Hedgehog pathway by targeting Smoothened.* Nat Chem Biol, 2006. **2**(1): p. 29-30.

22. Geling, A., et al., *A gamma-secretase inhibitor blocks Notch signaling in vivo and causes a severe neurogenic phenotype in zebrafish.* EMBO Rep, 2002. **3**(7): p. 688-94.

23. Geling, A., et al., *A γ-secretase inhibitor blocks Notch signaling in vivo and causes a severe neurogenic phenotype in zebrafish.* EMBO reports, 2002. **3**(7): p. 688-694.

24. Dutta, D.J., et al., *Combinatorial actions of Tgfbeta and Activin ligands promote oligodendrocyte development and CNS myelination.* Development, 2014. **141**(12): p. 2414-28.

25. Dias, J.M., et al., *Tgfbeta signaling regulates temporal neurogenesis and potency of neural stem cells in the CNS.* Neuron, 2014. **84**(5): p. 927-39.

26. Inman, G.J., et al., *SB-431542 is a potent and specific inhibitor of transforming growth factor-beta superfamily type I activin receptor-like kinase (ALK) receptors ALK4, ALK5, and ALK7.* Mol Pharmacol, 2002. **62**(1): p. 65-74.

27. Kopan, R. and M.X.G. Ilagan, *The Canonical Notch Signaling Pathway: Unfolding the Activation Mechanism.* Cell, 2009. **137**(2): p. 216-233.

28. Setoguchi, T. and T. Kondo, *Nuclear export of OLIG2 in neural stem cells is essential for ciliary neurotrophic factor-induced astrocyte differentiation.* J Cell Biol, 2004. **166**(7): p. 963-8.

29. Marumo, T., et al., *Notch signaling regulates nucleocytoplasmic Olig2 translocation in reactive astrocytes differentiation after ischemic stroke.* Neuroscience Research, 2013. **75**(3): p. 204-209.

30. Du, Z.W., et al., *Induced expression of Olig2 is sufficient for oligodendrocyte specification but not for motoneuron specification and astrocyte repression.* Mol Cell Neurosci, 2006. **33**(4): p. 371-80.

31. Mazzoni, E.O., et al., *Synergistic binding of transcription factors to cell-specific enhancers programs motor neuron identity.* Nat Neurosci, 2013. **16**(9): p. 1219-27.

32. Koch, U., R. Lehal, and F. Radtke, *Stem cells living with a Notch.* Development, 2013. **140**(4): p. 689-704.

33. Das, R.M. and K.G. Storey, *Mitotic spindle orientation can direct cell fate and bias Notch activity in chick neural tube.* EMBO Reports, 2012. **13**(5): p. 448-454.

34. Bultje, R.S., et al., *Mammalian Par3 Regulates Progenitor Cell Asymmetric Division via Notch Signaling in the Developing Neocortex.* Neuron, 2009. **63**(2): p. 189-202.

35. Nery, S., H. Wichterle, and G. Fishell, *Sonic hedgehog contributes to oligodendrocyte specification in the mammalian forebrain.* Development, 2001. **128**(4): p. 527-40.

36. Danesin, C., et al., *Ventral neural progenitors switch toward an oligodendroglial fate in response to increased Sonic hedgehog (Shh) activity: involvement of Sulfatase 1 in modulating Shh signaling in the ventral spinal cord.* J Neurosci, 2006. **26**(19): p. 5037-48.

37. Touahri, Y., et al., *Sulfatase 1 promotes the motor neuron-to-oligodendrocyte fate switch by activating Shh signaling in Olig2 progenitors of the embryonic ventral spinal cord.* J Neurosci, 2012. **32**(50): p. 18018-34.

38. Chung, A.Y., et al., *Indian hedgehog B function is required for the specification of oligodendrocyte progenitor cells in the zebrafish CNS.* J Neurosci, 2013. **33**(4): p. 1728-33.

39. Yu, K., S. McGlynn, and M.P. Matise, *Floor plate-derived sonic hedgehog regulates glial and ependymal cell fates in the developing spinal cord.* Development, 2013. **140**(7): p. 1594-604.

40. Al Oustah, A., et al., *Dynamics of sonic hedgehog signaling in the ventral spinal cord are controlled by intrinsic changes in source cells requiring sulfatase 1.* Development, 2014. **141**(6): p. 1392-403.

41. Ravanelli, A.M. and B. Appel, *Motor neurons and oligodendrocytes arise from distinct cell lineages by progenitor recruitment.* Genes Dev, 2015. **29**(23): p. 2504-15.

42. Briscoe, J., et al., *Homeobox gene Nkx2.2 and specification of neuronal identity by graded Sonic hedgehog signalling.* Nature, 1999. **398**(6728): p. 622-7.

43. Amoutzias, G.D., et al., *Choose your partners: dimerization in eukaryotic transcription factors.* Trends Biochem Sci, 2008. **33**(5): p. 220-9.

44. Chen, J.-A., et al., *Mir-17-3p Controls Spinal Neural Progenitor Patterning by Regulating Olig2/Irx3 Cross-Repressive Loop.* Neuron, 2011. **69**(4): p. 721-735.

45. Li, H., et al., *Phosphorylation regulates OLIG2 cofactor choice and the motor neuron-oligodendrocyte fate switch.* Neuron, 2011. **69**(5): p. 918-29.

46. Liu, Z., et al., *Induction of oligodendrocyte differentiation by Olig2 and Sox10: Evidence for reciprocal interactions and dosage-dependent mechanisms.* Developmental Biology, 2007. **302**(2): p. 683-693.

47. Hu, B.-Y., et al., *Human oligodendrocytes from embryonic stem cells: conserved SHH signaling networks and divergent FGF effects.* Development, 2009. **136**(9): p. 1443-1452.

48. Davis-Dusenbery, B.N., et al., *How to make spinal motor neurons.* Development, 2014. **141**(3): p. 491-501.

49. Hu, B.Y., et al., *Human oligodendrocytes from embryonic stem cells: conserved SHH signaling networks and divergent FGF effects.* Development, 2009. **136**(9): p. 1443-52.

50. Steinbeck, Julius A., et al., *Functional Connectivity under Optogenetic Control Allows Modeling of Human Neuromuscular Disease.* Cell Stem Cell. **18**(1): p. 134-143.

51. Calder, E.L., et al., *Retinoic Acid-Mediated Regulation of GLI3 Enables Efficient Motoneuron Derivation from Human ESCs in the Absence of Extrinsic SHH Activation.* J Neurosci, 2015. **35(**33): p. 11462-81.

52. Qu, Q., et al., *High-efficiency motor neuron differentiation from human pluripotent stem cells and the function of Islet-1.* 2014. **5**: p. 3449.

53. Shin, S., S. Dalton, and S.L. Stice, *Human motor neuron differentiation from human embryonic stem cells.* Stem Cells Dev, 2005. **14**(3): p. 266-9.

54. Stasiulewicz, M., et al., *A conserved role for Notch signaling in priming the cellular response to Shh through ciliary localisation of the key Shh transducer Smo.* Development, 2015. **142**(13): p. 2291-2303.

55. Qian, Y., et al., *Elucidation of seventeen human peripheral blood B-cell subsets and quantification of the tetanus response using a density-based method for the automated identification of cell populations in multidimensional flow cytometry data.* Cytometry B Clin Cytom, 2010. **78 Suppl 1**: p. S69-82.

Figure 3.1. Generation and network transformation of cell types

(a) Differentiation diagram for the derivation of cell types including patterning factors (RA, Pur) and neuronal survival factors (BDNF, GDNF). Representative z-slice from a day 9 aggregate depicting immunocytochemistry for (b) Olig2, (c) GFP and (d) Nkx2.2. (e) Tri-color, merged projection image of z-stack. (f) Cells were identified as pMN ($Olig2^{+}/Nkx2.2^{-}$, red arrows), MN (GFP^{+}, green arrows) and OPC ($Olig2^{+}/Nkx2.2^{-}$, white arrows). (g) Representative image of converted network including unlabeled cells (blue), pMN (red), MN (green) and OPC (cyan). RA, retinoic acid; Pur, purmorphamine; BDNF, brain-derived neurotrophic factor; GDNF, glial cell line-derived neurotrophic factor. Scale bar represents 100 μm.

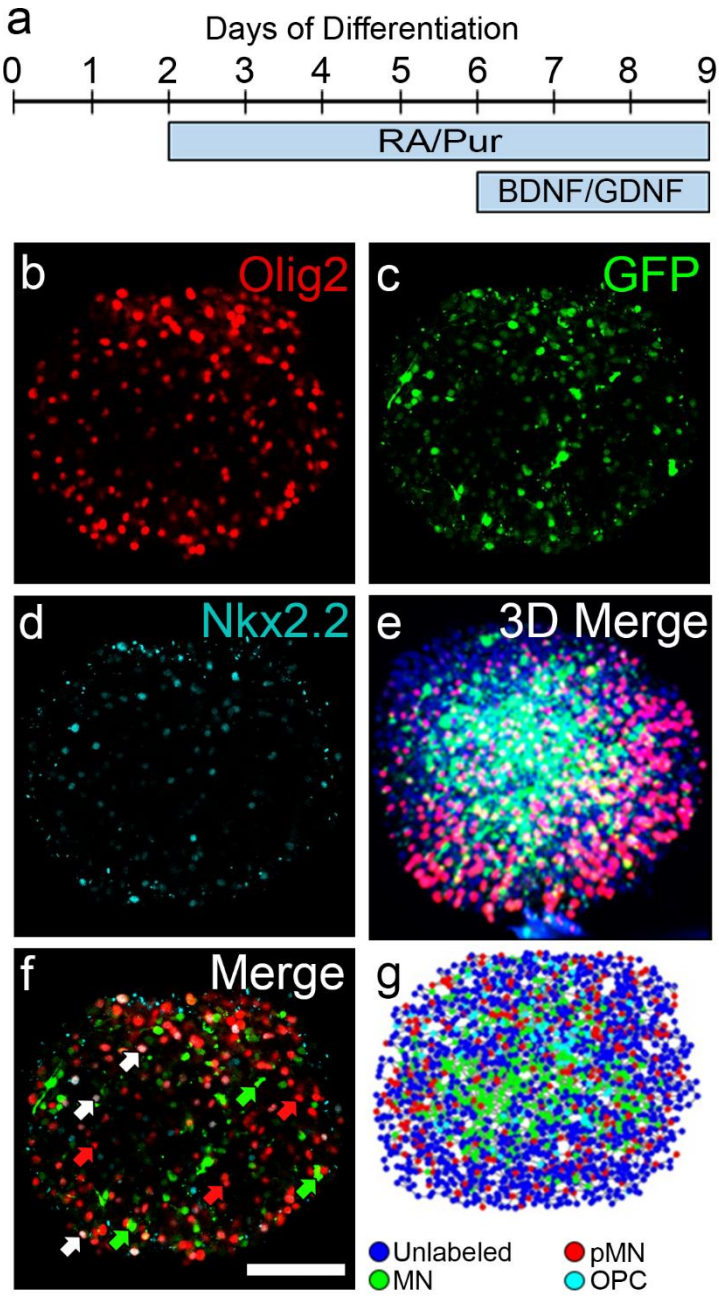
a
Days of Differentiation
0 1 2 3 4 5 6 7 8 9
RA/Pur
BDNF/GDNF
b Olig2
c GFP
d Nkx2.2
e 3D Merge
f Merge
g
Unlabeled
MN
pMN
OPC

Figure 3.2. Principal component analysis of spatial data

(a) Principal component analysis of the multidimensional pattern analysis performed on control stem cell aggregates receiving no DAPT. Principal component 1 and 2 captured 23.82% and 15.18% of the variance respectively. Each symbol represents a single aggregate with different symbols representing different days (n = 10-11 per time point). (b) Heatmap showing how different metrics contribute to each PCA axis.

a

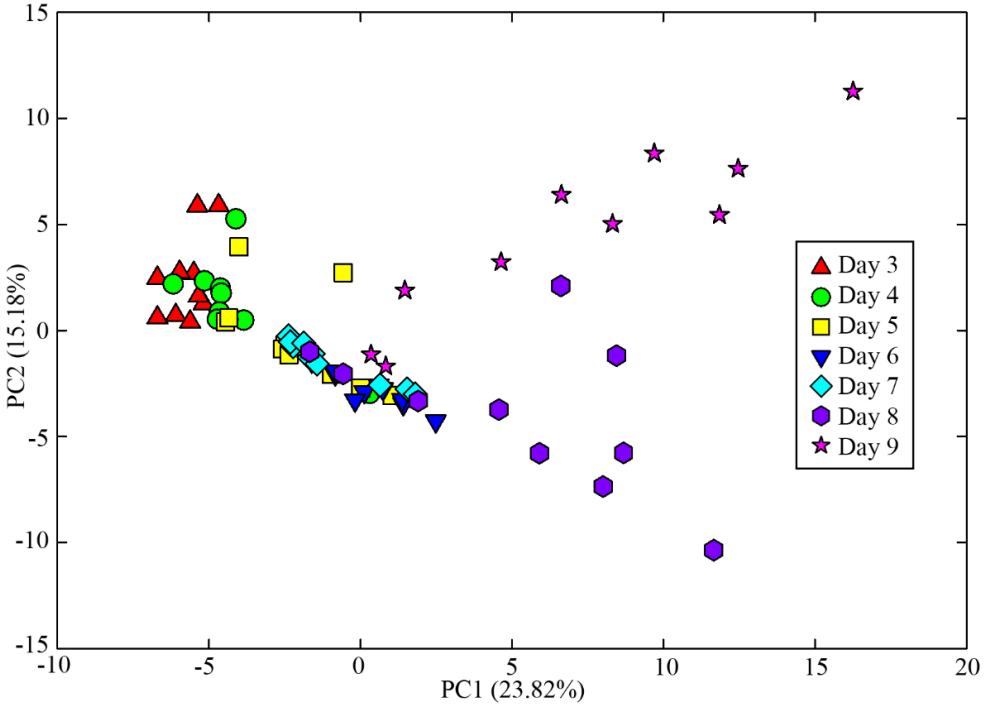
PC2 (15.18%)
PC1 (23.82%)
Day 3
Day 4
Day 5
Day 6
Day 7
Day 8
Day 9

b

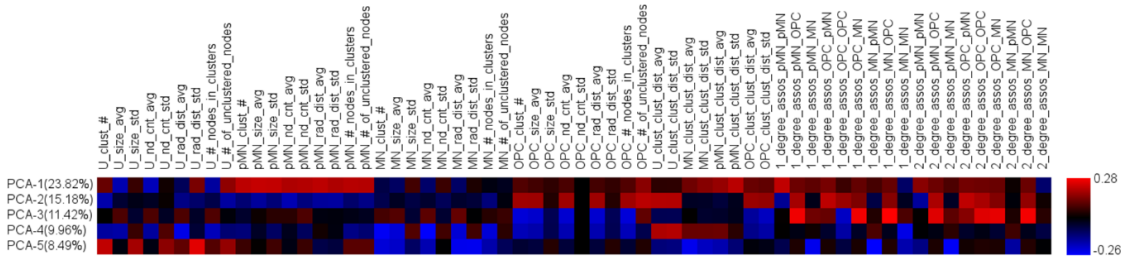
PCA-1(23.82%)
PCA-2(15.18%)
PCA-3(11.42%)
PCA-4(9.96%)
PCA-5(8.49%)
0.28
-0.26

Figure 3.3. Stochastic models suggest MN-mediated negative feedback and a transient pMN state can explain aggregate differentiation dynamics.

Schematics for three separate differentiation schemes modeled including (a) random, (e) feedback and (i) feedback/transient. (a) Random simulations incorporate consistent rates of differentiation for all processes. (e) Feedback schematics represent a negative feedback from MN self-limiting their generation. (i) Transient/Feedback represents feedback mechanism and existence of both mitotic and transient pMN states. (b-l) Plots depict average simulated (n = 10) and experimental cell quantities over time. Experimental data (solid lines) and average simulated data (dashed lines) +/- 1 standard deviation (shaded area) (n = 10). (b,f,j) pMN trajectories, (c,g,k) MN trajectories and (d,h,l) OPC trajectories are depicted for each schematic. Error bars for experimental data represent standard deviation.

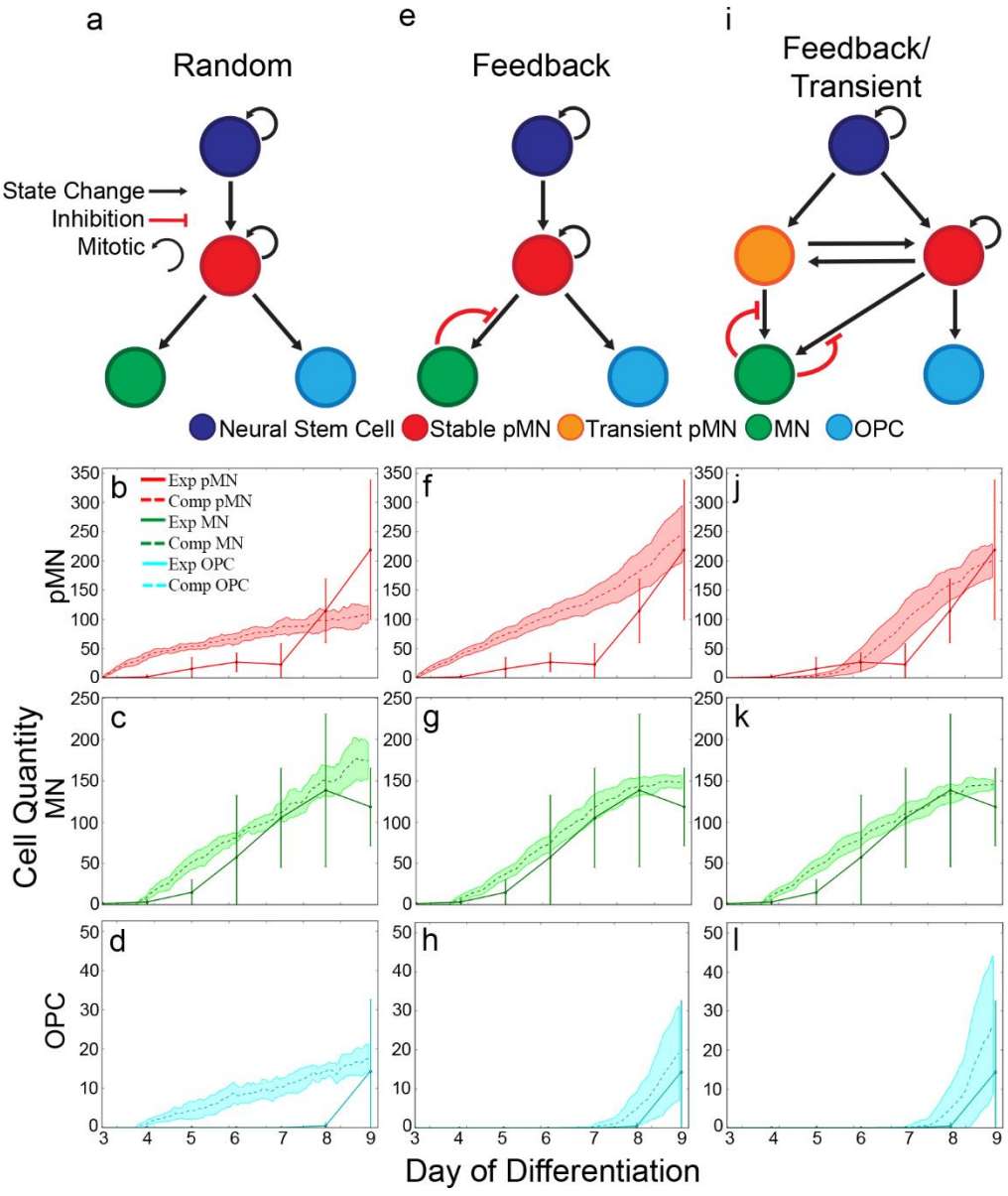
a
Random
e
Feedback
i
Feedback/
Transient
State Change
Inhibition
Mitotic
Neural Stem Cell
Stable pMN
Transient pMN
MN
OPC
b
Exp pMN
Comp pMN
Exp MN
Comp MN
Exp OPC
Comp OPC
f
j
c
g
k
d
h
l
pMN
MN
OPC
Cell Quantity
Day of Differentiation

Figure 3.4. Conditioned media from both MN-enriched and -depleted day 7 cultures increases the OPC:MN ratio over media from day 2 cultures.

Representative images of dissociated day 5 cultures after 48 hours in (a) immature, (b) MN-enriched and (c) MN-depleted conditioned media. Insets depict $Olig2^{+}/Nkx2.2^{+}$ OPC generation for each condition. (d) Box plots of OPC:MN ratio for each condition. Data represent 2 biological replicates of 3 technical replicates each (Kruskal-Wallis One-way ANOVA on ranks $P=0.004$ and Tukey Test $^{*}P<0.05$). Center bar represents median. Red, Olig2; Green, GFP; Cyan, Nkx2.2. Scale bar represents 100 μm.

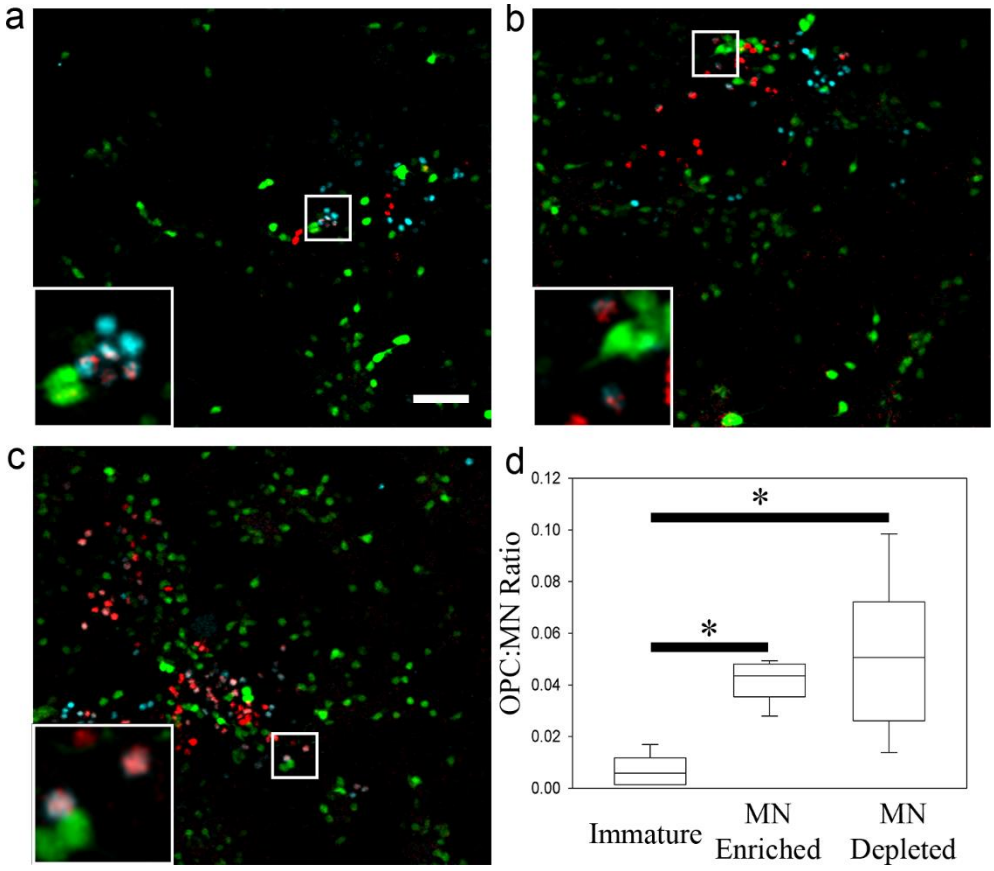
a
b
c
d
OPC:MN Ratio
0.12
0.10
0.08
0.06
0.04
0.02
0.00
*
*
Immature
MN Enriched
MN Depleted

Figure 3.5. Stochastic models suggest DAPT treatment pushes stable pMN towards transient pMN at day 3, but not at day 7.

(a, h, l) Schematics for differentiation schemes modeled. (a) DAPT increases transition from NSC towards transient pMN and stable pMN, from stable pMN towards transient progenitors and from stable pMN towards OPC. (h, i) Same as (a) with the introduction of an anchor term for Olig2: (h) Olig2 is not anchored at day 3, leading to increased transition from stable pMN to transient pMN under DAPT. (i) Olig2 is anchored on day 7 eliminating the stable MN to transient pMN transition. Plots depict average simulated (n = 10) and experimental (n=10 per time point) cell quantities over time. Plots depict experimental data (solid lines), and average simulated data (dashed lines) +/- 1 standard deviation (shaded area). (b-d, i-k) DAPT treatment beginning on Day 3. (e-g, m-o) DAPT treatment beginning on day 7. (b, e, i, m) Stable pMN, (c, f, j, n) MN and (d, g, k, o) OPC are depicted for each schematic. Error bars for experimental data represent standard deviation.

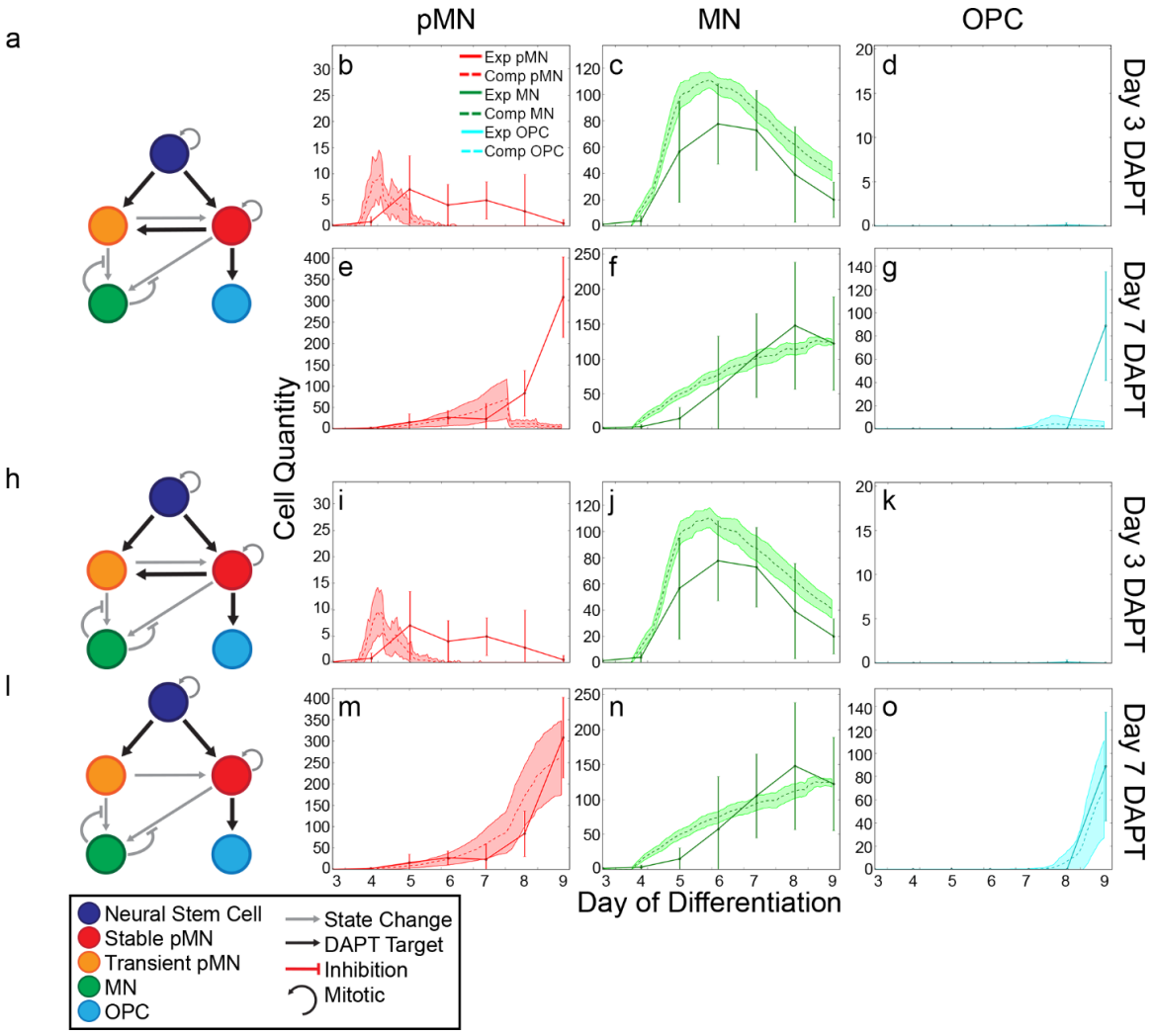
a
h
l
pMN
MN
OPC
b
c
d
e
f
g
i
j
k
m
n
o
Exp pMN
Comp pMN
Exp MN
Comp MN
Exp OPC
Comp OPC
Day 3 DAPT
Day 7 DAPT
Cell Quantity
Day of Differentiation
Neural Stem Cell
Stable pMN
Transient pMN
MN
OPC
State Change
DAPT Target
Inhibition
Mitotic

Figure 3.6. Tgf-β signaling, but not Nkx2.2 expression, is sufficient to block the effects of DAPT.

(a) Differentiation and treatment strategy for Tgf-β experiments. (b) Percent of each cell type per treatment. (c) $Nkx2.2^{+}$ and $Nkx2.2^{-}$ cells as a fraction of Olig2-expressing cells. (d) $Olig2^{+}$ and $Olig2^{-}$ cells as a fraction of Olig2-expressing cells. Error bars represent S.E.M. n = 3 biological replicates per treatment. Cell populations: MN, GFP^{+}; pMN, $Olig2^{+}/Nkx2.2^{-}$; OPC, $Olig2^{+}/Nkx2.2^{+}$. Differing letters represent $P<0.05$ by two-way ANOVA and Holm-Sidak multiple comparisons per each cell type/fraction. N.S., not significant. In (c) and (d), cell fractions were normalized to the average of all replicates prior to two-way ANOVA and Holm-Sidak multiple comparisons. Please see Supp. Table 1 for Two-Way ANOVA results table.

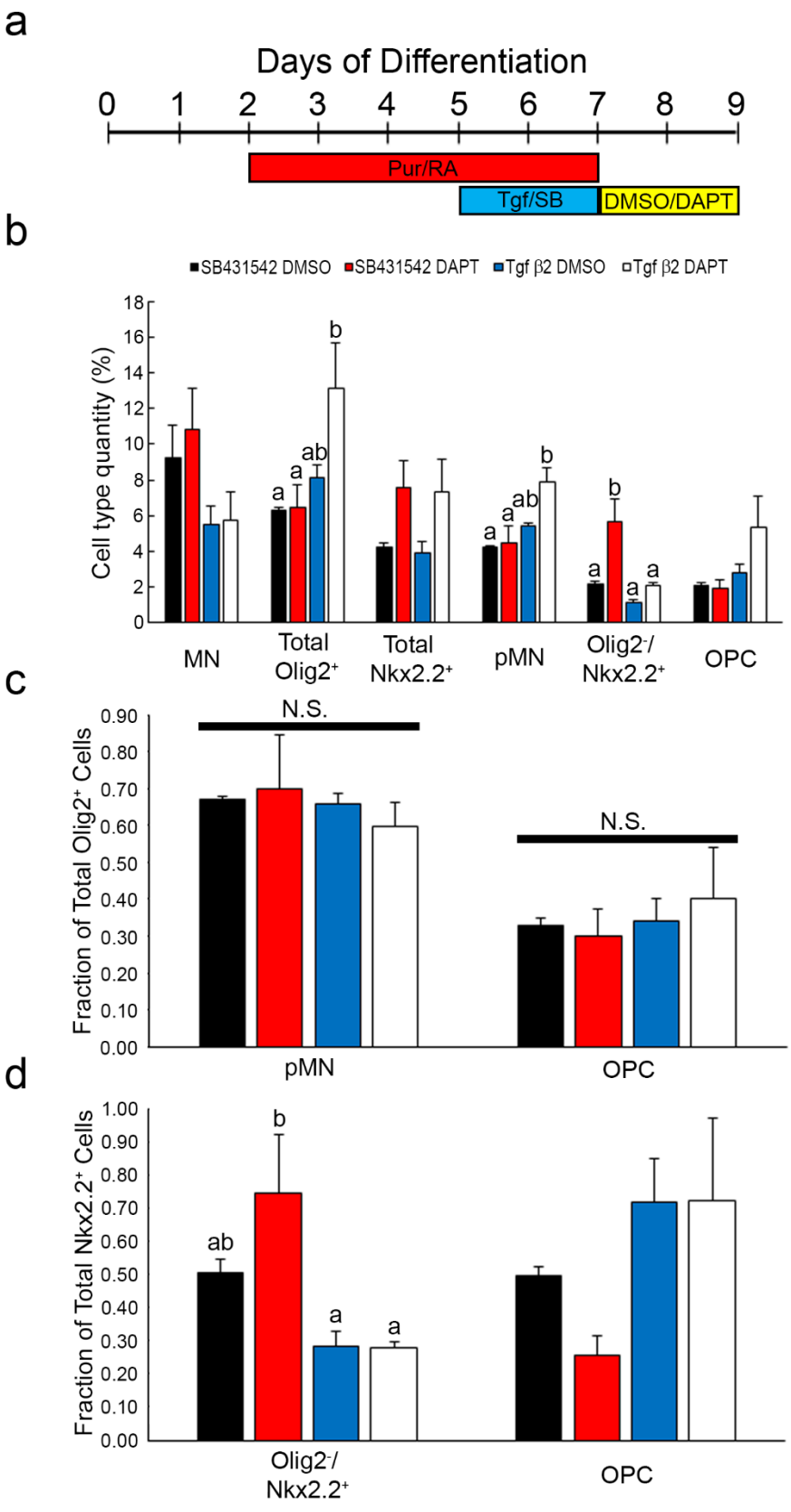
a
Days of Differentiation
0 1 2 3 4 5 6 7 8 9
Pur/RA
Tgf/SB
DMSO/DAPT
b
SB431542 DMSO
SB431542 DAPT
Tgf β2 DMSO
Tgf β2 DAPT
Cell type quantity (%)
MN
Total Olig2+
Total Nkx2.2+
pMN
Olig2-/ Nkx2.2+
OPC
c
Fraction of Total Olig2+ Cells
N.S.
N.S.
pMN
OPC
d
Fraction of Total Nkx2.2+ Cells
Olig2-/ Nkx2.2+
OPC

Figure 3.7. Three dimensional modeling predicts spatiotemporal evolution of progenitor. An agent based computational model was built on a trimmed principal component analysis. Representative images of simulated DMSO-treated (a-c) and DAPT-treated (d-f) aggregates from days 7-9. (g-i) Principal component analysis of simulated aggregates (n = 10). (j) Heatmap showing how each metric contributed to principal components. (k) Principal component analysis of experimental aggregates at day 9. Blue circles represent unlabeled cells, red represent pMN, green represent MN and black represent OPC.

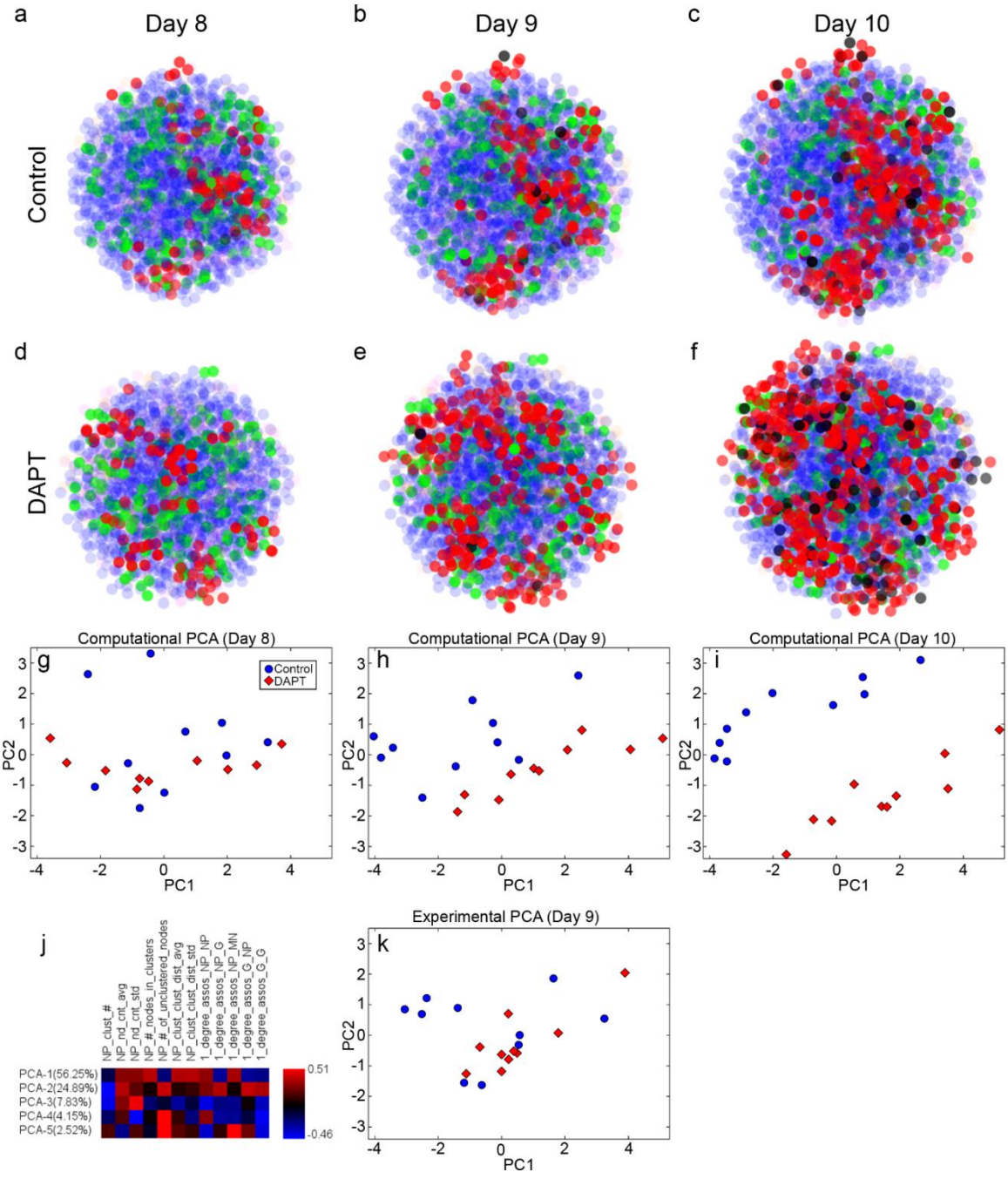
a
Day 8
b
Day 9
c
Day 10
Control
d
e
f
DAPT
Computational PCA (Day 8)
Computational PCA (Day 9)
Computational PCA (Day 10)
g
h
i
Control
DAPT
PC1
PC2
j
NP_clust_#
NP_nd_cnt_avg
NP_nd_cnt_std
NP_#_nodes_in_clusters
NP_#_of_unclustered_nodes
NP_clust_clust_dist_avg
NP_clust_clust_dist_std
1_degree_assos_NP_NP
1_degree_assos_NP_G
1_degree_assos_NP_MN
1_degree_assos_G_NP
1_degree_assos_G_G
PCA-1(56.25%)
PCA-2(24.89%)
PCA-3(7.83%)
PCA-4(4.15%)
PCA-5(2.52%)
0.51
-0.46
Experimental PCA (Day 9)
k

Supplementary Figure 3.1. Computational data for Feedback/Transient differentiation scheme. Simulated quantities of unlabeled cells (blue), stable pMN (red), transient pMN (orange), MN (green) and OPC (cyan) (n=10). Shaded region represents +/- 1 standard deviation of simulations.

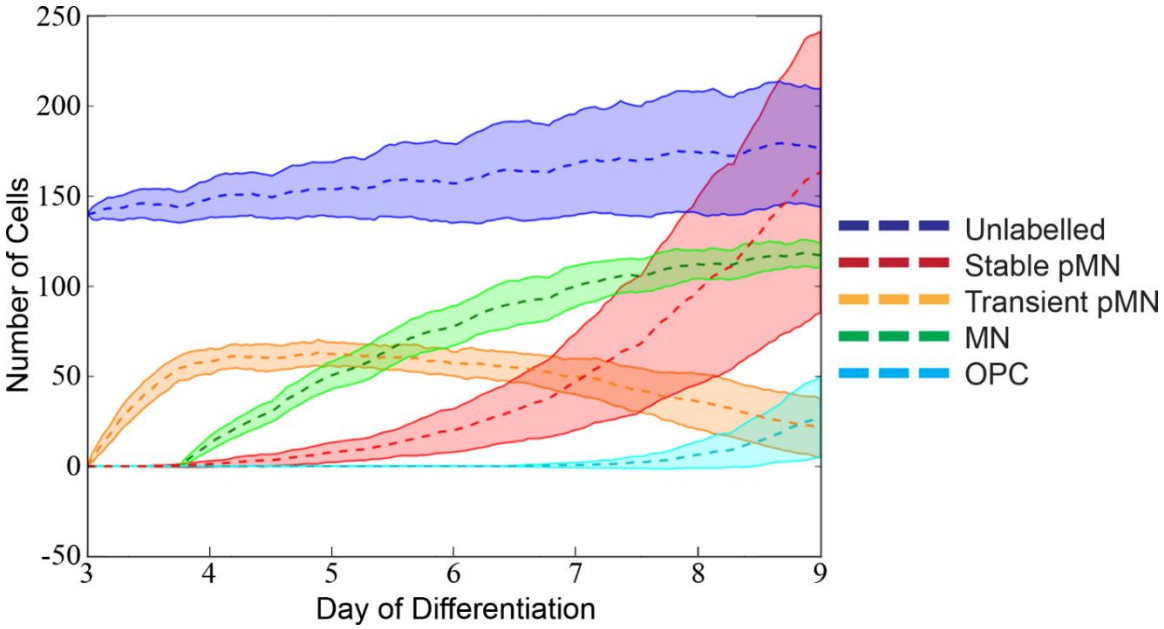
250
200
150
100
50
0
-50
Number of Cells
3
4
5
6
7
8
9
Day of Differentiation
Unlabelled
Stable pMN
Transient pMN
MN
OPC

Supplemental Figure 3.2. Modeling suggests that DAPT-treatment indirectly increases differentiated cell quantities.

(a) Maximum projection images of control (a, a”’) and DAPT-treated (a’, a””) aggregates. (a, a’) Hoechst, Olig2 and GFP immunostaining shows increases in MN on day 5 in treated aggregates. (a”’, a””) Olig2 and Nkx2.2 immunostaining show increases in OPC at day 9 in treated aggregates. Scale bar represents 50 μm (b) Cell quantities of untreated and DAPT-treated MN in aggregates on day 5 after day 3 DAPT-treatment (left side). Cell quantities of untreated and DAPT-treated OPC in aggregates on day 9 after day 7 DAPT-treatment (right side). Center line represent median. Two-tailed t-test, $*P=0.008$, $**P<0.001$. (c, j) Schematics for differentiation schemes modeled. (c) DAPT directly increases transition from transient pMN and stable pMN towards MN. (j) DAPT directly increases transition from stable pMN towards OPC. Plots depict average simulated (n = 10) and experimental (n = 10 per time point) cell quantities over time. Plots depict experimental data (solid lines), and average simulated data (dashed lines) +/- 1 standard deviation (shaded area). Error bars for experimental data represent standard deviation. (d-f, k-m) DAPT treatment beginning on Day 3. (g-i, n-p) DAPT treatment beginning on day 7. (d, g, k, n) Stable pMN, (e, h, l, o) MN and (f, i, m, p) OPC trajectories are depicted for each schematic.

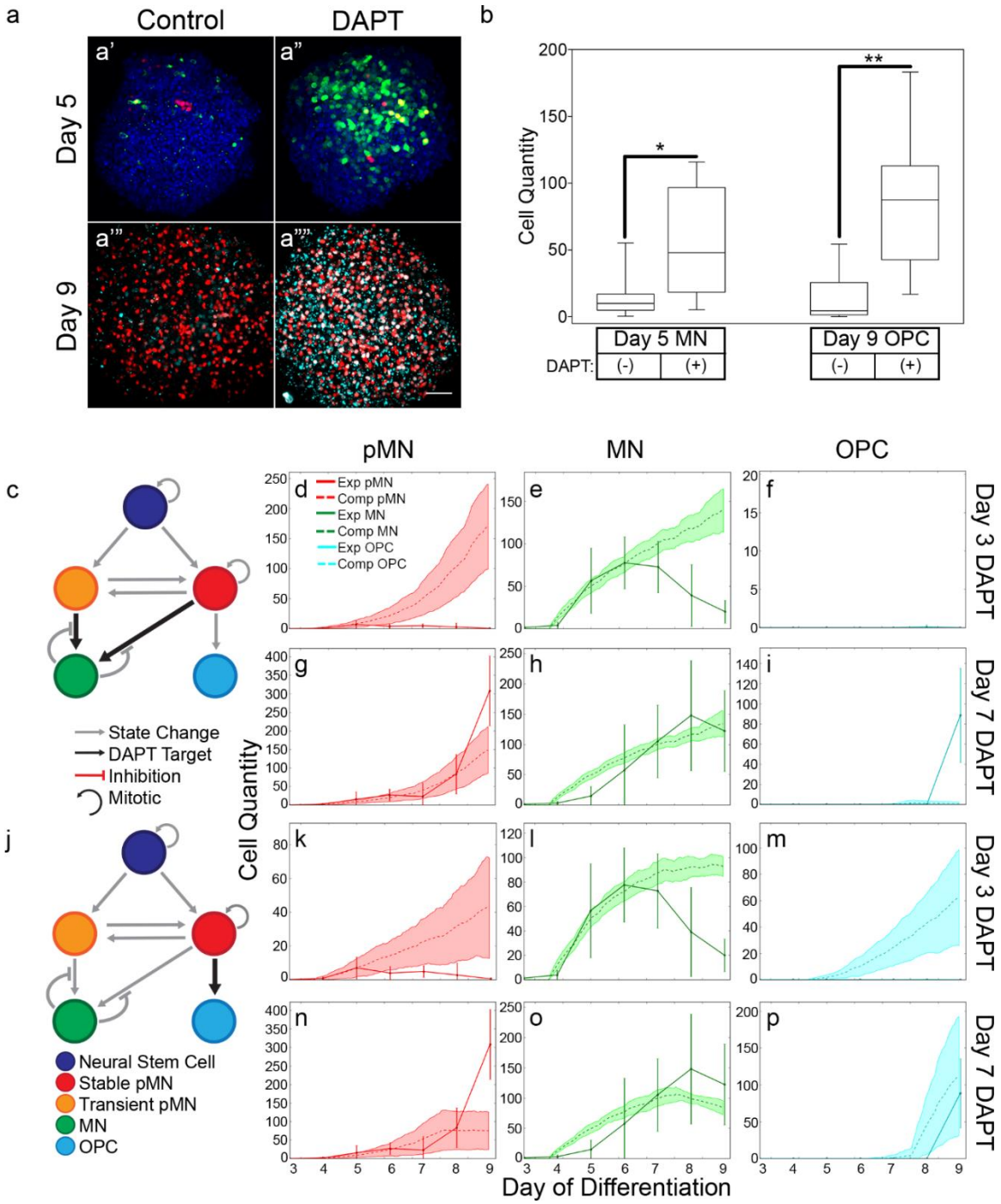
a
Control
DAPT
a'
a''
a'''
a''''
Day 5
Day 9
b
Cell Quantity
200
150
100
50
0
*
**
Day 5 MN
Day 9 OPC
DAPT:
(-)
(+)
(-)
(+)
c
State Change
DAPT Target
Inhibition
Mitotic
j
Neural Stem Cell
Stable pMN
Transient pMN
MN
OPC
pMN
MN
OPC
d
e
f
g
h
i
k
l
m
n
o
p
Exp pMN
Comp pMN
Exp MN
Comp MN
Exp OPC
Comp OPC
Cell Quantity
Day 3 DAPT
Day 7 DAPT
Day 3 DAPT
Day 7 DAPT
3 4 5 6 7 8 9
Day of Differentiation

Supplementary Table 3.1. Two Way ANOVA table for Tgf-β experiments.

Top. Two-Way ANOVA with Holm-Sidak multiple comparisons results for Fig. 3.6b.

Bottom. Two-Way ANOVA with Holm-Sidak comparisons for Fig. 3.6c, d.

	GFP+	Total Olig2	Total Nkx2.2	Olig2+/ Nkx2.2-	Olig2-/ Nkx2.2+	Olig2+/ Nkx2.2+
SB/TGF	0.037	0.020	0.842	0.008	0.009	0.071
DMSO/DAPT	0.621	0.122	0.025	0.067	0.011	0.261
SB/TGF x DMSO/DAPT	0.717	0.139	0.969	0.126	0.096	0.213
DMSO/DAPT within SB	0.547	0.953	0.091	0.779	0.006	Not tested
DMSO/DAPT within TGF	0.925	0.044	0.084	0.027	0.347	
SB/TGF within DMSO	0.173	0.396	0.866	0.24	0.317	
SB/TGF within DAPT	0.077	0.012	0.91	0.006	0.006	

	Nkx2.2- within Olig2+	Nkx2.2+ within Olig2	Olig2- within Nkx2.2+	Olig2+ within Nkx2.2+
SB/TGF	0.503	0.503	0.006	0.045
DMSO/DAPT	0.841	0.841	0.243	0.442
SB/TGF x DMSO/DAPT	0.596	0.596	0.229	0.428
DMSO/DAPT within SB	Not tested	Not tested	0.107	0.278
DMSO/DAPT within TGF			0.978	0.986
SB/TGF within DMSO			0.128	0.308
SB/TGF within DAPT			0.008	0.053

CHAPTER 4

THE CONVERGENCE OF THE NOTCH, TGF-BETA AND SONIC HEDGEHOG SIGNALING PATHWAYS IN PMN DERIVATION AND DIFFERENTIATION[1]

[1]Swetenburg, R. L. and S.L. Stice. To be submitted to *Stem Cells and Development*.

Abstract

In the primitive spinal cord, termed the neural tube, a gradient of Sonic hedgehog (Shh) generates distinct progenitor domains which will ultimately give rise to the motor control system in the adult. The pMN and p3 domain express the transcription factors Olig2 and Nkx2.2, respectively. Both domains derive from Olig2-expressing cells at the onset of Shh patterning. Ultimately, pMN and p3 cells become oligodendrocyte precursor cells (OPC), which is, in part, marked by a switch from cross-repression to co-expression of Olig2 and Nkx2.2. Previously, we showed that Notch signaling inhibition in early stage pluripotent stem cell cultures downregulated Olig2 expression, while in late differentiation, Notch inhibition appeared to increase Olig2. In addition to Notch signaling, Shh and transforming growth factor-β (Tgf-β) have also been linked to gliogenesis and thus the regulation of Olig2. Our overall goal was to examine the interplay of Shh, Notch-Delta and Tgf-β within the context of PSC differentiation towards the pMN, p3 and OPC fate. We find that an unexpected combination of Notch inhibition and Tgf-β pathway activation stabilizes the pMN cell state by a post-transcriptional mechanism. Moreover, this stabilization is sufficient to decrease Shh-driven Nkx2.2 expression in both OPC and p3 cell types.

Introduction

The ventral neural tube is the birthplace of all major neural cell types of the motor control system, which is ultimately responsible for controlling all voluntary and involuntary movement in the body. A gradient of Sonic Hedgehog (Shh) from the notochord and, later, the floor plate, specifies five distinct progenitor domains: p0, p1, p2, pMN and p3 [1-3]. Ventral most, and thus exposed to the highest levels of Shh, are the

p3 and pMN domains. Expression of the basic helix-loop-helix (bHLH) transcription factor oligodendrocyte transcription factor 2 (Olig2) defines the pMN domain, while the homeodomain transcription factor NK2 Homeobox 2 (Nkx2.2) marks the p3 domain.

Modeling of the corresponding gene regulatory network [4], as well a fate mapping experiments [5], have established that the Olig2 protein is expressed in the precursor cells of both the future pMN and p3 domain in the ventral neural tube (Fig. 4.1). Cells further displaced from Shh sources (i.e. more dorsal) remain $Olig2^+$ by modulating their response to Shh, effectively blunting its effect, to establish the pMN domain [4, 6]. The more ventral $Olig2^+$ cells experience increased Shh levels which drives the expression of the Olig2-repressive Nkx2.2 protein, thereby establishing the p3 domain. After the p3 and pMN domains are established, both progenitor cells generate neurons by asymmetric division in a self-renewing manner [7], including motor neurons (MN) and V3 interneurons, respectively. Later in development, Olig2 and Nkx2.2 shift from being cross-repressive to being co-expressed within oligodendrocyte progenitor cells (OPC) [8]. OPC derive from both pMN (i.e. expression of Nkx2.2 in $Olig2^+$ cells) and the p3 domain (i.e. expression of Olig2 in $Nkx2.2^+$ cells), and both transcription factors work cooperatively to drive much of the genetic machinery for myelination in oligodendrocytes [9].

The Notch-Delta pathway is a juxtacrine signaling mechanism activated by direct cell-cell contact between one of four membrane-spanning Notch receptors, Notch1-4, and a Notch ligand, including the Delta and Jagged family members (reviewed in [10]). Upon activation, a number of proteolytic cleavages, including an obligate γ-secretase cleavage, releases the Notch intracellular domain (NICD) from the membrane to

translocate directly to the nucleus. There, it drives the transcription of Notch target genes, including the hairy and enhancer of split (Hes) and the hairy/enhancer-of-split related with YRPW motif protein (Hey) family members. Notch signaling is critical to the proper regulation of neurogenesis and gliogenesis in the developing central nervous system, including the caudal ventral neural tube [11]. Notch and Notch ligands are highly expressed in the ventricular zone during neurogenesis, but appear in a salt-and-pepper pattern later in development, during gliogenesis and OPC specification [12]. When Notch-Delta signaling is inhibited behind an $Olig2^{+}$ promoter, such that only cells already expressing Olig2 experience depleted Notch, the pMN domain is expanded by essentially desensitizing the cells to Shh signaling, effectively lowering the Shh dose each cell experiences. This dampens the effects of high Shh, resulting in reduced Nkx.2 expression, which, in turn, does not suppress Olig2. Together, this leads to pMN expansion [13]. NICD overexpression results in OPC formation and decreased neurogenesis, indicating that Notch oscillations are essential for asymmetric divisions within pMN [14]. On the other hand, Notch inhibition after the pMN domain is established greatly accelerates the transition from pMN to MN at the expense of progenitors [15]. Late Notch inhibition, however, yields increased OPC [12]. The Notch-Olig2 interaction is particularly puzzling as, early in development, Notch inhibition increases Olig2 levels by essentially decreasing Nkx2.2 levels through Shh modulation. Later, Notch inhibition drives pMN to become to become $Olig2^{-}$ MN. During gliogenesis, Notch inhibition generates OPC both prematurely and in excess, which would require the maintenance of Olig2, in line with the pMN expansion effect but in direct opposition to MN generation.

Notably, the transforming growth factor-β (Tgf-β) pathway is upregulated around the time of gliogenesis, when Notch signaling takes on the salt-and-pepper pattern [12, 16]. Moreover, Tgf-β, but not bone morphogenetic protein (BMP), can bypass neurogenesis in pMN and induce gliogenesis [17]. There is ample evidence of crosstalk between Shh, Notch-Delta and Tgf-β (reviewed in [18]). As noted, the long terms effects of Notch inhibition are well studied. Our overall aim was to gain a better understanding of how Notch inhibition affects the $Olig2^+$ cell-based differentiation trajectory towards pMN, p3 and OPC in the short term, and how two critical signaling pathways, Shh and Tgf-β, might depress or enhance these effects. Here, we present evidence that the specific combination of Tgf-β pathway activation and Notch inhibition strongly stabilizes the expression of the Olig2 protein, regardless of Shh activation or inhibition, through a post-transcriptional mechanism. Not only are pMN increased, but both p3 and OPC are decreased. In all, our studies reveal a delicately balanced interplay between all three pathways in the derivation and differentiation of pMN towards both p3 and OPC.

Results

To investigate the effects of Notch inhibition on Olig2 expression, we used the γ-secretase inhibitor DAPT, an inhibitor of the Notch signaling cascade in neural development [19]. Pluripotent stem cell (PSC) cultures were differentiated to a point where pMN levels plateau at a low level yet MN are increasing [20], and exposed to either DAPT or DMSO for 24 hours (Fig. 4.2A). We combined an Olig2::GFP reporter cell line [21] with immunocytochemistry (ICC) to differentiate between Olig2 mRNA expression and Olig2 protein expression, respectively (Fig. 4.2B,C). The GFP^+ cell fraction largely remained the same with a slight decrease at 24 hours (Fig. 4.2B). $Olig2^+$

cells, as defined by ICC, and the ratio of ICC/GFP$^+$, however, significantly declined between the 12 and 24 hour time points (Fig. 4.2B,C). Therefore, Notch inhibition had minimal effects on Olig2 transcription, but significantly reduced the number of cells expressing the Olig2 protein.

In later development, Olig2 levels are sustained in response to Notch inhibition. Thus, we hypothesized that the presence or absence of either Tgf-β or Shh in cultures would effectively block the effects of DAPT on pMN observed in Figure 4.2. Cultures were exposed to combinations of Tgf-β2, the Tgf-β inhibitor, SB431542 [22] (SB), the Smoothened agonist purmorphamine (Pur) and/or the Shh inhibitor cyclopamine [23] (Cyc) (Fig. 4.3A), followed by 24 hours of DAPT or vehicle (DMSO) treatment. Cells were analyzed by flow cytometry for Olig2 and Nkx2.2 by ICC, and for Olig2 transcription by GFP expression. Overall marker expression followed similar trends, with Pur increasing all cell types of interest over Cyc. Notably, Tgf-β decreased the overall number of GFP$^+$ cells. DAPT had no significant effect on overall marker expression within the 24 hours treatment period. Therefore, all markers increased in response to exogenous Shh signaling, while Tgf-β decreased the number of cell transcribing Olig2.

We next investigated the effects of Tgf-β, Shh and DAPT on individual cell types as denoted by traditional protein markers. pMN (Olig2$^+$/Nkx2.2$^-$/GFP$^{+/-}$) were increased in Pur over Cyc while Tgf-β/SB had a significant interaction with DMSO/DAPT (Fig. 4.3C). Increases in pMN in Tgf-β/DAPT both within DMSO/DAPT and within Tgf-β/SB neared significance. It is worth noting that only an exceptionally small population of cells expressed Olig2 in the absence of both GFP and Nkx2.2, indicating that Olig2

protein expression was wholly dependent upon Olig2 transcription. On the contrary, there were a substantial number of cells co-expressing Olig2 and Nkx2.2 which were GFP^- (data not shown), indicating that Olig2 protein expression can be propagated in the absence of transcription in more OPC-like cell types. OPC ($Olig2^+/Nkx2.2^+/GFP^{+/-}$) cells were increased in both SB and Pur (Fig. 4.3C). The p3 cell population ($Olig2^-/Nkx2.2^+/GFP^{+/-}$) was increased in Pur over Cyc with a Tgf-β/SB interaction effect with Pur/Cyc that neared significance (Fig. 4.3C). In all, the data show that Pur increased all cell types of interest, while Tgf-β and Notch may differentially affect pMN.

A cell type unique to this study was the $Olig2^-/Nkx2.2^-/GFP^+$ (GFP^+) population. GFP^+ cells were negatively regulated by DAPT while Tgf-β/SB showed a significant interaction with Pur/Cyc. Pur increased the GFP^+ population within both Tgf-β and SB conditions, while SB increased GFP^+ over Tgf-β in Pur conditions, likely due to the a decrease in Olig2 transcription by Tgf-β. Notably, within Tgf-β^+ conditions, GFP^+ cells appear to follow the opposite trend as the pMN cells. To better examine this relationship, we normalized the pMN population to the GFP^+ population within each treatment (Fig. 4.3D). Tgf-β/SB statistically interacted with both the Pur/Cyc and the DMSO/DAPT treatments: within Tgf-β conditions, Cyc increased the GFP^+:pMN ratio over Pur. Notably, there appeared to be an inverse relationship in how Notch inhibition affected Tgf-β and SB treated cultures: Tgf-β/DAPT treatment shifted the ratio towards Olig2 protein expression, while SB/DAPT shifted the ratio towards GFP^+ only. Thus, even though Tgf-β deceases Olig2 expression, it appears to have a stabilizing on the Olig2 protein.

Fate mapping and gene regulatory network studies *in vivo* have shown that Olig2-expessing cells in the ventral neural tube are the source of both pMN and p3 progenitors [4, 6]. Moreover, $Olig2^+/Nkx2.2^+$ OPC derive from both populations [9] (Fig. 4.1). In other words, either pMN progenitors can gain Nkx2.2 expression or p3 progenitors can gain Olig2, during the generation of OPC. *In vivo*, every cell expressing Olig2 eventually expresses Nkx2.2 and vice versa. Based on the literature and our previous data, we conceptualized a differentiation progression based on the four major populations we identified (GFP^+, pMN, p3, OPC) with the following assumptions: (1) GFP expression is obligate prior to Olig2 protein identification, (2) pMN are the source of both p3 and OPC, (3) Nkx2.2 is a dominant repressor (i.e. Nkx2.2 cannot be downregulated), (4) all cells of interest progress towards the OPC fate in a stepwise manner (i.e. cells cannot regress, dedifferentiate) and (5) our data represent a "snapshot" of differentiation, comprised of cells at different stages in the overall progression. Thus we generated a model for differentiation (Fig. 4.4A) in which an uncommitted cell first expressed Olig2 mRNA, followed by concurrent Olig2 protein expression. All p3 cells derived from $Olig2^+$ progenitors, while both p3 and pMN could generate OPC. To account for different overall effects on marker expression, each stepwise progression was calculated as a ratio of the descendent to its predecessor and then normalized to SB/Cyc/DAPT (in which each pathway is inhibited) to determine the effect of adding each pathway back individually or in combination. We derived ratios for pMN to GFP, p3 to pMN, OPC to p3 and OPC to pMN to investigate each cell state transition.

We first examined the pMN/GFP^+ ratio as a measure of which conditions promote Olig2 protein expression in cells transcribing Olig2. Only the combination of Tgf-β and

DAPT were sufficient to significantly increase pMN over the total inhibition group (Fig. 4.4B). Shh appeared to have an additive effect to Tgf-β/DAPT. Notch restoration alone, or Notch and Shh combined, both had a similar effect. However, Shh in combination with Tgf-β and DMSO did not significantly increase over control. No treatment significantly promoted p3 over pMN, though Tgf-β addition and Notch restoration approached significance (Fig. 4.4B). The OPC-to-pMN ratio was decreased by all groups except the restoration of Notch signaling alone, or the combination of Tgf-β and Notch. Notably, Tgf-β did not have the same effect on the OPC to p3 ratio, as only Notch restoration was insignificant from complete inhibition. The data imply that Tgf-β in combination with Notch inhibition strongly favors both the acquisition of, and impedes the differentiation from, the pMN state.

That most treatments reduced the OPC levels compared to their predecessors indicates the Shh, Tgf-β and Notch all likely contribute to the maintenance and stability of progenitor cells (p3 and pMN) over OPC differentiation. Notch restoration alone was sufficient to rescue the ratio of OPC to either pMN or p3. However, OPC:pMN, but not OPC:p3, included the Tgf-β/Notch restoration treatment which brought it to levels near those of complete inhibition, possibly due to Olig2 transcription disruption by Tgf-β. Taken together, our data imply that the p3 or pMN cell types must by weakly destabilized in order for either become an OPC (see Discussion).

As Shh is required for OPC specification *in vivo*, we asked how varying the dosage of Pur might affect our system. To isolate the interactions of the Shh and Notch pathways, we treated cultures with Pur in the presence and absence of DAPT in cultures under persistent Tgf-β inhibition (Fig. 4.5A). Pur concentrations over 10 μM were

largely cytotoxic (data not shown). Total Olig2 was increased in the absence of Pur and decreased at higher levels, though no significant effect of DAPT was observed (Fig. 4.5B). Total Nkx2.2 followed a somewhat inverse pattern: decreasing Shh signaling significantly decreased total Nkx2.2 levels (Fig. 4.5C). However, above 1 μM, there was no significant change in Nkx2.2, indicating that the population had plateaued. Taken together, this is consistent with developmental studies, in that higher Shh concentrations favor Nkx2.2 over Olig2 expression. Within the total GFP^+ population, higher doses largely followed the same pattern as total Olig2 (Fig. 4.5D). However, there was no increase over 1 μM in the absence of Pur. Therefore, the relationship between Olig2 transcription and protein expression was largely dependent on the level of Shh signaling.

The pMN and OPC cell populations were regulated in a similar manner to total Olig2, in that decreasing Pur from 1 to 0 μM generated a significant increase in these cell types, but increased Pur led to decreased populations (Fig. 4.5E,F). p3 cells mimicked total Nkx2.2, as well (Fig. 4.5G). Cells positive for Olig2 transcription but neither the Olig2 or Nkx2.2 protein expression (GFP^+) were regulated by both Pur dosage and DAPT (Fig. 4.5H). DMSO increased Olig2 transcription overall and within the 1 μM Pur dose. Within DMSO, only 2.5 and 5 μM doses were significantly different from 1, while in DAPT 0 μM was increased over 1, and 2.5 and 5 μM were decreased. Taken together, Pur doses significantly affected the expression of Olig2 and Nkx2.2 proteins, as well as Olig2 transcription. However, only Olig2 transcription was differentially regulated by DAPT, implying the Shh cannot rescue the effects of DAPT on Olig2 protein, and thus identifying Tgf-β as a more likely candidate for Olig2 protein stabilization.

To investigate the isolated effects of Tgf-β we quantified both Olig2 mRNA and total protein by RT-qPCR and western blot, respectively, in cultures treated with Cyc (Fig. 4.6A). In terms of total Olig2 protein, within Tgf-β cultures, protein increases neared significance, while within SB there was a significant decrease. Within DMSO, Tgf-β decreased the amount of Olig2 protein while in DAPT, Tgf-β increased the amount of Olig2 (Fig. 4.6B). No significant effect on Olig2 mRNA levels was found either from DAPT or Tgf-β treatments (Fig. 4.6C). Therefore, Tgf-β and DAPT treatments did not change the overall amount of Olig2 mRNA, but differentially modulated the amount of protein in an inverse manner.

Discussion

We were initially motivated to investigate Olig2 regulation by detecting a non-linear relationship between Olig2 protein expression and transcription in the presence of the Notch inhibitor DAPT during the MN generation phase of differentiation, which included a slight increase in Olig2 transcription over DMSO, followed by a sharp decline in Olig2-protein expressing cells within 24 hours of DAPT addition (Fig. 4.2). We asked how DAPT might maintain or increase the number of cells transcribing Olig2, only to then decrease the number of cells expressing Olig2 protein. We hypothesized that some combination of Tgf-β and Shh pathway modulation would either progress cultures towards a more OPC-like state, in which Notch inhibition increases the overall Olig2 protein-expressing cells, or retain them in a state in which Notch inhibition reduces Olig2 protein, as has been shown during neurogenesis.

Our studies indicate a complex relationship between the Tgf-β, Notch-Delta and Shh signaling pathways in the specification of pMN, p3 and OPC cell types. Shh

signaling generally promoted all cell types of interest. However, increasing Shh signaling drastically decreased Olig2^{+} cells in favor of Nkx2.2^{+} cells, even when the number of cells transcribing Olig2 remained unchanged. Tgf-β reduced the overall number of cells transcribing Olig2, but not the overall amount of Olig2 mRNA. As expected, Notch inhibition via DAPT did not affect overall Olig2, Nkx2.2 or GFP expression. However, in tandem with Tgf-β, DAPT appeared to stabilize the pMN cell state by increasing the amount of Olig2 protein, or possibly be preventing its loss. In the absence of Tgf-β signaling, DAPT reduced the overall amount of Olig2 protein. In the presence of endogenous Notch signaling, Tgf-β actually promotes the p3 cell state over pMN.

Taken together, we hypothesize that Shh signaling increases pMN levels overall by driving the initial transcription of Olig2, but also increases the flux from pMN to p3 by driving the Olig2-repressive Nkx2.2.. Tgf-β reduces Olig2 transcription and thus the source of all downstream cell types, but also has a strong stabilizing effect on Olig2 protein expression in combination DAPT to promote pMN populations. Endogenous Notch alone weakly stabilizes the Olig2 protein, and the pMN state. DAPT in the absence of Tgf-β destabilizes Olig2 protein expression. However, Tgf-β and DAPT can combine to stabilize Olig2, preventing Nkx2.2 from downregulating it to generate p3. Finally, during OPC specification, increased Shh signaling prevents p3 cells from gaining Olig2 expression and becoming OPC. Meanwhile, in pMN stabilized by Tgf-β/DAPT, Olig2 continues to repress Nkx2.2, thus preventing OPC formation from pMN. This implies that OPC derived from p3 cells likely need Shh inhibited for Olig2 co-expression, but with an Olig2-stabilizing component (e.g. Olig2 stabilized by Notch and a lack of

Tgf-β). Conversely, Tgf-β/DAPT combinations stabilize Olig2 such that p3 and OPC generation is inhibited.

It is useful to look at these hypotheses in context by examining various scenarios from Figure 4.3. In the pMN/GFP$^+$ ratio, Tgf-β/DAPT treatments had the highest mean with an additive effect seen in Shh-activated cultures. Based on our hypotheses, this was likely due to the effect of Tgf-β/DAPT stabilization of Olig2 protein expression, with or without Shh signaling continuing to drive transcription. The lowest mean occurred in Cyc/Tgf-β/DMSO: though endogenous Notch would likely have stabilized Olig2 protein expression, Tgf-β and inhibition of the Shh pathway jointly decreased the transcription levels. This effect can be partially rescued by Shh pathway activation. The restoration of endogenous Notch signaling alone also increased the mean over complete inhibition, similar to results in Figure 4.2.

In the p3/pMN ratio, each of the three lowest means involved stabilized Olig2 protein, either through Tgf-β/DAPT or endogenous Notch. When Shh signaling was added to these combinations, it was able to counteract endogenous Notch signaling to generate p3. However, Tgf-β/DAPT maintained the pMN population in either the presence or absence of Pur, indicating that Tgf-β/DAPT stabilization of Olig2, but not endogenous Notch signaling, superseded exogenous Shh activation to prevent p3 generation. Both Pur/SB/DAPT and, surprisingly, Cyc/Tgf-β/DMSO yielded similar results in pushing cells from a pMN towards a p3 state. We expect that the added Shh pathway activation by Pur, the "normal" Olig2 transcription afforded by SB, and the destabilizing nature of DAPT on the Olig2 protein, might explain this increase in p3 generation in the former case. In the case of the latter, even though endogenous Notch

stabilized Olig2 protein, Tgf-β likely disrupted Olig2 transcription enough that p3 transitions occurred even in the absence of Shh pathway activation.

In order to generate OPC, either a p3 cell must begin expressing Olig2, or a pMN cell must begin to express Nkx2.2. The lowest means for OPC:pMN came from the Tgf-β/DAPT treated cells in the presence or absence of Pur, further strengthening our hypothesis that stabilized Olig2 suppressed Nkx2.2. The highest ratios came from cultures with destabilized Olig2 transcription (Tgf-β^{+}/DAPT^{-}) in the absence of Pur, such that Nkx2.2 suppressed Olig2 expression. For OPC/p3 ratios, Pur/DAPT in the absence of Tgf-β yielded the lowest ratio likely due to high Shh driving Nkx2.2 while DAPT destabilized Olig2 protein. The highest ratio of OPC to p3, however, was Cyc/SB/DMSO, with a positive mean, in which Shh pathway inhibition likely led to low levels of Nkx2.2, SB allowed for upregulated Olig2 transcription and endogenous Notch further stabilized the Olig2 protein. Importantly, no conditions generated OPC significantly better than complete inhibition, indicating that a there is a very delicate balance of these signals that must be met for the successful generation of OPC.

The push and pull on each cell type, and between each pathway, is striking. Tgf-β decreases the overall number of cells transcribing Olig2, but can rescue the effects of Notch inhibition in terms of protein expression. In order to increase the ratio of p3 to pMN, it is necessary to destabilize Olig2, either transcriptionally through Tgf-β addition in the presence of Notch, or post-transcriptionally through DAPT addition during Tgf-β inhibition. Each of these signals is detrimental to OPC generation, both alone and in combination- likely due to stabilized Olig2 suppressing Nkx2.2, and p3-stabilizing conditions depressing Olig2 transcription.

These studies, it should be noted, investigated the sequential treatment of cultures: first by modulating the Shh and/or Tgf-β pathways, and only then by modulating the Notch pathway in otherwise untreated cultures and only for 24 hours. This is an important distinction, as many of the cells types were generated during the two day Tgf-β/Shh treatments, and not concurrently with Notch modulation. Further, we expect that many cells express Tgf-β, as seen *in vivo* [16], which can effect cells upon removal of SB during DAPT administration leading to an incomplete rescue of the DAPT phenotype in Figure 4.2.

However, the DAPT-induced changes seen in the overall populations between matching Tgf-β and Shh treatments is evidence of the profound effect Notch inhibition can have on cell types in a short amount of time. In Figure 4.2, we show that DAPT negatively regulates the Olig2 protein without affecting its transcription. In Figure 4.3, we show that Tgf-β downregulates Olig2 transcription. The model proposed in Figure 4.4 is simplified, as both pMN and p3 generate neuronal and astrgolial subtypes not studied here. Moreover, we have previously shown that it is likely that GFP+/Olig2^{-} are a potential source of MN. Taken together, we propose a parallel effect of Tgf-β signaling, in which DAPT suppresses Nkx2.2 expression and Tgf-β prevents MN generation, both of which would results in increased pMN and have been demonstrated separately *in vivo* [13, 17]. In all, we have demonstrated, for the first time, crosstalk between the Tgf-β, Shh and Notch signaling pathways in the specification of Olig2-expressing cell types and their derivatives. Though the effect of long term Notch inhibition is well documented, this is a first step in understanding the mechanisms

underlying those changes which will ultimately enhance developmental and disease models, as well as *in vitro* PSC differentiation.

Methods

Cell maintenance and differentiation

The G-Olig2 mESC line [21] from was used for all experiments. ES cells were maintained as previously described [24]. Briefly, mitomycin C-inactivated mouse embryonic fibroblasts (MEF) were plated at 50,000 cells/cm2 for 24-48 hours in media consisting of DMEM with 4500 mg/L Glucose (HyClone Laboratories), supplemented with Defined FBS (10%, HyClone Laboratories), Penicillin/Streptomycin (50 U/ml, ThermoFisher) and L-Glutamine (4 mM, ThermoFisher). G-Olig2 mESCs were plated on inactivated MEFs in ESC medium consisting of EmbryoMax DMEM with 4500 mg/L glucose and 2250 mg/L $NaHCO_3$ (Milllipore), Non-Essential Amino Acids (1x, ThermoFisher), Nucleosides (1x, Millipore), L-Glutamine (2 mM, ThermoFisher), Penicillin/Streptomycin (50 U/ml, ThermoFisher), Defined FBS (15%, HyClone Laboratories), Beta-mercaptoethanol (100 nM, Sigma) and murine LIF (1000 U/ml, Millipore). Cells were between passage 15 and 19 for all experiments. Cells were expanded and frozen in ESC medium supplemented with 10% DMSO until use.

ES cell differentiation

G-Olig2 were differentiated as described [24], with minor adjustments. Briefly, G-Olig2 mESCs were thawed (day 0) directly into differentiation medium consisting of a 1:1 mixture of AB2 (Aruna Biomedical) and Advanced DMEM/F12 (ThermoFisher) supplemented with Knockout Serum Replacement (10%, ThermoFisher), L-Glutamine (2 mM, ThermoFisher), Penicillin/Streptomycin (50 U/ml, ThermoFisher), and Beta-

mercaptoethanol (100 nM, Sigma). Thawed cells were seeded into 10 cm petri dishes in where they self-aggregated, and were maintained in rotary culture on an Orbi-shaker Jr. (Benchmark Scientific) at 50 rpm. Cells were maintained in basal differentiation medium for 72 hours post-thaw with daily media changes (days 1-3). At 48 and 72 hours post-thaw, media was supplemented with retinoic acid (RA, 1 μM) and Purmorphamine (Pur, 1 μM). At day 5, aggregates were dissociated using 0.05% Trypsin (ThermoFisher) for 6 minutes with trituration at 3 minutes. Trypsin was quenched with an equal volume of 20% FBS in DMEM/F12 (ThermoFisher), followed by another trituration post-quench. Dissociated cells were passed through a 70 μm cell strainer (Corning), quantified and replated into differentiation media supplemented with Rock inhibitor (10 μM, Fisher Scientific) and containing mixes of Pur (Fisher Scientific), Cyc (10 μM, Selleck Chemicals), SB431542 (10 μM, Sigma Aldrich), Tgf-β2 (10 ng/ml, EMD Millipore), N-[N-(3,5-Difluorophenacetyl)-L-alanyl]-S-phenylglycine t-butyl ester (DAPT, 5 μM, Sigma Aldrich) and Dimethyl Sulfoxide (DMSO, Fisher Scientific) into plates or slides pre-coated with Growth Factor Reduced Matrigel (BD Bioscience) for one hour.

Immunocytochemistry

Immunocytochemistry was performed on intact embryoid bodies (EB) as described[25], with minor modifications. Briefly, cultures were fixed in 4% paraformaldehyde (PFA, Electron Microscopy Sciences). Cells were then permeabilized for 15 minutes in 0.1% Triton X-100 in phosphate buffered saline with calcium and magnesium ($PBS^{+/+}$, HyClone). Cells were blocked in blocking buffer (2% bovine serum albumin, 0.1% Tween-20 in $PBS^{+/+}$) for 45-60 minutes. Samples were immunolabelled with rabbit anti-Olig2 (1:2000, EMD Millipore) and mouse anti-Nkx2.2 (1:200,

Developmental Hybridoma Studies Bank) antibody for 1 hour at room temperature in blocking buffer. After three five-minute washes in blocking buffer, cells were subsequently stained with a secondary anti-rabbit Alexa Fluor 546 and anti-mouse Alexa Fluor 647 secondary antibodies (both 1:1000, ThermoFisher) for 1 hours. Samples were washed 3 more times for five minutes each and coverslipped with DAPI Prolong Gold reagent (Life Technologies). Cell type numbers were quantified with a custom ImageJ algorithm.

Flow Cytometry

For flow cytometry, cells were differentiated as above. At day five, cells were dissociated to 60 mm, Matrigel coated plates in differentiation medium supplemented with appropriate mixtures of Tgf-β, SB, Pur or Cyc. After 48 hours, media was changed to that containing either DAPT (5 μM) or an equal volume of DMSO. After 24 hours, cells were dissociated with trypsin, washed once in PBS without magnesium or calcium ($PBS^{-/-}$) and fix in 4% PFA diluted in $PBS^{-/-}$. 10^6 cells were transferred to a V-bottom 96 well plate where all subsequent steps occurred on ice. Cells were permeabilized with 0.1% Triton-X 100 for 15 minutes in $PBS^{-/-}$ and washed twice in $PBS^{-/-}$. Cells were blocked in 1% BSA in $PBS^{-/-}$ (blocking buffer) for one hour. Cells were then incubated with Olig2 (1:500, EMD Millipore) or Nkx2.2 (1:10, DHSB) for 60 minutes in blocking buffer. Cells were washed three time for 5 minutes in blocking buffer and incubated with Alexa Fluor 546 and 633 at 1:2000 for 30 minutes. After three, five minutes washes in blocking buffer, cells were resuspended in $PBS^{-/-}$ for analysis by flow cytometry, including unstained cells and FMO controls for each antibody. Flow cytometry was performed on a Beckman Coulter Cytoflex. Flow cytometry results were analyzed using

the open-source, density- and cluster-based FLOCK package [26] freely available through the National Institute of Allergy and Infectious Diseases (NIAID). Briefly, the workflow was performed as suggested, and consisted of automated quality control on each sample, followed by automatic gating and conversion. All samples were merged and FLOCK analysis was run on the merged dataset. Like populations were auto-collapsed and centroids were determined based on the software algorithm. CrossSample analysis was then run on each dataset individually and final cell fractions were taken from output file. The complete dataset will be published through the NIAID website (Immport.org).

RT-qPCR Analysis

On day 8, after treatment with either Tgf-β2 or SB431542 followed by DAPT or DMSO, RNA was collected using the Qiagen RNEasy Mini Kit per the manufacturer's instructions. RNA and DNA were quantified on a NanoDrop 8000 (ThermoFisher). cDNA was generated using an iScript cDNA Synthesis Kit (BioRad) from 1 μg of RNA on a Biometra Professional ThermoCycler per manufacturer's instructions. qPCR was performed using SsoAdvanced Universal SYBR Green Supermix (BioRad) on a CFX Connect Real-Time System (BioRad). The following primers sequences were obtained from the Harvard PrimerBank database [27]: Olig2 forward: GGGAGGTCATGCCTTACGC, Olig2 reverse: CTCCAGCGAGTTGGTGAGC; Canx forward: ATGGAAGGGAAGTGGTTACTGT, Canx reverse: GCTTTGTAGGTGACCTTTGGAG; Hprt forward: TCAGTCAACGGGGGACATAAA, Hprt Reverse: GGGGCTGTACTGCTTAACCAG; Actb forward: GGCTGTATTCCCCTCCATCG, Actb reverse: CCAGTTGGTAACAATGCCATGT;

Tbp forward: AGAACAATCCAGACTAGCAGCA, Tbp reverse: GGGAACTTCACATCACAGCTC; Gapdh forward: AGGTCGGTGTGAACGGATTTG, Gapdh reverse: TGTAGACCATGTAGTTGAGGTCA. NormFinder software was used to determine the optimal reference genes (Hprt and Canx) based on representative treatments. Olig2, Canx and Hprt efficiencies were 2.06, 1.93, 1.95; and R^2 values were 0.9925, 0.9984, 0.9994, respectively. Melt curve analysis was used to rule out the presence of primer dimers. The Pfaffl method was used to quantify $\log_2$ changes in Olig2 expression versus the average of the reference genes, and then against SB/DMSO treatment.

Western Blotting

Cultures were differentiated and treated as described previously. After treatment, cells were lysed in Pierce IP Lysis Buffer (ThermoFisher) according to manufacturer's instructions supplemented with Halt Protease and Phosphatase Inhibitor Cocktail (1X, ThermoFisher). Pierce BCA Protein assay (ThermoFisher) was used to quantify total protein and plates were read on a Promega GloMax plate reader. 20 μg of protein were mixed with Licor 4x Protein Loading Buffer and incubated at 75° C for 15 minutes. Samples and the Precision Plus Protein All Blue Prestained Protein Ladder (BiorRad) were then loaded into a precast 4-20% Criterion TGX Midi Protein Gel (BioRad) and run in a Criterion Cell (BioRad). Gels were transferred onto nitrocellulose membranes using the Trans-Blot Turbo Transfer System (BioRad) and stained using the iBind Western Device and reagents (ThermoFisher) and the following antibodies and concentrations: Olig2, EMD Millipore, 1:1000; β-Actin, Santa Cruz Biotech, 1:5000; IRDye 800 CW Goat anti-Mouse IgG, Licor, 1:2000; IRDye 800CW anti-Rabbit IgG, Licor, 1:2000.

Membranes were imaged on a BioRad ChemiDoc MP Imaging System and quantified using BioRad ImageLab software package.

References

1. Briscoe, J., et al., *A homeodomain protein code specifies progenitor cell identity and neuronal fate in the ventral neural tube.* Cell, 2000. **101**(4): p. 435-45.
2. Dessaud, E., A.P. McMahon, and J. Briscoe, *Pattern formation in the vertebrate neural tube: a sonic hedgehog morphogen-regulated transcriptional network.* Development, 2008. **135**(15): p. 2489-2503.
3. Jessell, T.M., *Neuronal specification in the spinal cord: inductive signals and transcriptional codes.* Nat Rev Genet, 2000. **1**(1): p. 20-9.
4. Balaskas, N., et al., *Gene Regulatory Logic for Reading the Sonic Hedgehog Signaling Gradient in the Vertebrate Neural Tube.* Cell, 2012. **148**(1-2): p. 273-284.
5. Chen, J.-A., et al., *Mir-17-3p Controls Spinal Neural Progenitor Patterning by Regulating Olig2/Irx3 Cross-Repressive Loop.* Neuron, 2011. **69**(4): p. 721-735.
6. Ribes, V. and J. Briscoe, *Establishing and interpreting graded Sonic Hedgehog signaling during vertebrate neural tube patterning: the role of negative feedback.* Cold Spring Harb Perspect Biol, 2009. **1**(2): p. a002014.
7. Shen, Q., et al., *Asymmetric Numb distribution is critical for asymmetric cell division of mouse cerebral cortical stem cells and neuroblasts.* Development, 2002. **129**(20): p. 4843-53.
8. Sun, T., et al., *Cross-repressive interaction of the Olig2 and Nkx2.2 transcription factors in developing neural tube associated with formation of a specific physical complex.* J Neurosci, 2003. **23**(29): p. 9547-56.
9. Zhou, Q., G. Choi, and D.J. Anderson, *The bHLH transcription factor Olig2 promotes oligodendrocyte differentiation in collaboration with Nkx2.2.* Neuron, 2001. **31**(5): p. 791-807.

10. Kopan, R. and M.X.G. Ilagan, *The Canonical Notch Signaling Pathway: Unfolding the Activation Mechanism.* Cell, 2009. **137**(2): p. 216-233.

11. Louvi, A. and S. Artavanis-Tsakonas, *Notch signalling in vertebrate neural development.* Nat Rev Neurosci, 2006. **7**(2): p. 93-102.

12. Rabadan, M.A., et al., *Jagged2 controls the generation of motor neuron and oligodendrocyte progenitors in the ventral spinal cord.* Cell Death Differ, 2012. **19**(2): p. 209-19.

13. Kong, Jennifer H., et al., *Notch Activity Modulates the Responsiveness of Neural Progenitors to Sonic Hedgehog Signaling.* Developmental Cell, 2015. **33**(4): p. 373-387.

14. Tan, G.C., Esteban O. Mazzoni, and H. Wichterle, *Iterative Role of Notch Signaling in Spinal Motor Neuron Diversification.* Cell Reports, 2016. **16**(4): p. 907-916.

15. Crawford, T.Q. and H. Roelink, *The Notch response inhibitor DAPT enhances neuronal differentiation in embryonic stem cell-derived embryoid bodies independently of sonic hedgehog signaling.* Developmental Dynamics, 2007. **236**(3): p. 886-892.

16. Dutta, D.J., et al., *Combinatorial actions of Tgfbeta and Activin ligands promote oligodendrocyte development and CNS myelination.* Development, 2014. **141**(12): p. 2414-28.

17. Dias, J.M., et al., *Tgfbeta signaling regulates temporal neurogenesis and potency of neural stem cells in the CNS.* Neuron, 2014. **84**(5): p. 927-39.

18. Borggrefe, T., et al., *The Notch intracellular domain integrates signals from Wnt, Hedgehog, TGFβ/BMP and hypoxia pathways.* Biochimica et Biophysica Acta (BBA) - Molecular Cell Research, 2016. **1863**(2): p. 303-313.

19. Geling, A., et al., *A γ-secretase inhibitor blocks Notch signaling in vivo and causes a severe neurogenic phenotype in zebrafish.* EMBO reports, 2002. **3**(7): p. 688-694.

20. Swetenburg, R., White, DE, Kemp, ML, McDevitt, TC, Stice, SS, *In preparation.* 2015.

21. Xian, H.Q., et al., *A subset of ES-cell-derived neural cells marked by gene targeting.* Stem Cells, 2003. **21**(1): p. 41-9.

22. Inman, G.J., et al., *SB-431542 is a potent and specific inhibitor of transforming growth factor-beta superfamily type I activin receptor-like kinase (ALK) receptors ALK4, ALK5, and ALK7.* Mol Pharmacol, 2002. **62**(1): p. 65-74.

23. Cooper, M.K., et al., *Teratogen-mediated inhibition of target tissue response to Shh signaling.* Science, 1998. **280**(5369): p. 1603-7.

24. Wichterle, H., et al., *Directed differentiation of embryonic stem cells into motor neurons.* Cell, 2002. **110**(3): p. 385-97.

25. White, D.E., et al., *Spatial pattern dynamics of 3D stem cell loss of pluripotency via rules-based computational modeling.* PLoS Comput Biol, 2013. **9**(3): p. e1002952.

26. Qian, Y., et al., *Elucidation of seventeen human peripheral blood B-cell subsets and quantification of the tetanus response using a density-based method for the automated identification of cell populations in multidimensional flow cytometry data.* Cytometry B Clin Cytom, 2010. **78 Suppl 1**: p. S69-82.

27. Spandidos, A., et al., *PrimerBank: a resource of human and mouse PCR primer pairs for gene expression detection and quantification.* Nucleic Acids Research, 2010. **38**(suppl_1): p. D792-D799.

Figure 4.1. Schematic of gene expression in the ventral region of the developing neural tube. Shh from the notochord initially triggers the expression of Olig2. In more dorsal regions, cell are desensitized to the effects of Shh, while more ventral cells are not, leading to Nkx2.2 expression. Once established, the domains both undergo a wave of neurogenesis. Later, Oig2 and Nkx2.2 become co-expressed at the boundary and are termed OPC.

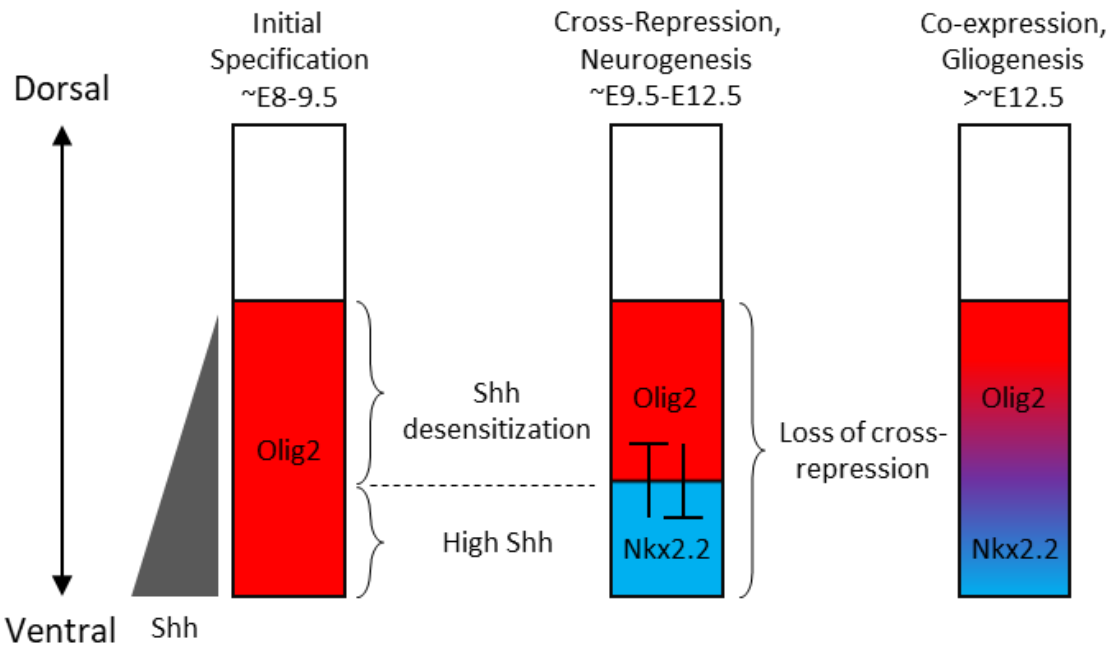
Dorsal
Ventral
Shh
Initial
Specification
~E8-9.5
Olig2
Shh
desensitization
High Shh
Cross-Repression,
Neurogenesis
~E9.5-E12.5
Olig2
Nkx2.2
Loss of cross-
repression
Co-expression,
Gliogenesis
>~E12.5
Olig2
Nkx2.2

Figure 4.2. Olig2 protein expression and transcription are nonlinearly regulated by DAPT. (A) Schematic of cell treatments. (B-C) Representative image of Olig2 (red) and GFP at the 24 hour time pointfor DMSO (B) and DAPT (C) treated cultures. (D-F) Cell fractions for GFP (D), Olig2 ICC (E) and ICC/GFP (F). n=3, Bars depict mean +/- s.e.m. Two-way ANOVA with Holm-Sidak method for multiple comparisons, *P<0.05 within time point, **P<0.001 within time point, #P<0.01 vs time 0, ##P<0.001 vs time 0. Scale bar: 100 μm.

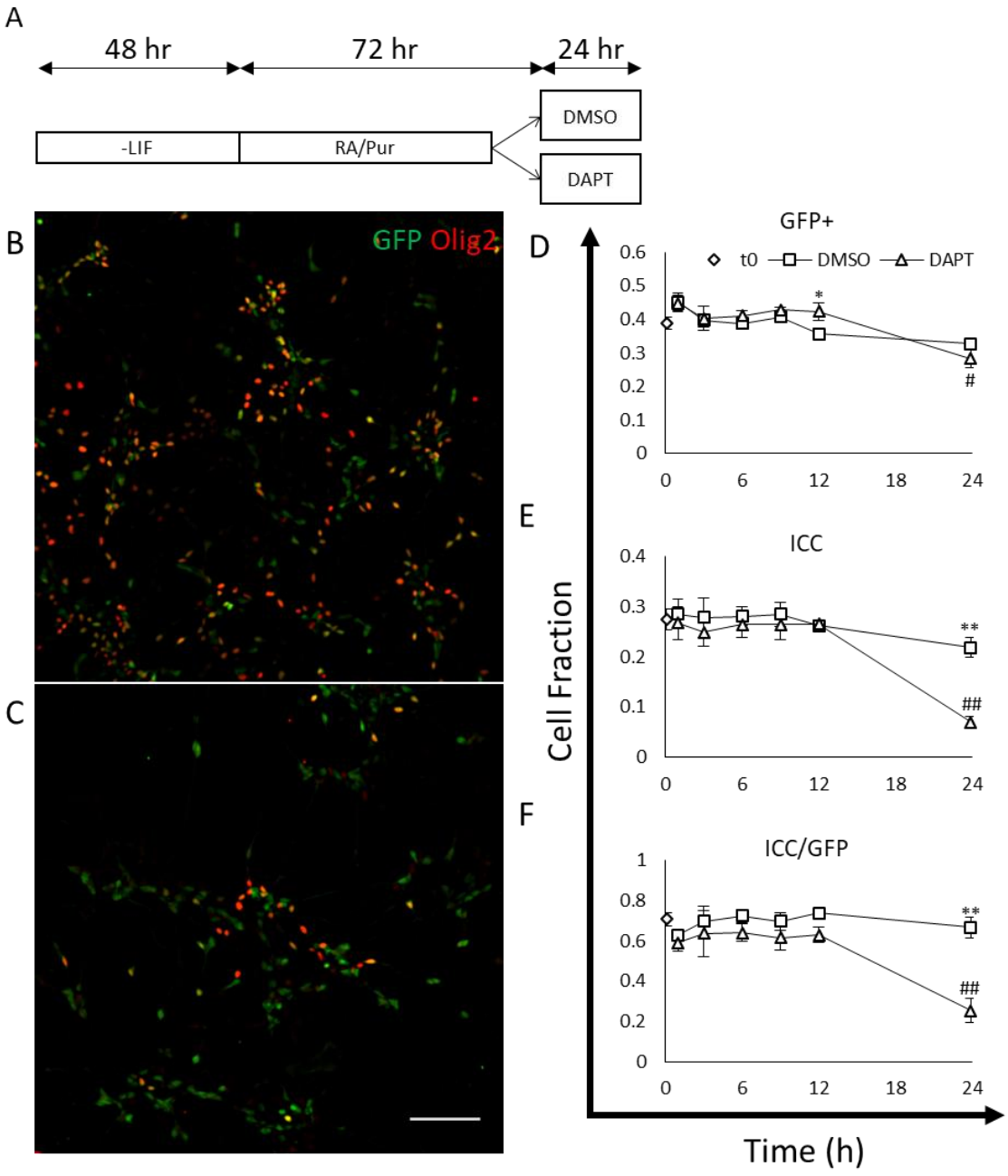
A
48 hr
72 hr
24 hr
-LIF
RA/Pur
DMSO
DAPT
B
GFP Olig2
C
D
GFP+
t0
DMSO
DAPT
E
ICC
F
ICC/GFP
Cell Fraction
Time (h)

Figure 4.3. Overview of Tgf-β, Shh and Notch signaling on Olig2, Nkx2.2 and GFP expression. (A) Treatment schematic. (B) Percent of total cells expressing each marker. (C) Percent of individual cell types identified. (D) Ratio of GFP^+:pMN. n=2 biological replicates. Bars represent mean + s.e.m. Please see Supplementary Table 1 for *P*- values and multiple comparisons from three-way ANOVA with Holm-Sidak method for multiple comparisons.

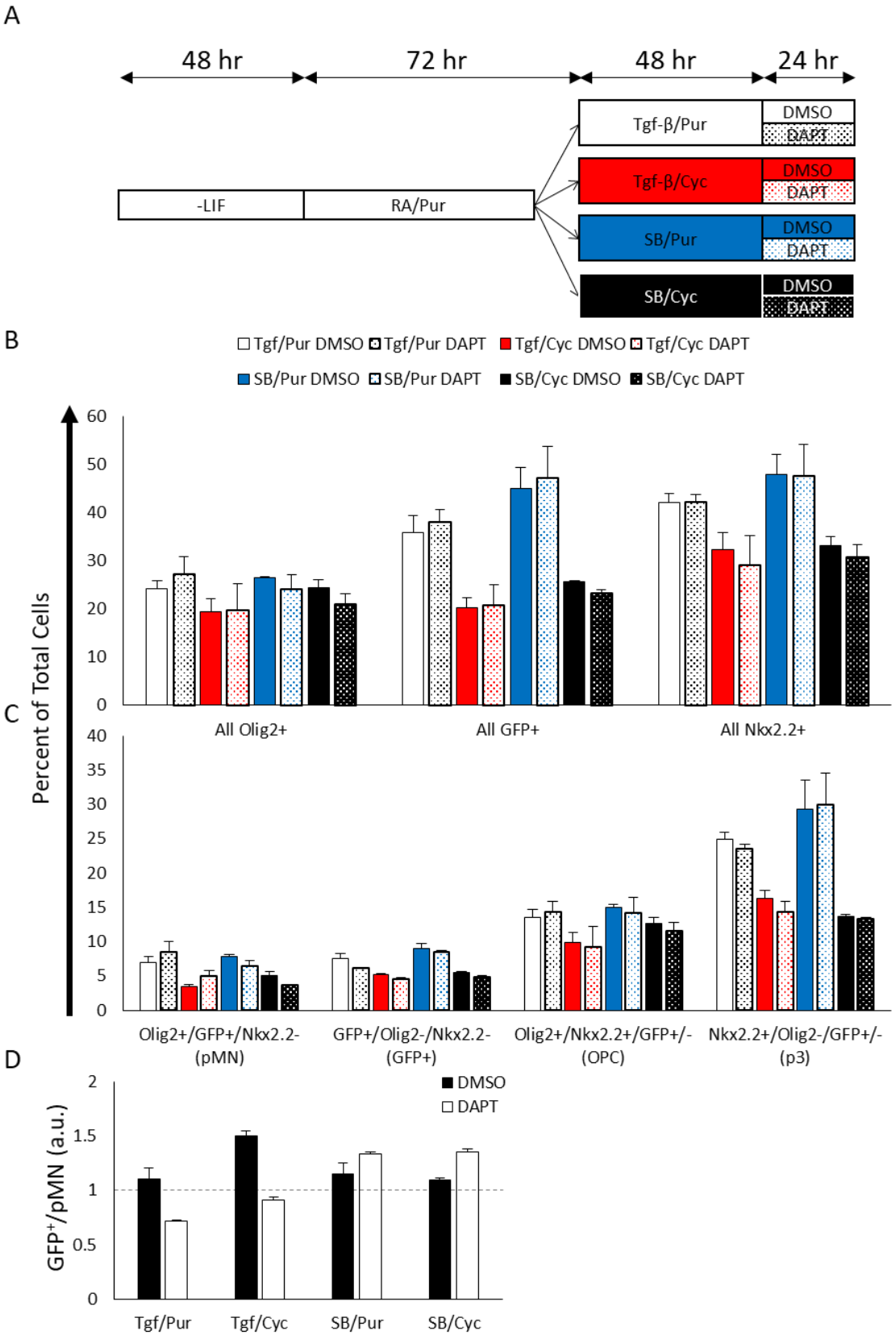
A
48 hr
72 hr
48 hr
24 hr
-LIF
RA/Pur
Tgf-β/Pur
Tgf-β/Cyc
SB/Pur
SB/Cyc
DMSO
DAPT
B
Tgf/Pur DMSO
Tgf/Pur DAPT
Tgf/Cyc DMSO
Tgf/Cyc DAPT
SB/Pur DMSO
SB/Pur DAPT
SB/Cyc DMSO
SB/Cyc DAPT
C
Percent of Total Cells
All Olig2+
All GFP+
All Nkx2.2+
Olig2+/GFP+/Nkx2.2-
(pMN)
GFP+/Olig2-/Nkx2.2-
(GFP+)
Olig2+/Nkx2.2+/GFP+/-
(OPC)
Nkx2.2+/Olig2-/GFP+/-
(p3)
D
GFP+/pMN (a.u.)
Tgf/Pur
Tgf/Cyc
SB/Pur
SB/Cyc

Figure 4.4. Insights into differentiation trajectories in Shh, Tgf-β, and/or DAPT. (A) Proposed differentiation trajectory. (B) Ratio of ancestor to descendant for pMN:GFP^{+}, p3:pMN, OPC:pMN, and OPC:p3. One-way ANOVE with Holmd-Sidak method for mlutple comparisons. n=2 biological replicates. Bars depict mean + s.e.m. *P<.05 from complete inhibition, **P<0.01 from complete inhibition, ***P<0.001 from complete inhibition, #P=0.067 from complete inhibition.

A

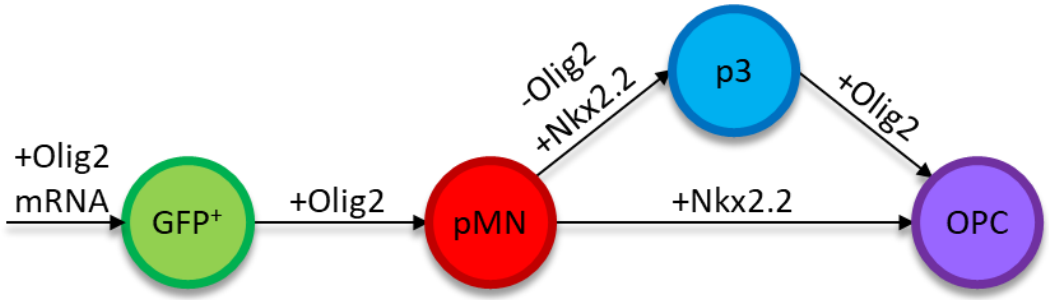
+Olig2
mRNA
GFP+
+Olig2
pMN
-Olig2
+Nkx2.2
p3
+Olig2
+Nkx2.2
OPC

B

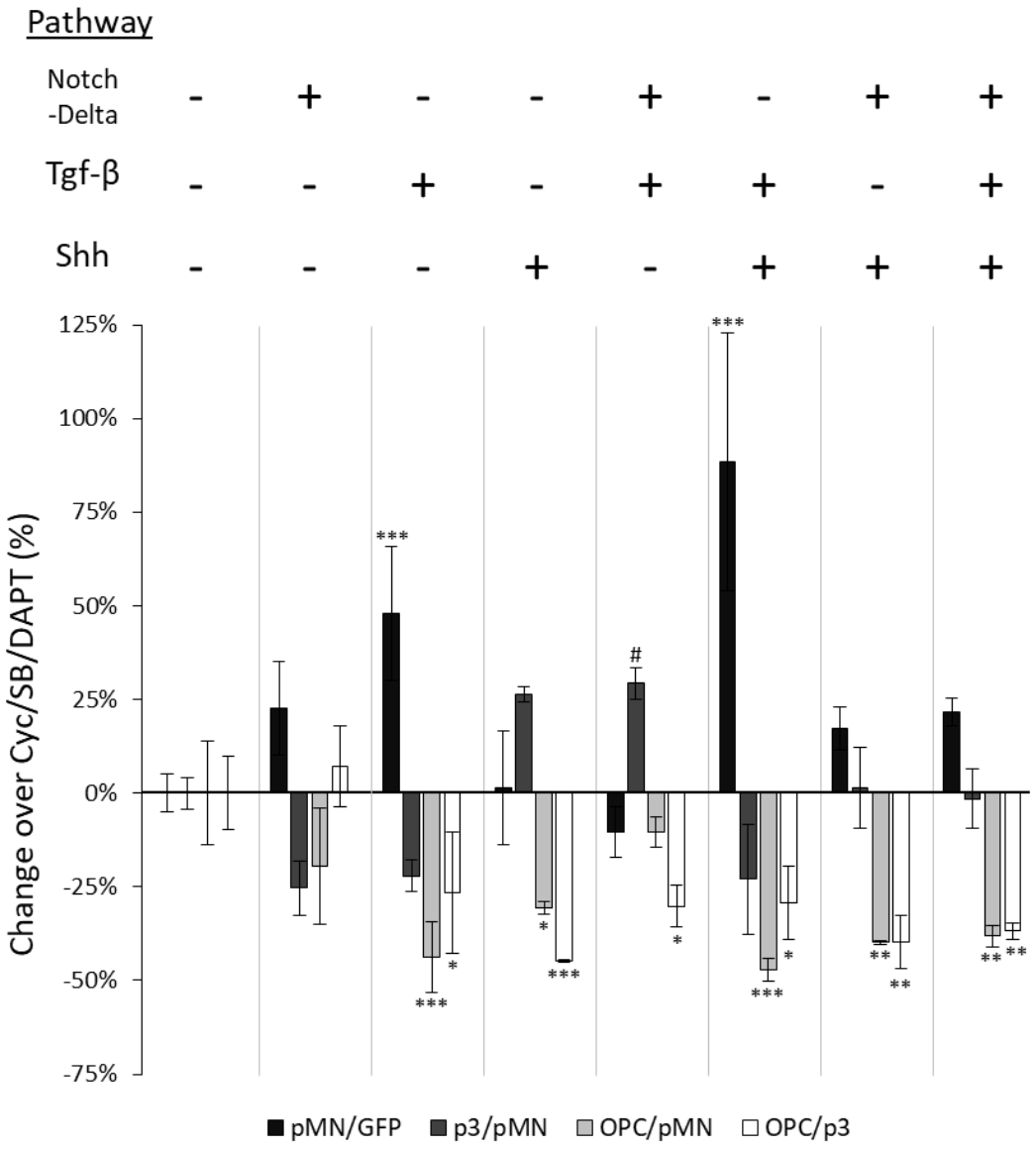
Pathway
Notch
-Delta
Tgf-β
Shh
Change over Cyc/SB/DAPT (%)
125%
100%
75%
50%
25%
0%
-25%
-50%
-75%
pMN/GFP
p3/pMN
OPC/pMN
OPC/p3

Figure 4.5. Effects of increasing Pur concentrations on cell type specification. (A) Treatment schematic. Fold change over 1 μM for (B-D) Overall marker expression and (E-H) individual cell types. Two way ANOVA with Holm-Sidak method for multiple comparisons. n=2 biological replicates. Bars depict mean +/- s.e.m. *P<0.05 vs 1 μM within Pur dose, ** P<0.01 vs 1 μM within Pur dose, *** P<0.001 vs 1 μM within Pur dose, # P<0.05 vs 1 μM within Pur dose/DAPT, ## P<0.01 vs 1 μM within Pur dose/DAPT, ### P<0.001 vs 1 μM within Pur dose/DAPT, † P<0.05 vs 1 μM within Pur dose/DMSO, †† P<0.01 vs 1 μM within Pur dose/DMSO , ††† P<0.001 vs 1 μM within Pur dose/DMSO, ‡ P<0.05 vs 1 μM between DMSO/DAPT within Pur dose.

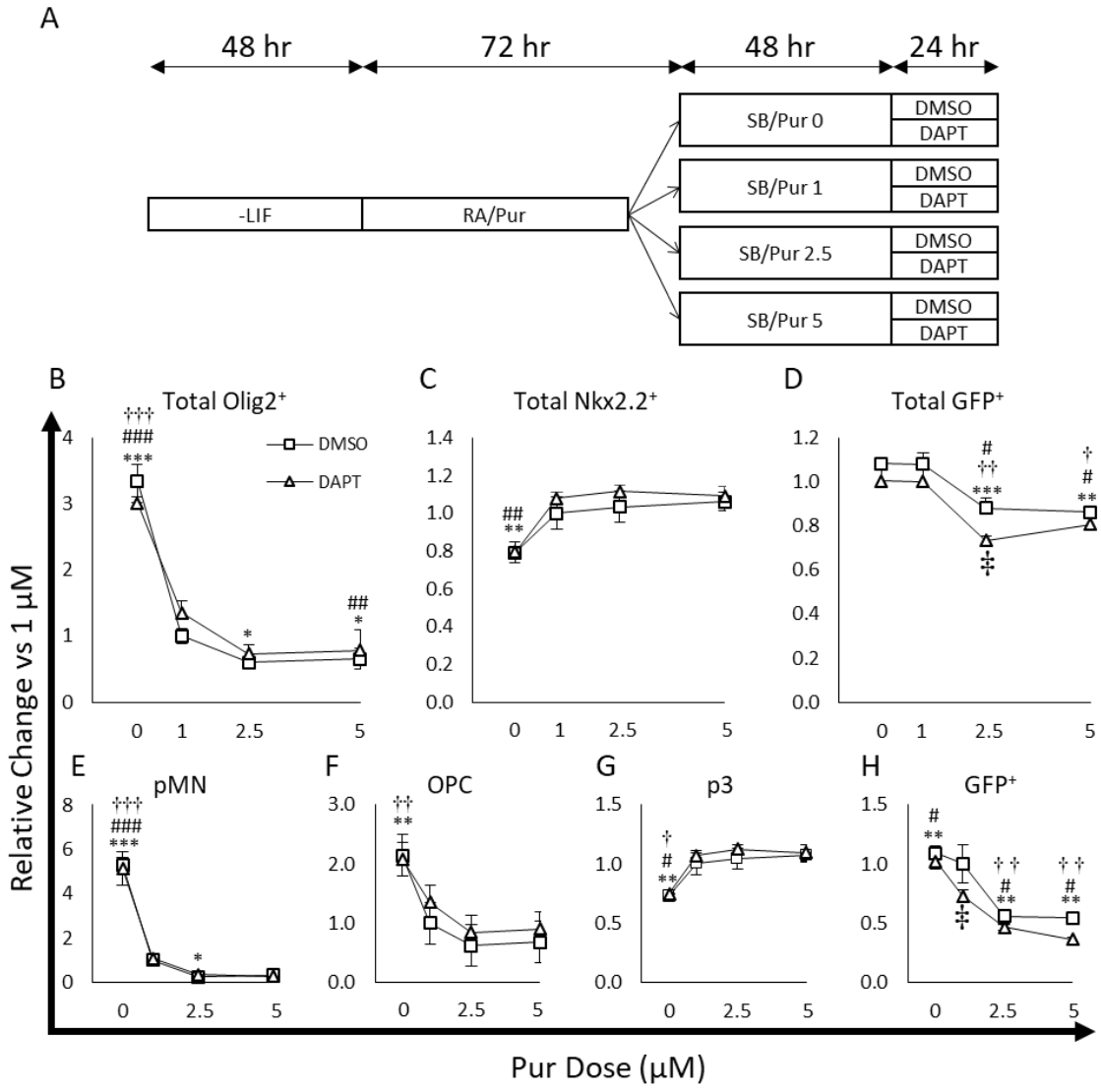
A
48 hr
72 hr
48 hr
24 hr
-LIF
RA/Pur
SB/Pur 0
SB/Pur 1
SB/Pur 2.5
SB/Pur 5
DMSO
DAPT
B
Total Olig2+
C
Total Nkx2.2+
D
Total GFP+
E
pMN
F
OPC
G
p3
H
GFP+
DMSO
DAPT
Relative Change vs 1 µM
Pur Dose (µM)

Figure 4.6. DAPT has inverse effects on Olig2 protein, but not mRNA, in Tgf-β inhibited or activate cultures. (A) Schematic for cell treatment. (B)Representative image of western blot and relative quantification to β-actin levels in Tgf-β- and SB431542-treated cultures. (C) mRNA levels relative to the average of Canx and Hprt and normalized to SB431542/DMSO. n=3 biological replicates. Bars reprent mean +/- s.e.m. Two way ANOVA with Holm-Sidak method for multiple comparisons. *P<0.05.

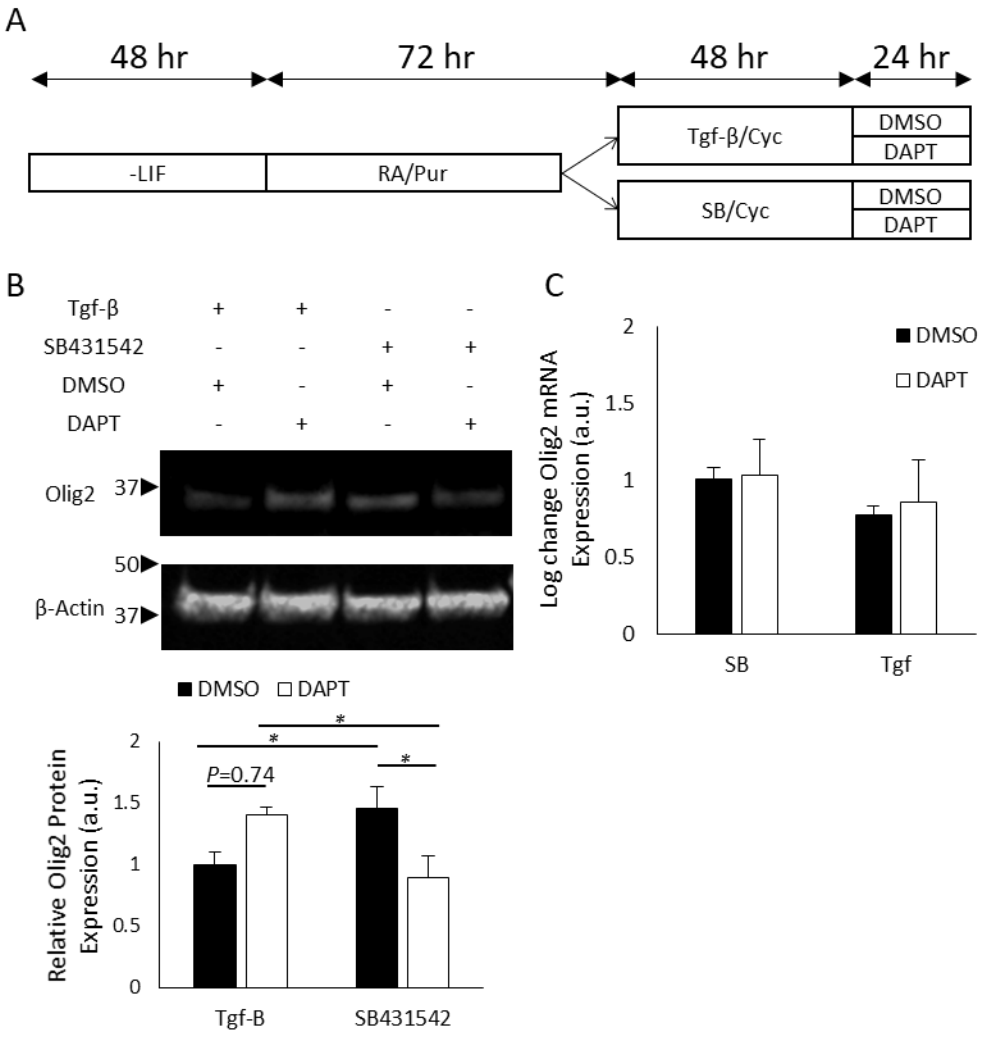
A
48 hr
72 hr
48 hr
24 hr
-LIF
RA/Pur
Tgf-β/Cyc
SB/Cyc
DMSO
DAPT
DMSO
DAPT
B
Tgf-β + + - -
SB431542 - - + +
DMSO + - + -
DAPT - + - +
Olig2
37
50
β-Actin
37
DMSO DAPT
Relative Olig2 Protein Expression (a.u.)
P=0.74
*
*
*
Tgf-B
SB431542
C
DMSO
DAPT
Log change Olig2 mRNA Expression (a.u.)
SB
Tgf

Supplementary Table 4.1. *P*-values for Figure 4.3.

Total Olig2+					
Source of Variation	DF	SS	MS	F	P
Tgf/SB	1	6.838	6.838	0.653	0.443
Pur/Cyc	1	173.449	173.449	16.555	0.004
DMSO/DAPT	1	0.403	0.403	0.0385	0.849
Tgf/SB x Pur/Cyc	1	6.2	6.2	0.592	0.464
Tgf/SB x DMSO/DAPT	1	15.484	15.484	1.478	0.259
Pur/Cyc x DMSO/DAPT	1	0.706	0.706	0.0673	0.802
Tgf/SB x Pur/Cyc x DMSO/DAPT	1	0.24	0.24	0.0229	0.883
Residual	8	83.817	10.477		
Total	15	287.137	19.142		
Total GFP+					
Source of Variation	DF	SS	MS	F	P
Tgf/SB	1	169.325	169.325	6.943	0.03
Pur/Cyc	1	1817.53	1817.53	74.526	<0.001
DMSO/DAPT	1	2.665	2.665	0.109	0.749
Tgf/SB x Pur/Cyc	1	40.101	40.101	1.644	0.236
Tgf/SB x DMSO/DAPT	1	0.473	0.473	0.0194	0.893
Pur/Cyc x DMSO/DAPT	1	4.01	4.01	0.164	0.696
Tgf/SB x Pur/Cyc x DMSO/DAPT	1	3.582	3.582	0.147	0.712
Residual	8	195.104	24.388		
Total	15	2232.789	148.853		
Total Nkx2.2+					
Source of Variation	DF	SS	MS	F	P
Tgf/SB	1	45.698	45.698	1.764	0.221
Pur/Cyc	1	1014.741	1014.741	39.174	<0.001
DMSO/DAPT	1	5.593	5.593	0.216	0.655
Tgf/SB x Pur/Cyc	1	30.305	30.305	1.17	0.311
Tgf/SB x DMSO/DAPT	1	0.837	0.837	0.0323	0.862
Pur/Cyc x DMSO/DAPT	1	2.624	2.624	0.101	0.758
Tgf/SB x Pur/Cyc x DMSO/DAPT	1	0.0961	0.0961	0.00371	0.953
Residual	8	207.225	25.903		
Total	15	1307.12	87.141		
GFP+/Olig2+/Nkx2.2- (pMN)					
Source of Variation	DF	SS	MS	F	P
Tgf/SB	1	0.294	0.294	0.248	0.632
Pur/Cyc	1	39.596	39.596	33.414	<0.001

DMSO/DAPT	1	0.0473	0.0473	0.0399	0.847
Tgf/SB x Pur/Cyc	1	0.494	0.494	0.416	0.537
Tgf/SB x DMSO/DAPT	1	8.985	8.985	7.582	0.025
Pur/Cyc x DMSO/DAPT	1	0.0000562	0.0000562	0.0000475	0.995
Tgf/SB x Pur/Cyc x DMSO/DAPT	1	0.0000563	0.0000563	0.0000475	0.995
Residual	8	9.48	1.185		
Total	15	58.896	3.926		
Comparisons for factor: Tgf/SB within DMSO					
Comparison	Diff of Means	t	P		
SB vs. Tgf	1.228	1.595	0.149		
Comparisons for factor: Tgf/SB within DAPT					
Comparison	Diff of Means	t	P		
Tgf vs. SB	1.77	2.299	0.051		
Olig2+/ Nkx2.2+/ GFP+/- (OPC)					
Source of Variation	DF	SS	MS	F	P
Tgf/SB	1	128.652	128.652	8.789	0.018
Pur/Cyc	1	947.562	947.562	64.732	<0.001
DMSO/DAPT	1	8.925	8.925	0.61	0.457
Tgf/SB x Pur/Cyc	1	30.003	30.003	2.05	0.19
Tgf/SB x DMSO/DAPT	1	3.285	3.285	0.224	0.648
Pur/Cyc x DMSO/DAPT	1	5.676	5.676	0.388	0.551
Tgf/SB x Pur/Cyc x DMSO/DAPT	1	1.843	1.843	0.126	0.732
Residual	8	117.106	14.638		
Total	15	1243.053	82.87		
Olig2-/Nkx+/gfp+/- (p3)					
Source of Variation	DF	SS	MS	F	P
Tgf/SB	1	12.978	12.978	1.175	0.31
Pur/Cyc	1	623.626	623.626	56.454	<0.001
DMSO/DAPT	1	2.288	2.288	0.207	0.661
Tgf/SB x Pur/Cyc	1	53.181	53.181	4.814	0.06
Tgf/SB x DMSO/DAPT	1	3.45	3.45	0.312	0.592
Pur/Cyc x DMSO/DAPT	1	0.62	0.62	0.0561	0.819
Tgf/SB x Pur/Cyc x DMSO/DAPT	1	0.0281	0.0281	0.00254	0.961
Residual	8	88.374	11.047		
Total	15	784.544	52.303		

GFP Only					
Source of Variation	DF	SS	MS	F	P
Tgf/SB	1	4.873	4.873	15.156	0.005
Pur/Cyc	1	30.997	30.997	96.408	<0.001
DMSO/DAPT	1	2.489	2.489	7.74	0.024
Tgf/SB x Pur/Cyc	1	2.426	2.426	7.545	0.025
Tgf/SB x DMSO/DAPT	1	0.253	0.253	0.785	0.401
Pur/Cyc x DMSO/DAPT	1	0.143	0.143	0.443	0.524
Tgf/SB x Pur/Cyc x DMSO/DAPT	1	0.284	0.284	0.882	0.375
Residual	8	2.572	0.322		
Total	15	44.035	2.936		
Comparison	Diff of Means	t	P		
SB vs. Tgf	1.883	4.695	0.002		
Comparisons for factor: Tgf/SB within Cyc					
Comparison	Diff of Means	t	P		
SB vs. Tgf	0.325	0.811	0.441		
GFP+:pMN					
Source of Variation	DF	SS	MS	F	P
Tgf/SB	1	0.123	0.123	18.281	0.003
Pur/Cyc	1	0.0786	0.0786	11.687	0.009
DMSO/DAPT	1	0.0749	0.0749	11.14	0.01
Tgf/SB x Pur/Cyc	1	0.0981	0.0981	14.581	0.005
Tgf/SB x DMSO/DAPT	1	0.499	0.499	74.244	<0.001
Pur/Cyc x DMSO/DAPT	1	0.0046	0.0046	0.685	0.432
Tgf/SB x Pur/Cyc x DMSO/DAPT	1	0.0205	0.0205	3.055	0.119
Residual	8	0.0538	0.00673		
Total	15	0.953	0.0635		
Comparisons for factor: Pur/Cyc within Tgf					
Comparison	Diff of Means	t	P		
Cyc vs. Pur	0.297	5.117	<0.001		
Comparisons for factor: Tgf/SB within Pur					
Comparison	Diff of Means	t	P		

SB vs. Tgf	0.332	5.723	<0.001		
Comparisons for factor: DMSO/DAPT within Tgf					
Comparison	Diff of Means	t	P		
DMSO vs. DAPT	0.49	8.453	<0.001		
Comparisons for factor: DMSO/DAPT within SB					
Comparison	Diff of Means	t	P		
DAPT vs. DMSO	0.216	3.733	0.006		
Comparisons for factor: Tgf/SB within DMSO					
Comparison	Diff of Means	t	P		
Tgf vs. SB	0.178	3.069	0.015		
Comparisons for factor: Tgf/SB within DAPT					
Comparison	Diff of Means	t	P		
SB vs. Tgf	0.529	9.116	<0.001		

CHAPTER 5

CONCLUSIONS

Much of the current dogma in pluripotent stem cell (PSC) differentiation comes from our underlying knowledge of development. *In vivo* models work extremely well because they are extremely predictable. The precisely timed patterning events of cell type specification, self-renewal and terminal differentiation rarely change unless we impose change upon them. Our results, however, reinforce that PSC differentiation disrupts cellular processes in ways that would never come to light in a living system, but must be accounted for in order for *in vitro* models to be useful. To our knowledge, no study, *in vivo* or *in vitro*, has demonstrated the expression of the motor neuron (MN) marker Hb9 prior to the expression of the motor neuron progenitor (pMN) marker Olig2. In the first experiment we performed, our view of the pMN differentiation paradigm was shifted. Further, we cannot overstate the usefulness of computational modeling here. These events would likely have been ignored had we not been forced to fit them into a mathematical system that demanded objectivity. Using computational modeling to aid in biological hypotheses led us to consider a transient or destabilized progenitor state. Further iterations on our model led to the theory that Notch signaling provides some necessary signal to stabilize progenitors, and specifically Olig2 expression. Late Notch inhibition led us to hypothesize that this Notch-based stabilization signal was replaced by another signal, rendering Notch inhibition incapable of generating MN or losing Olig2 expression. Experimental data implied that a negative feedback signal from both MN and

at least one other mature cell type is capable of causing a switch in progenitor cells from neurogenesis to gliogenesis. Ultimately, we realized that the Notch-replacement signal and the soluble negative feedback signal could be one and the same, in the form of transforming growth factor-β (Tgf-β).

To better understand the convergence of extracellular signals capable of regulating pMN cells, we next explored the intersection of Notch, Shh and Tgf-β. We found that Tgf-β decreased Olig2 transcription. Increased Shh activation led to increased Nkx2.2-expressing p3 cells. Notably, decreased Shh activation, while not changing the number of cells transcribing Olig2, vastly increased the number of cells expressing the Olig2 protein, implicating post-transcriptional, Shh-based suppression of Olig2 as a key determinant of *in vitro* differentiation. Increasing Shh, however, could not counteract the effects of DAPT in the absence of Tgf-β signaling. The combination of Tgf-β and DAPT, surprisingly, stabilized Olig2-expressing progenitors both in the acquisition of Olig2 protein expression, as well as by restricting their progression towards either p3 or OPC.

Taken together, we can draw a number of conclusions, often opposing, about the specification of and differentiation from Olig2-expressing cells: (1) Endogenous Notch signaling provides a weak stabilizing signal for Olig2, suitable for neurogenesis and asymmetric divisions; (2) Notch inhibition destabilizes the Olig2 protein, but also suppresses p3; (3) Tgf-β decreases Olig2 transcription, but also provides strong Olig2 stability, which blocks neurogenesis and is more suitable for persistent Olig2 expression in OPC (4) Shh pathway activation drives Olig2 transcription, but also Nkx2.2, which suppresses Olig2. This complex list of mechanisms displays the intricate balance that

must be met *in vivo*, but also in *in vitro* studies, for successful cellular homo- or heterogeneity, depending on the desired outcome. From our experiments, we can build a hierarchical structure to these conclusions: (1) The Tgf-β/DAPT combination stabilizes Olig2 more than Nkx2.2 or DAPT alone can repress it; (2) Shh alone is unable to drive Olig2 or Nkx2.2 in the absence of Notch, resulting in neurogenesis; (3) Tgf-β is insufficient to overcome Shh-driven p3 generation in the presence of Notch signaling. In summing these inferences and assigning a tiered structure to them, we can better deduce how differentiation occurs.

We propose that, under low levels of Notch signaling and destabilized Olig2, MN generation occurs instead of the generation of Olig2-expressing progenitors. With complete Notch inhibition, the Olig2 protein is never stabilized resulting in increased MN and a total depletion of pMN progenitors and their downstream progeny, p3 and OPC. Later, MN production plateaus as MN and pMN both secrete Tgf-β. Tgf-β weakens overall Olig2 transcription, resulting in few newborn pMN, but effectively blocks the generation of MN. This weakening of Olig2 transcription in the presence of Notch signaling leads to an uptick in p3 cells from pMN, as Nkx2.2 represses the Olig2 protein. However, in the absence of Notch, Tgf-β effectively blocks neurogenesis while Notch inhibition suppresses p3 generation, yielding an expanded pMN population. For pMN or p3 to become OPC, each requires a distinct and permissive cell state. Based on our results, we hypothesize that pMN cell transition to OPC (i.e. adding Nkx2.2 expression to cells already expressing Olig2) requires weak Olig2 stabilization in the absence of Shh. "Weak Olig2 stabilization" falls under one of two scenarios. First, Tgf-β, which blocks neurogenesis but also inhibits Olig2 transcription, combined with Notch signaling which

weakly stabilizes the protein, can lead to increases in Nkx2.2 expression in the presence of Olig2 and, thus, OPC. The second weakened state includes Tgf-β inhibition in the absence of Notch, which would lead to an unstable Olig2 protein, but with restored Olig2 transcription. Generating OPC from p3 would require decreased Shh signaling, a weakly stabilized Olig2 protein by Notch signaling, but also strengthened Olig2 transcription through Tgf-β blockade.

Future Studies

Though our studies produced novel and interesting results and hypotheses, they leave many questions unanswered and even ask new questions not previously considered. Foremost among these is the idea of a transient progenitor. We hypothesized that Olig2 protein expression is not necessary for MN generation. We believe that Olig2 transcription is sufficient to show that, in an *in vitro* milieu highly disrupted from *in vivo* conditions, the genetic machinery is available to generate MN. One possible experiment to demonstrate the existence of this cell type is with a dual lox-stop-lox-tag reporter system. One reporter would act a lineage tracer for Olig2 transcription, similar to the G-Olig2 cell line, multiplexed with an Olig2 response element driving a second reporter to detect protein expression. MN could be quantified based on Hb9 expression and the status of each reporter for Olig2 transcription and the Olig2 protein. Moreover, we have assumed that Olig2 protein expression is necessary for Nkx2.2 expression. Based on our MN and transient progenitor results, this may not be the case. A multiplexed reporter system could answer this question, as well.

We also hypothesized that MN and pMN both secrete Tgf-β to trigger the glial switch. A simple experiment could be done confirm this, but genetic schemes may do a

better job of making the point. Here, we studied the Tgf-β phenomenon using small molecules and recombined protein. Given that we know response elements for both Olig2 and Hb9, along with the ease of use of Crispr-based genetic manipulation, cell type specific knockout or knockdown of various Tgf-β family members, and a corresponding loss of OPC, would make a convincing argument as for the source of this glial switch. It may also shed light on compensation within the Tgf-β family and within the cell population as a whole.

Our studies yielded overviews of differentiation largely employing cell type quantification as endpoints. We expanded on this with hypothetical mechanistic interpretations. However, more work needs to be done to test the proposed underlying mechanisms. We hypothesized that many of the proposed signals, including Notch and Tgf-β, act in a post-transcriptional mechanism to stabilize Olig2. It would be supportive to perform both actinomycin D and cyclohexamide experiments to determine at which stage Olig2 is affected: mRNA or protein, respectively. Further, we assume that many of the effects seen *in vivo* (i.e. DAPT suppression of Nkx2.2) will be true *in vitro.* Experiments could be designed based on the original study [1] to support our mechanistic hypotheses.

Perhaps the most daunting, but telling, set of experiments would be to identify the intracellular targets of both Notch and Tgf-β responsible for stabilizing Olig2. Given the resulting phenotypes we saw, it would be useful to perform RNA-seq to determine what factors are upregulated in response to each signal. The Hes/Hey family of genes are a likely target, as they are E-box binding bHLH transcription factors, like Olig2, and can likely bind many of the same targets. Moreover, they are direct targets of Notch but can

be modulated by other signaling pathways [2-4]. However, a blind approach may not yield positive results. Therefore, a more thorough approach would better identify the genetic targets within our cell of interest.

We also hypothesized that most of the effects of Notch, Tgf-β and Shh happen in parallel, but it is highly possible that there is significant crosstalk, again making Hes/Hey an enticing target given the overlap in regulation seen in other cell types. The post-translational state of Olig2, particularly with regards to phosphorylation of two specific groups of serines, has been widely implicated in the fate switch [5-8]. Thus, it is possible that, rather than some unique target, these signals converge on Olig2 itself. Lastly, we used endogenous Notch, rather than Notch overexpression. There is no guarantee that cultures have uniform Notch activation, and that NICD overexpression might not overcome some effects of Olig2 destabilization, particularly if Shh or Tgf-β converge on the Notch protein.

Perhaps the most exciting opportunity comes from the flow data combining all three signals in Chapter 4. We have made a set of hierarchical hypotheses about how differentiation works. Each of the factors examined was hypothesized to affect affecting multiple processes. Based on Chapter 3, we believe the best way to test hypotheses on factors with multiple modes of action and a large number of outcomes is through a computational model. Moreover, for our analysis, cell types were lumped together according to traditional protein markers, regardless of GFP expression. However, flow cytometry analysis indicates 10 unique populations, including GFP^-, GFP^{low}, and GFP^{high} cell states existing within traditional cell state. Including GFP^+ ($GFP^+/Olig2^-/Nkx2.2^-$) and pMN ($GFP^+/Olig2^+/Nkx2.2^-$), which were already mentioned, we found differing

GFP levels within p3 and OPC. Interestingly, pMN only expressed GFP^{high}, while p3 cells only expressed GFP^{low} and OPC could be high, low or negative. Cell only expressing GFP were all GFP^{low}. A computational model could be based on the addition or loss of each external factor, with different hypotheses based on which factors affect transcription directly and which effects occur post-transcriptionally. We could model probabilities for basic questions like, "Does Olig2 mRNA become downregulated or decreased before the protein, or is it the other way around?" For instance, is $Nkx2.2^{+}/Olig2^{-}/GFP^{low}$ a cell on its way to becoming an OPC, or is it a newborn p3 which has just downregulated the Olig2 protein but not them RNA yet. Or is the $Olig2^{+}/Nkx2.2^{+}/GFP^{-}$ the newborn p3, waiting for Olig2 to burn itself out? Or is it neither, or even both? A cell expressing only GFP and Olig2, for example, could potentially lose Olig2 protein (as seen with Notch inhibition), or could gain Nkx2.2 protein. But at what cost or manner does this happen, and in which extracellular circumstance is this most likely?

A model would not only be helpful, but likely necessary. We can make biologically sound arguments based on developmental biology and our work here that the $GFP^{high}/Olig2^{+}/Nkx2.2^{-}$ cell type alone could yield 6 different direct progeny (not including MN). Even a reduced model only encompassing cell types identified here, binary GFP, and with tight restrictions on differentiation trajectories, yields 144 distinct biological pathways, and this even excludes unidentified cell types and processes (i.e. astrocytes and neurons, both of which can derive from p3 and pMN, apoptosis). Ultimately, and as above, the model could point us towards possible theories, and would be followed up with wet lab work to confirm or deny them.

References

1. Kong, Jennifer H., et al., *Notch Activity Modulates the Responsiveness of Neural Progenitors to Sonic Hedgehog Signaling.* Developmental Cell, 2015. **33**(4): p. 373-387.
2. Fischer, A. and M. Gessler, *Delta–Notch—and then? Protein interactions and proposed modes of repression by Hes and Hey bHLH factors.* Nucleic Acids Research, 2007. **35**(14): p. 4583-4596.
3. Kageyama, R., T. Ohtsuka, and T. Kobayashi, *The Hes gene family: repressors and oscillators that orchestrate embryogenesis.* Development, 2007. **134**(7): p. 1243-51.
4. Borggrefe, T., et al., *The Notch intracellular domain integrates signals from Wnt, Hedgehog, TGFβ/BMP and hypoxia pathways.* Biochimica et Biophysica Acta (BBA) - Molecular Cell Research, 2016. **1863**(2): p. 303-313.
5. Meijer, D.H., et al., *An amino terminal phosphorylation motif regulates intranuclear compartmentalization of Olig2 in neural progenitor cells.* J Neurosci, 2014. **34**(25): p. 8507-18.
6. Li, H., et al., *Phosphorylation regulates OLIG2 cofactor choice and the motor neuron-oligodendrocyte fate switch.* Neuron, 2011. **69**(5): p. 918-29.
7. Sun, Y., et al., *Phosphorylation state of Olig2 regulates proliferation of neural progenitors.* Neuron, 2011. **69**(5): p. 906-17.
8. Gaber, Z.B. and B.G. Novitch, *All the embryo's a stage, and Olig2 in its time plays many parts.* Neuron, 2011. **69**(5): p. 833-5.